

Kinetics of Ferroics at Nanoscales (Towards Low-energy Consuming Devices)

Dissertation

zur Erlangung des Doktorgrades der Naturwissenschaften
(Dr. rer. nat.)

der

Naturwissenschaftlichen Fakultät II
Chemie, Physik und Mathematik

der Martin-Luther-Universität
Halle-Wittenberg

vorgelegt von

Herrn Seyyed Ruhollah Etesami
geb. am 06.08.1983 in Khomini Shahr (Isfahan, Iran)

verteidigt am 25.11.2016

Gutachter:

1. Prof. Dr. Jamal Berakdar, Martin-Luther-Universität Halle-Wittenberg
2. Prof. Dr. Steffen Trimper, Martin-Luther-Universität Halle-Wittenberg
3. Prof. Dr. Ireneusz Weymann, Adam Mickiewicz University, Poland

Contents

Abbreviations and Notations	viii
1 General Introduction	2
1.1 Motivation and Goal	2
1.2 Materials of Interest	3
1.3 Scales and Methods	3
1.4 Phenomena of Interest	3
2 Thermal Fluctuations in Magnetic Systems	4
2.1 A Theoretical Perspective to Thermal Fluctuations in Magnetic Systems	5
2.1.1 Stochastic Differential Equations and Fokker-Planck Equation	7
2.2 Landau-Lifshitz-Gilbert Equation	11
2.3 A Numerical Perspective to Thermal Fluctuations in Magnetic Systems	12
2.3.1 First Example : Thermal Average of Magnetization at Equilibrium	13
2.3.2 Second Example : Thermally Activated Magnetization Switching	14
2.3.3 Some Details about Numerical Procedure	14
3 Spin Seebeck Effect	17
3.1 Spin-Wave Spin Current inside a Ferromagnetic Sample	17
3.1.1 Longitudinal Spin Current in a Chain	20
3.2 Spin Current at the Interface	25
3.2.1 Longitudinal Spin Current near the Interface	25
3.2.2 Transversal Spin Current	27
3.3 Yttrium Iron Garnet	28
3.4 Spectral Characteristics of Spin-Wave Spin Current	29
3.4.1 Time-Resolved Study	30
3.5 White Noise vs Colored Noise	33
3.6 Domain-Wall Motion	34
4 Temperature in Ferroelectrics	36
4.1 Temperature in Ferroelectrics as Noise	36
4.1.1 Thermally Activated Switching Time	37
4.2 Ferroelectric Phase Diagrams : Barium Titanate	39
4.3 Pyroelectric Effect : Barium Titanate	43
4.3.1 Model	45
4.4 An Alternative : Deterministic Heat Baths	47
5 Multiferroics and Thermal Effects	49
5.1 Single-Phase Multiferroics : Bismuth Ferrite	49

5.2	Composite Multiferroics	52
5.2.1	Multiferroic Diode	53
5.2.2	Magnetically-Controlled Pyroelectric Engine	55
6	Summary, Conclusions, and Outlooks	60
6.1	Summary and Conclusions	60
6.2	Outlooks	62
6.2.1	Pyromagnetic Engine	62
6.2.2	Spin Seebeck Diode and Ratchet Spin Current via Dzyaloshinskii-Moriya Interaction	62
	Bibliography	64
	Eidesstattliche Erklärung	74
	Acknowledgements	75
	Curriculum Vitae	76
	List of Publications	77

List of Figures

1.1	Number of publications containing <i>ferromagnet</i> and <i>ferroelectric</i> since 1900	2
2.1	A typical ferromagnet-paramagnet phase transition diagram	4
2.2	The representation of a magnetic moment in spherical coordinates	5
2.3	Magnetic moment dynamics in the presence of an external magnetic field and dissipative sources	6
2.4	Trajectory of averaged reduced magnetization for a single ferromagnetic domain and equilibrium magnetization versus temperature	13
2.5	Trajectory of the z component of reduced magnetization of a single ferromagnetic domain and mean-first-passage time versus temperature	15
2.6	Generate a standard normal distribution out of a uniform distribution	16
3.1	Schematic of the meaning of different components of the spin-wave spin current tensor	19
3.2	Schematic of spin Seebeck effect and the role of exchange torque in the generation or absorption of spin current	21
3.3	The spin currents and the exchange torque profiles in a ferromagnetic chain	22
3.4	The spin current profile for different temperature gradients in a ferromagnetic chain	23
3.5	The magnon accumulation profile in a ferromagnetic chain	23
3.6	The spin current profile for ferromagnetic chains with different lengths	24
3.7	Schematic of detection of longitudinal and transversal spin Seebeck effect	25
3.8	Effects of enhanced Gilbert damping and Spin-transfer torque on the longitudinal spin current	26
3.9	Net transversal spin current injected to the normal metal	27
3.10	Phonon and magnon temperature profiles for a ferromagnetic chain under a temperature gradient	28
3.11	Spin-wave dispersion for Yttrium Iron Garnet	30
3.12	The time-resolved study of spin Seebeck effect	31
3.13	Spin-wave spin current versus the modulation frequency for different extrinsic cutoff frequencies	32
3.14	Spin-wave spin current with white noise and colored noise for different values of correlation time	33
3.15	Domain wall motion due to spin Seebeck effect	34
3.16	Domain wall motion for different temperature gradients and frequencies of pulsed heating	35
4.1	Thermally-activated switching of polarization	37
4.2	Polarization switching time as a function of electric field for different temperatures and as a function of inverse temperature for different electric fields	38

4.3	The frequency of optical phonons versus electric field and inverse internal resistivity	39
4.4	Polarization vector at different phases of Barium Titanate	40
4.5	The procedure to obtain the phase diagram including the structural phase transitions	41
4.6	The Barium Titanate polarization and its phase diagram for different electric fields	42
4.7	The Barium Titanate polarization and its phase diagram for different pressures	42
4.8	The Barium Titanate polarization and its phase diagram for different cell sizes	43
4.9	Schematic of exploitation of temperature-dependency of hysteresis loops for pyroelectric effect	44
4.10	Performance of an Olsen cycle in pyroelectric effect	45
4.11	The produced electrical energy and pyroelectric efficiency versus hydrostatic pressure	46
4.12	Conductivity of a ferroelectric chain under Nose-Hoover thermostats . . .	47
5.1	Schematic of a G-type antiferromagnet and the simulated system for Bismuth Ferrite	50
5.2	x,y and z components of the magnetic moments and magnetically-induced polarizations in Bismuth Ferrite	51
5.3	A three-dimensional picture of magnetic moments in Bismuth Ferrite . .	52
5.4	Schematic presentation of the multiferroic diode	53
5.5	Heat current flowing inside a multiferroic diode for different biased temperatures	54
5.6	Magnetically-controlled pyroelectric engine	56
5.7	The produced electrical energy and the corresponding efficiency versus the amplitude of the oscillatory magnetic field	57
5.8	The produced electrical energy and the corresponding efficiency versus magnetoelectric coupling	58
5.9	The produced electrical energy and the corresponding efficiency versus magnetoelectric coupling for different values of magnetic field	58
6.1	Schematic of the proposed pyromagnetic engine	62
6.2	Spin-wave dispersion for different values of Dzyaloshinskii-Moriya interaction	63

List of Tables

3.1	Phonon-magnon relaxation times and the corresponding frequencies for Yttrium Iron Garnet	30
4.1	Barium Titanate parameters	41
5.1	Bismuth Ferrite parameters	50

Abbreviations and Notations

FM	Ferromagnet
FE	Ferroelectric
APS	American Physical Society
MF	Multiferroic
SDE	Stochastic Differential Equations
LLG	Landau-Lifshitz-Gilbert (equation)
FPE	Fokker-Planck Equation
MFPT	Mean-First-Passage time
SSE	Spin Seebeck effect
SW	Spin wave
NM	Normal metal
ISHE	Inverse spin-Hall effect
YIG	Yttrium iron garnet
LLMS	Landau-Lifshitz-Miyasaki-Seki (approach)
DW	Domain wall
TDGL	Time-dependent Ginzburg-Landau (equation)
GLD	Ginzburg-Landau-Devonshire (potential)
BTO	Barium Titanate (BaTiO_3)
ME	Magnetoelectric
BFO	Bismuth Ferrite (BiFeO_3)
AFM	Antiferromagnet
DM	Dzyaloshinskii-Moriya

ι	Angular momentum
μ	Magnetic moment
H	Magnetic field
γ	Gyromagnetic ratio
θ	Polar angle of the magnetic moment in spherical coordinates
φ	Azimuthal angle of magnetic moment in spherical coordinates
α	damping parameter
k_B	Boltzmann constant
T	Temperature
M	Magnetization
M_S	Saturation magnetization
a	Cell size
F	Free energy density
Ω	Probability
A	Exchange stiffness constant
k	Uniaxial anisotropy constant
S	Spin density
$\varepsilon_{j\nu\beta}$	Levi-Civita antisymmetric tensor
q	Wave vector
\hbar	Planck constant
P	Polarization
E	Electric field
γ_v	Internal resistivity
Q_{ij}	Electrostrictive coefficients
ε^m	Magnetic energy
ε	Electric energy
ε_0	Vacuum permittivity
ε_r	Relative permittivity
ϱ	Resistivity
Q	Thermal energy (heat)
ρ	Mass density
c	Specific heat
μ_0	Vacuum permeability
μ_B	Bohr magneton

1 General Introduction

1.1 Motivation and Goal

Waste heat has always been a severe bottleneck. It reduces the efficiency of machines and much worse, extra energy is needed to cool down the systems. Looking globally, to have the global warming under control while maintaining sustainable energy services, it is worth to think about waste heat. From a completely different perspective, at nanoscales, heat also becomes more and more troublesome nowadays as the devices become smaller and smaller so that it even sometimes diminishes the functionality of devices. In this regard finding ways to reuse heat as a mechanical or electrical energy is overwhelmingly important. Our motivation in this thesis is to take one small step in this direction. Naturally, first we need to know how the heat affects the systems. Therefore, our main goal in this thesis is a fundamental investigation of thermal effects, though it might not be directly related to the technical realization of thermal energy harvesting at this stage. By *kinetic* in the title of the thesis, we mean these thermal effects.

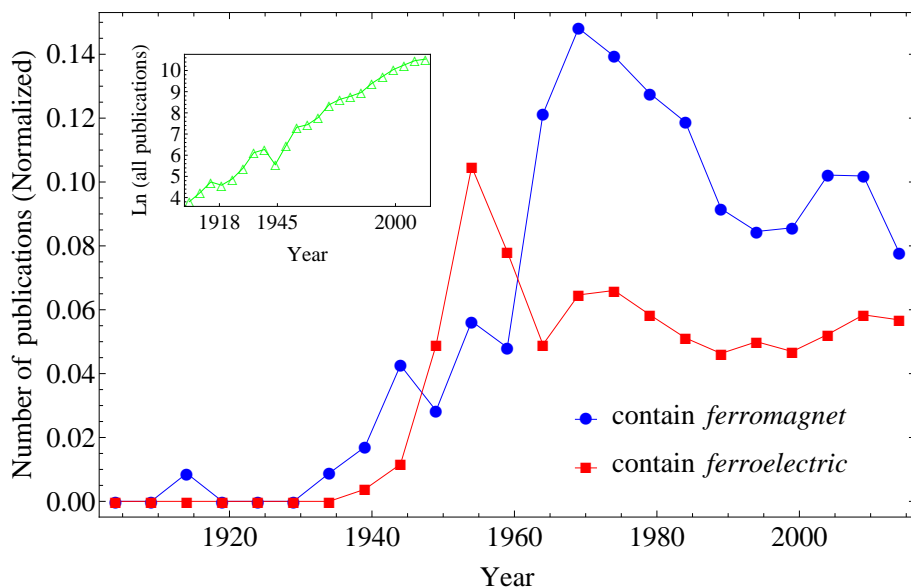


Figure 1.1: Number of APS publications per five years containing a specific word, normalized by the total number of publications per five years since 1900. The inset shows the logarithm of the total number of APS publications per five years (strictly speaking, the total number of APS publications per five years which contain the letter *a*).

1.2 Materials of Interest

Our materials of interest are ferromagnets (FMs) and ferroelectrics (FEs). These materials have revolutionized our life and can be found in almost every electronic device that we touch every day, from our refrigerator to our mobile phone. The number of papers published on the American Physical Society¹ (APS) which contain such terms shows that still such materials are of great interest to the physics community (Fig. 1.1).

Both FMs and FEs have long range ordering which is characterized by magnetization in FMs and polarization in FEs. External magnetic and electric fields directly affect the magnetization and the polarization, respectively. The emergence of a new type of materials known as multiferroics (MFs) has provided the opportunity to magnetically control the polarization and electrically control the magnetization. Such materials can be found in nature rarely, but they can be fabricated by modern material design techniques, e.g. as the composition of FMs and FEs. Therefore MFs are also our interest.

In chapters 2-3 we deal with FMs and in chapter 4 with FEs. Chapter 5 is about MFs.

1.3 Scales and Methods

Depending on the scale of interest, different formalisms have been proposed to treat the systems. Due to miniaturization of devices nowadays, we are interested in the scales between nm and μm . We will operate in a regime where one can neglect quantum effects. Thermal fluctuations are introduced as noise to the equations of motion for magnetization and polarization. This means that we deal with stochastic differential equations (SDEs). The way we treat them is given in details in the chapters. Due to the complexity of equations, especially in extended systems, we use numerical methods to solve them.

1.4 Phenomena of Interest

When it comes to FMs and FEs, thermal effects are very diverse. Among them, in chapter 3 we specifically address spin Seebeck effect (SSE) in which a temperature gradient over a FM is used to generate a spin current. This phenomenon not only can be considered as a way to recover waste heat, but also can be considered as a spin current source which itself can be used in low-energy consuming devices.

In chapter 4 we address the pyroelectric effect in which the temperature-dependency of hysteresis loops in FEs is used to harvest thermal energy.

Finally, in chapter 5 we combine our experiences with FMs and FEs to study MFs. We address some of the possible functionalities of these materials in terms of thermal effects. In line with our motivation and goals, we propose a thermomagnetolectric engine to use a magnetic field to steer the operation of pyroelectric engines.

Beside the mentioned phenomena which are directly related to the thermal energy harvesting, we simulate some other interesting temperature-related phenomena such as thermally activated switching times in FMs and FEs, spin-current driven domain-wall motion, phase instability in reduced-size FE domains, and a MF thermal diode.

¹<http://www.aps.org>

2 Thermal Fluctuations in Magnetic Systems

Ferromagnets (FMs) are materials that possess a spontaneous magnetization (magnetic moment per volume) below a certain temperature known as Curie temperature T_c (Fig. 2.1). Within such a simple definition, we can recognize the importance of the interplay between magnetization and temperature. Here we want to go more into details of this interplay, but in the regimes far below the Curie temperature. We will see that even in such regimes the thermal fluctuations lead to interesting phenomena especially at nanoscales.

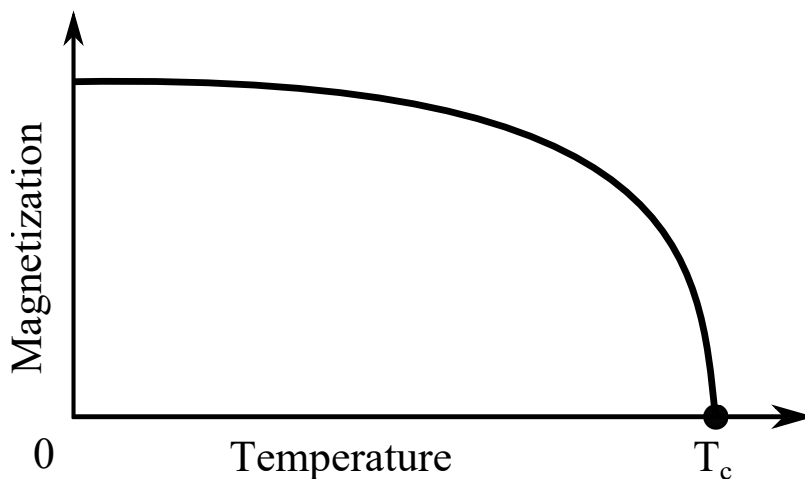


Figure 2.1: A typical ferromagnet-paramagnet phase transition diagram at zero external magnetic field. Below the Curie temperature (T_c) the system is in FM phase with a spontaneous magnetization while above that it is in paramagnet phase.

We start from the fundamental object in ferromagnetism i.e. a magnetic moment and see how the temperature can affect its dynamics. Generally speaking, a magnetic field is the generic way a magnetic moment can be influenced from the outside world. Even when it comes to the interplay of a magnetic moment and temperature we will see that the temperature should be translated in terms of a magnetic field to affect the magnetic moment. Therefore, we start with the dynamics of a single magnetic moment in the presence of an external magnetic field. To go to more complicated systems we need to just consider the *effective* magnetic field acting on the magnetic moments.

2.1 A Theoretical Perspective to Thermal Fluctuations in Magnetic Systems

According to the classical mechanics, the dynamics of an angular momentum (\vec{l}) of a magnetic moment ($\vec{\mu}$) is determined by the torque acting on it [1] :

$$\frac{d\vec{l}}{dt} = \vec{\mu} \times \vec{H}, \quad (2.1)$$

where \vec{H} in principle is the effective magnetic field, but here for the sake of simplicity we assume it is a fixed external magnetic field. Since the angular momentum and magnetic moment are connected via gyromagnetic ratio $\vec{\mu} = \gamma\vec{l}$, the equation of motion for the magnetic moment reads :

$$\frac{d\vec{\mu}}{dt} = \gamma\vec{\mu} \times \vec{H}. \quad (2.2)$$

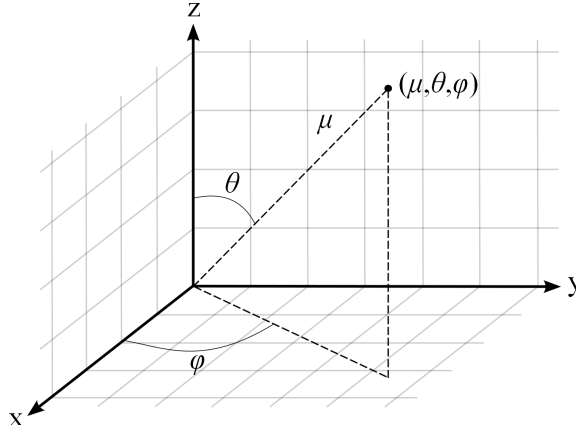


Figure 2.2: The representation of a magnetic moment in spherical coordinates.

Within all this thesis, γ is a positive quantity, though in principle angular momentum and magnetic moment can have opposite sign as well. To solve this equation, due to symmetry of the system, it would be better to write it in spherical coordinates (see Fig. 2.2) :

$$\begin{aligned} \dot{\mu} &= 0, \\ \dot{\theta} &= 0, \\ \dot{\phi} &= -\gamma H_0, \end{aligned} \quad (2.3)$$

where it is assumed $\vec{H} = H_0\hat{z}$. It means that the magnetic moment just rotates around the magnetic field with the so-called *Larmor* precession frequency γH_0 . Since the angle between the magnetic moment and the field remains fixed, the energy of the magnetic moment $\varepsilon^m = -\vec{\mu} \cdot \vec{H}$ is preserved in this case. This gives us a hint on how we can couple our system to a heat bath and other dissipative sources. The $\varepsilon^m = -\vec{\mu} \cdot \vec{H}$ says in order to

have dissipation we need an extra torque to change the angle between magnetic moment and the magnetic field. Such torque can have the following form (Fig. 2.3) :

$$\vec{\tau}^{damping} = -\frac{\alpha}{\mu} \vec{\mu} \times (\vec{\mu} \times \vec{H}), \quad (2.4)$$

where α determines the strength of coupling of dissipative sources to the magnetic moment and is known as the damping parameter. For the moment, we assume this torque summarizes the effect of all dissipative forces that act on the magnetic moment. In the case that the dissipation stems from thermal fluctuations, α determines the strength of coupling of the system to the heat bath where in the case of FM insulators it is a phonon subsystem. In the case of interacting magnetic moments, however, the energy of each magnetic moment can be transferred to others to generate spin waves (but even in this case the energy of the magnetic system is eventually transferred to the lattice).

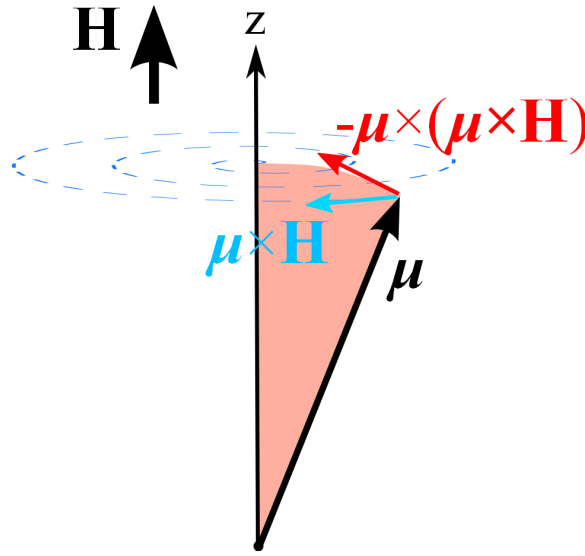


Figure 2.3: Magnetic moment dynamics in the presence of an external magnetic field and dissipative sources. The blue arrow is the corresponding torque to the Larmor precession and the red arrow is the corresponding torque to the dissipative forces.

With the provided extra torque (Eq. (2.4)), now we can write the equation of motion for the magnetic moment as :

$$\frac{d\vec{\mu}}{dt} = \gamma \vec{\mu} \times \left(\vec{H} - \frac{\alpha}{\mu} \vec{\mu} \times \vec{H} \right), \quad (2.5)$$

which in spherical coordinates reads :

$$\begin{aligned} \dot{\mu} &= 0, \\ \dot{\theta} &= -\gamma \alpha H_0 \sin(\theta), \\ \dot{\varphi} \sin(\theta) &= -\gamma H_0 \sin(\theta). \end{aligned} \quad (2.6)$$

As can be seen, the employed dissipative torque (Eq. (2.4)) still keeps the length of the magnetic moment fixed. So this kind of damping is called *transverse* damping (in contrast to longitudinal damping [2, 3]). In case that $\theta = 0$ or π there is no dynamic, so we consider the case that $\theta \neq 0, \pi$. The third equation gives the Larmor frequency as before γH_0 . According to the second equation :

$$-\gamma\alpha H_0 t = \int_{\theta_0}^{\theta} \frac{d\theta'}{\sin(\theta')} = -\ln\left(\frac{1}{\sin(\theta)} + \frac{\cos(\theta)}{\sin(\theta)}\right) + \ln\left(\frac{1}{\sin(\theta_0)} + \frac{\cos(\theta_0)}{\sin(\theta_0)}\right), \quad (2.7)$$

which after some straightforward calculation yields $\cos(\theta)$ and so the dynamics of the z component of magnetic moment :

$$\mu_z(t) = \mu \cos(\theta) = \mu \frac{-1 + \frac{1 + \frac{\mu_z(0)}{\mu}}{1 - \frac{\mu_z(0)}{\mu}} \exp(2\gamma\alpha H_0 t)}{+1 + \frac{1 + \frac{\mu_z(0)}{\mu}}{1 - \frac{\mu_z(0)}{\mu}} \exp(2\gamma\alpha H_0 t)}. \quad (2.8)$$

The time evolution of the magnetic energy is

$$\varepsilon^m = -\vec{\mu} \cdot \vec{H} = -\mu H_0 \frac{-1 + \frac{1 + \frac{\mu_z(0)}{\mu}}{1 - \frac{\mu_z(0)}{\mu}} \exp(2\gamma\alpha H_0 t)}{+1 + \frac{1 + \frac{\mu_z(0)}{\mu}}{1 - \frac{\mu_z(0)}{\mu}} \exp(2\gamma\alpha H_0 t)}, \quad (2.9)$$

meaning that the magnetic moment loses energy while relaxing to the direction of magnetic field. The speed of damping depends on α , meaning that as the coupling between the magnetic moment and the dissipative sources becomes stronger the dissipation of energy is faster.

So far we just introduced a damping term (Eq. (2.4)) to show how the energy of our magnetic system could be dissipated and we did not explicitly refer to the temperature. When the system is in contact with thermal baths, this damping torque is the average effect of thermal fluctuations. Therefore, in order to go one step further to establish a relation between temperature and magnetic moment dynamics, we should include the random impact of environment into the equation of motion. Formulation of such a problem (having a random magnetic field) brings us to a new type of differential equations known as stochastic differential equations (SDEs) (in Sec. 4.4 a deterministic approach is also provided briefly). Before approaching such equations we remind that in principle in classical physics we are dealing with a deterministic world and by stochastic we just mean that we are not interested in going into details of all the environmental factors that affect our system. We intend to eliminate the microscopic degrees of freedom of the environment by substitution of a stochastic field (noise). To cover this simplification to some extent, we calculate the averaged value of desired quantities over different realization of the noises (ensemble averages, which we will denote by $\langle \dots \rangle$).

2.1.1 Stochastic Differential Equations and Fokker-Planck Equation

We can divide the random impact of the environment in two parts; a dissipative term and a random term. This dissipative term and the random field, however, are expected to be

related since both come from the same origin which is the random impact of the environment (this is, in fact, the manifestation of the so-called fluctuation-dissipation theorem which finally helps us to establish the relation between temperature, random magnetic field $\vec{\xi}$ and damping parameter [4]). We assume the random impact of the environment is not too strong to change the magnitude of the magnetic moment and so Eq. (2.5) is modified as :

$$\frac{d\vec{\mu}}{dt} = -\frac{\gamma}{1+\alpha^2}\vec{\mu} \times \left[\left(\vec{H} + \vec{\xi}(t) \right) + \frac{\alpha}{\mu}\vec{\mu} \times \left(\vec{H} + \vec{\xi}(t) \right) \right], \quad (2.10)$$

in which here μ is assumed to be the atomic magnetic moment stemming from unpaired electrons (therefore, angular momentum and magnetic moment have opposite sign [5]). This equation which is the basis of the atomistic spin model simulations is known as the atomistic Landau-Lifshitz-Gilbert (LLG) equation [6–8] (see Sec. 5.1) and belongs to the family of Langevin equations [9]. Depending on the circumstances, different distributions can be considered for this random magnetic field. However, in most cases a Gaussian-white is appropriate with the following properties :

$$\langle \xi_i(t) \rangle = 0, \quad \langle \xi_i(t') \xi_j(t) \rangle = b \delta_{ij} \delta(t - t'), \quad (2.11)$$

where i, j stand for three different components of the random field as a vector and b shows how strong is the random field. Due to the central limit theorem [10], in most situations the Gaussian distribution is the best choice to mimic the real world where the random field is the cumulative effect of numerous uncorrelated environmental factors. It is called *white* because the Fourier transform of the autocorrelation is constant (due to Dirac delta function), meaning all frequencies have the same amplitude. It is a completely random process with no memory at all, assuming that the environment varies much faster than the system [11]. In this sense, a better distribution is needed when it comes to for instance study of ultra-fast laser pulses on magnetization dynamics (see Sec. 3.5).

Coming back to the calculation of ensemble average of $\mu_z(t)$, obviously, we can write

$$\langle \mu_z(t) \rangle = \langle \mu \cos(\theta) \rangle = \int_0^{2\pi} \int_0^\pi \mu \cos(\theta) \Omega(\theta, \varphi, t) \sin(\theta) d\theta d\varphi, \quad (2.12)$$

where $\Omega(\theta, \varphi, t)$ is the probability of finding the magnetic moment at time t in (θ, φ) direction. The governing equation for the time evolution of this probability is known as Fokker-Planck equation (FPE) which, generally speaking, is the basis for the statistical description of the ensemble of systems where each one is described by a Langevin equation. Here we follow the Kramers-Moyal recipe given in Ref. [9] to find the corresponding FPE. In a general coordinate system $\{\psi\}$, the Kramers-Moyal expansion reads :

$$\begin{aligned} \frac{\partial}{\partial t} \Omega + \frac{1}{\prod_{m=1} l_m} \sum_{i=1} \frac{\partial}{\partial \psi_i} \left(\frac{\prod_{j=n} l_n}{l_i} D_i^{(1)}(\{\psi\}, t) \Omega \right) \\ - \frac{1}{\prod_{i=m} l_m} \sum_{i,j=1} \frac{\partial}{\partial \psi_i} \left(\frac{\prod_{j=n} l_n}{l_i l_j} \frac{\partial}{\partial \psi_j} D_{ij}^{(2)}(\{\psi\}, t) \Omega \right) = 0, \end{aligned} \quad (2.13)$$

where $l_i^2(\{\psi\})$ are the diagonal elements of the metric [12] and

$$\begin{aligned} D_i^{(1)}(\{\psi\}, t) &= h_i(\{\psi\}, t) + \frac{b}{2} g_{kj}(\{\psi\}, t) \frac{\partial}{\partial \psi_k} g_{ij}(\{\psi\}, t), \\ D_{ij}^{(2)}(\{\psi\}, t) &= \frac{b}{2} g_{ik}(\{\psi\}, t) g_{jk}(\{\psi\}, t), \end{aligned} \quad (2.14)$$

are the drift and diffusion coefficients respectively. h_i and g_{ij} are provided by the Langevin equation of the form $\dot{\psi}_i = h_i(\{\psi\}, t) + g_{ij}(\{\psi\}, t) \xi_j(t)$. Because of the symmetry of the system we use the spherical coordinate with $[l_\mu \ l_\theta \ l_\varphi] = [1 \ \mu \ \mu \sin(\theta)]$ in which Eq. (2.10) reads :

$$\begin{aligned} \dot{\mu} &= 0, \\ \mu \dot{\theta} &= -\frac{\mu \gamma \alpha H_0}{1 + \alpha^2} \sin(\theta) + \frac{\mu \gamma \alpha}{1 + \alpha^2} \eta_\theta + \frac{\mu \gamma}{1 + \alpha^2} \eta_\varphi, \\ \mu \dot{\varphi} \sin(\theta) &= +\frac{\mu \gamma H_0}{1 + \alpha^2} \sin(\theta) - \frac{\mu \gamma}{1 + \alpha^2} \eta_\theta + \frac{\mu \gamma \alpha}{1 + \alpha^2} \eta_\varphi, \end{aligned} \quad (2.15)$$

and so

$$\begin{bmatrix} h_r \\ h_\theta \\ h_\varphi \end{bmatrix} = \frac{\mu \gamma H_0}{1 + \alpha^2} \sin(\theta) \begin{bmatrix} 0 \\ -\alpha \\ 1 \end{bmatrix}, \quad \begin{bmatrix} g_{rr} & g_{r\theta} & g_{r\varphi} \\ g_{\theta r} & g_{\theta\theta} & g_{\theta\varphi} \\ g_{\varphi r} & g_{\varphi\theta} & g_{\varphi\varphi} \end{bmatrix} = \frac{\mu \gamma}{1 + \alpha^2} \begin{bmatrix} 0 & 0 & 0 \\ 0 & \alpha & 1 \\ 0 & -1 & \alpha \end{bmatrix},$$

which give us the drift and diffusion coefficients :

$$\begin{bmatrix} D_r^{(1)} \\ D_\theta^{(1)} \\ D_\varphi^{(1)} \end{bmatrix} = \frac{\mu \gamma H_0}{1 + \alpha^2} \sin(\theta) \begin{bmatrix} 0 \\ -\alpha \\ 1 \end{bmatrix}, \quad \begin{bmatrix} D_{rr}^{(2)} & D_{r\theta}^{(2)} & D_{r\varphi}^{(2)} \\ D_{\theta r}^{(2)} & D_{\theta\theta}^{(2)} & D_{\theta\varphi}^{(2)} \\ D_{\varphi r}^{(2)} & D_{\varphi\theta}^{(2)} & D_{\varphi\varphi}^{(2)} \end{bmatrix} = \frac{b(\mu \gamma)^2}{1 + \alpha^2} \begin{bmatrix} 0 & 0 & 0 \\ 0 & 1 & 0 \\ 0 & 0 & 1 \end{bmatrix}.$$

Substituting the above coefficients in the Kramers-Moyal expansion (Eq. (2.13)) the FPE is derived as

$$\begin{aligned} \frac{\partial}{\partial t} \Omega(\theta, \varphi, t) &= \frac{\gamma}{1 + \alpha^2} \frac{1}{\sin(\theta)} \frac{\partial}{\partial \theta} \left[\sin(\theta) \left(\alpha H_0 \sin(\theta) \Omega(\theta, \varphi, t) + \gamma \frac{b}{2} \frac{\partial}{\partial \theta} \Omega(\theta, \varphi, t) \right) \right] \\ &\quad - \frac{\gamma}{1 + \alpha^2} \frac{1}{\sin(\theta)} \frac{\partial}{\partial \varphi} \left[H_0 \sin(\theta) \Omega(\theta, \varphi, t) - \gamma \frac{b}{2} \frac{1}{\sin(\theta)} \frac{\partial}{\partial \varphi} \Omega(\theta, \varphi, t) \right]. \end{aligned} \quad (2.16)$$

To find the relation between b and the damping parameter (α) we impose the stationary condition ($\frac{\partial}{\partial t} \Omega(\theta, \varphi, t \rightarrow \infty) = 0$) on the derived Fokker-Planck equation. In such a case we expect the Boltzmann distribution is built in ($\Omega(\theta, \varphi) = \exp(\mu H_0 \cos(\theta)/k_B T)$) which leads to

$$b = \frac{2\alpha k_B T}{\gamma \mu}. \quad (2.17)$$

As expected b depends on the strength of coupling of the magnetic system to the heat bath i.e. damping parameter α . Here T is the temperature of the environment whose microscopic degrees of freedom have been replaced by the noise. In this thesis by the environment we mainly mean phonon subsystem (although in metallic FMs the electrons

also should be included) and so T introduced into the autocorrelation function is in fact phonon temperature. Putting back b in the derived FPE we reach exactly the one derived by Brown [13].

Now we come back to Eq. (2.12)

$$\begin{aligned} \frac{d}{dt}\langle\mu_z\rangle &= \mu \frac{d}{dt} \int_0^{2\pi} \int_0^\pi \cos(\theta)\Omega(\theta, \varphi, t) \sin(\theta) d\theta d\varphi \\ &= \mu \int_0^{2\pi} \int_0^\pi \cos(\theta) \sin(\theta) \frac{\partial}{\partial t} \Omega(\theta, \varphi, t) d\theta d\varphi. \end{aligned} \quad (2.18)$$

Replacing $\frac{\partial}{\partial t}\Omega(\theta, \varphi, t)$ from Eq. (2.16) and integrating by part twice and considering $\int_0^{2\pi} \int_0^\pi \sin(\theta)\Omega(\theta, \varphi, t) d\theta d\varphi = 1$ we find the equation of motion for the averaged z-component of the magnetic moment :

$$\frac{d}{dt}\langle\mu_z\rangle = \frac{\alpha\gamma}{\mu(1+\alpha^2)} \left[-2k_B T \langle\mu_z\rangle + H_0 (\mu^2 - \langle\mu_z^2\rangle) \right], \quad (2.19)$$

which represents the competition between thermal and magnetic energies to determine the state of the system. This equation cannot be solved independently because of $\langle\mu_z^2\rangle$. Again using Eq. (2.16) we have

$$\begin{aligned} \frac{d}{dt}\langle\mu_z^2\rangle &= \mu^2 \int_0^{2\pi} \int_0^\pi \cos^2(\theta) \sin(\theta) \frac{\partial}{\partial t} \Omega(\theta, \varphi, t) d\theta d\varphi \\ &= \frac{2\alpha\gamma}{1+\alpha^2} \left[H_0 \mu \langle\mu_z\rangle - \frac{H_0}{\mu} \langle\mu_z^3\rangle + \mu k_B T - \frac{3k_B T}{\mu} \langle\mu_z^2\rangle \right], \end{aligned} \quad (2.20)$$

that depends on $\langle\mu_z^3\rangle$ which calls for numerical analysis of SDEs. However, at least we can consider a simple case $\langle\mu_z^2\rangle \approx \langle\mu_z\rangle^2$. In such a case Eq. (2.19) can be solved as

$$\langle\mu_z\rangle \approx \mu \left(\frac{-1 + A(t)}{+1 + A(t)} \sqrt{1 + \left(\frac{k_B T}{\mu H_0}\right)^2} - \frac{k_B T}{\mu H_0} \right), \quad (2.21)$$

where

$$A(t) = \frac{+\frac{k_B T}{\mu H_0} + \sqrt{1 + \left(\frac{k_B T}{\mu H_0}\right)^2} + \frac{\mu_z(0)}{\mu}}{-\frac{k_B T}{\mu H_0} + \sqrt{1 + \left(\frac{k_B T}{\mu H_0}\right)^2} - \frac{\mu_z(0)}{\mu}} \exp \left(\frac{2\alpha\gamma H_0}{1 + \alpha^2} \sqrt{1 + \left(\frac{k_B T}{\mu H_0}\right)^2} t \right). \quad (2.22)$$

At $T = 0$ Eq. (2.21) reduces to the Eq. (2.8), considering that in Eq. (2.10) we have a factor of $(1 + \alpha^2)^{-1}$.

2.2 Landau-Lifshitz-Gilbert Equation

Up to now we were talking about one magnetic moment. In larger systems, a huge number of magnetic moments are coupled together. Thus, dealing with the corresponding SDEs would be a real challenge. At low enough temperatures the magnetic moments are strongly tight together, however, we still can keep the provided formalism in the previous section. Just we need to replace the magnetic moment in Eq. (2.10) by $a^3 \vec{M}$ where a^3 and \vec{M} are the volume which includes coupled magnetic moments and magnetization (magnetic moment per volume) respectively. In such a case, the equation of motion for the magnetization reads

$$\frac{d\vec{M}}{dt} = -\frac{\gamma}{1+\alpha^2} \vec{M} \times \left[\left(\vec{H} + \vec{\xi}(t) \right) + \frac{\alpha}{M_S} \vec{M} \times \left(\vec{H} + \vec{\xi}(t) \right) \right], \quad (2.23)$$

which is nothing but the phenomenological LLG equation with phenomenological damping parameter α known as Gilbert damping (which in principle is different from α in atomistic LLG equation). Additionally, in the case that $\vec{\xi}$ is Gaussian white noise, again we have :

$$\langle \xi_i(t) \rangle = 0, \quad \langle \xi_i(t') \xi_j(t) \rangle = \frac{2\alpha k_B T}{\gamma a^3 M_S} \delta_{ij} \delta(t - t'), \quad (2.24)$$

where M_S is the absolute value of the magnetization. As mentioned, this formalism is valid as long as the damping is transversal, meaning that the temperature must be much lower than the Curie temperature so that the temperature will not be able to change the absolute value of magnetization. Moreover, when the magnetic moments are strongly coupled together, the relative magnetic moment direction of the neighboring atoms can be assumed to be fixed and allows us to treat the magnetization as a continuum vector field $\vec{M}(\vec{r}, t)$. This treatment is known as micromagnetism simulations which can properly describe many magnetic phenomena at length scales between nm and μm . For smaller scales quantum theory, atomistic model, etc. are used while for larger scales domain theory and macroscopic models are appropriate. The transition from atomistic spin model to micromagnetism is, therefore, a transition from a discrete representation of magnetic structures as spins or magnetic moments to a continuum representation of magnetic structures by considering a smooth magnetization vector field [14]. To represent this continuity more explicitly we write LLG equation in the following form :

$$\frac{\partial \vec{M}(\vec{r}, t)}{\partial t} = -\frac{\gamma}{1+\alpha^2} \vec{M}(\vec{r}, t) \times \left[\vec{H}^{eff}(\vec{r}, t) + \frac{\alpha}{M_S} \vec{M}(\vec{r}, t) \times \vec{H}^{eff}(\vec{r}, t) \right], \quad (2.25)$$

where $\vec{H}^{eff} = -\frac{\partial F}{\partial \vec{M}} + \vec{\xi}(\vec{r}, t)$ includes all the fields which affect the magnetization such as thermal noise ($\vec{\xi}$) with the autocorrelation $\langle \xi_i(\vec{r}', t') \xi_j(\vec{r}, t) \rangle = \frac{2\alpha k_B T}{\gamma M_S} \delta_{ij} \delta(\vec{r} - \vec{r}') \delta(t - t')$, external magnetic field, exchange, anisotropy, etc. which are hidden in $-\frac{\partial F}{\partial \vec{M}}$. F is the micromagnetic free energy density of the system. It is worth to mention that the LLG equation can be straightforwardly derived from Gilbert equation [14, 15] :

$$\frac{\partial \vec{M}(\vec{r}, t)}{\partial t} = -\gamma \vec{M}(\vec{r}, t) \times \vec{H}^{eff}(\vec{r}, t) + \frac{\alpha}{M_S} \vec{M}(\vec{r}, t) \times \frac{\partial \vec{M}(\vec{r}, t)}{\partial t}, \quad (2.26)$$

under the assumption that the absolute value of magnetization is fixed ($\vec{M} \cdot \frac{\partial \vec{M}}{\partial t} = 0$). At high temperatures where the magnitude of magnetization changes, the sole transverse

damping term cannot describe the dynamics of the magnetic system properly and a longitudinal damping parameter is also needed. In such a case the Landau-Lifshitz-Bloch equation is used which is beyond the scope of this thesis [2, 3, 16, 17].

To get the magnetization dynamics using the LLG equation we can follow the previous section procedure to calculate FPE. But as we found there, it is not feasible even for a simple system. Since we are going in the direction of larger systems which includes the coupled magnetic domains the situation becomes even worse. Therefore, in this thesis we solve the LLG equations numerically using Langevin dynamics [18–20].

2.3 A Numerical Perspective to Thermal Fluctuations in Magnetic Systems

As seen in Sec. 2.1.1, dealing analytically with stochastic differential equations, even for very simple models, is a challenge. So for complicated systems we resort to numerical analysis. To do so, we start from Eq. (2.25) and evaluate the time propagation of magnetization by a direct integration over a discrete time path $\{t_0, t_1, t_2, \dots\}$ where $t_m - t_{m-1} = \Delta t$ is the numerical time step. In the case of multi-domain systems, we need to discretize the system in space as well $\{\vec{M}_1(t_m), \vec{M}_2(t_m), \vec{M}_3(t_m), \dots\}$ so that

$$\vec{M}_n(t_m) = \vec{M}_n(t_{m-1}) - \frac{\gamma}{1 + \alpha^2} \vec{M}_n(t_m) \times \left[\vec{H}_n^{eff}(t_m) + \frac{\alpha}{M_S} \vec{M}_n(t_m) \times \vec{H}_n^{eff}(t_m) \right] \Delta t, \quad (2.27)$$

with

$$\vec{H}_n^{eff}(t_m) = -\frac{\partial F}{\partial \vec{M}_n(t_m)} + \left(\sqrt{\frac{2\alpha k_B T}{\gamma a^3 M_S \Delta t}} \frac{1}{\Delta t} \right) \vec{\zeta}_n(t_m), \quad (2.28)$$

where $\zeta_n^{x,y,z}(t_m)$ are independent radome numbers with standard normal distribution (mean zero and unit variance) (see Fig. 2.6c) and a^3 is the volume of each domain. This gives us just the numerical solution of LLG equations for one realization of the noises. In the event we are interested in thermal averages (ensemble averages) of the quantities, we need to solve the LLG equations for different realization of the noises with the same initial conditions and then take the average over all trajectories (though in the equilibrium state, for the ergodic systems the time average will give the same value as the ensemble average [21]).

In the following, we numerically solve the LLG equations for two different simple systems in which the theoretical values for our quantities are available; to assess the quality of our simulations. As the first example, we calculate the thermal average of magnetization for the equilibrium state. As the second example, we calculate the mean-first-passage time in magnetization switching.

2.3.1 First Example : Thermal Average of Magnetization at Equilibrium

We address a single domain with free energy density of

$$F = -H_0 M^z, \quad (2.29)$$

where $H_0 = 0.005$ [T] is the external magnetic field. Our goal is to calculate the thermal average of the equilibrium magnetization at different temperatures. Theoretically, we know that the interaction of the magnetic system with the heat bath leads to the population of excited states whose probability, depending on their equilibrium configuration, is given by the Boltzmann distribution $\exp(-E/k_B T)$ so that the thermal average of the

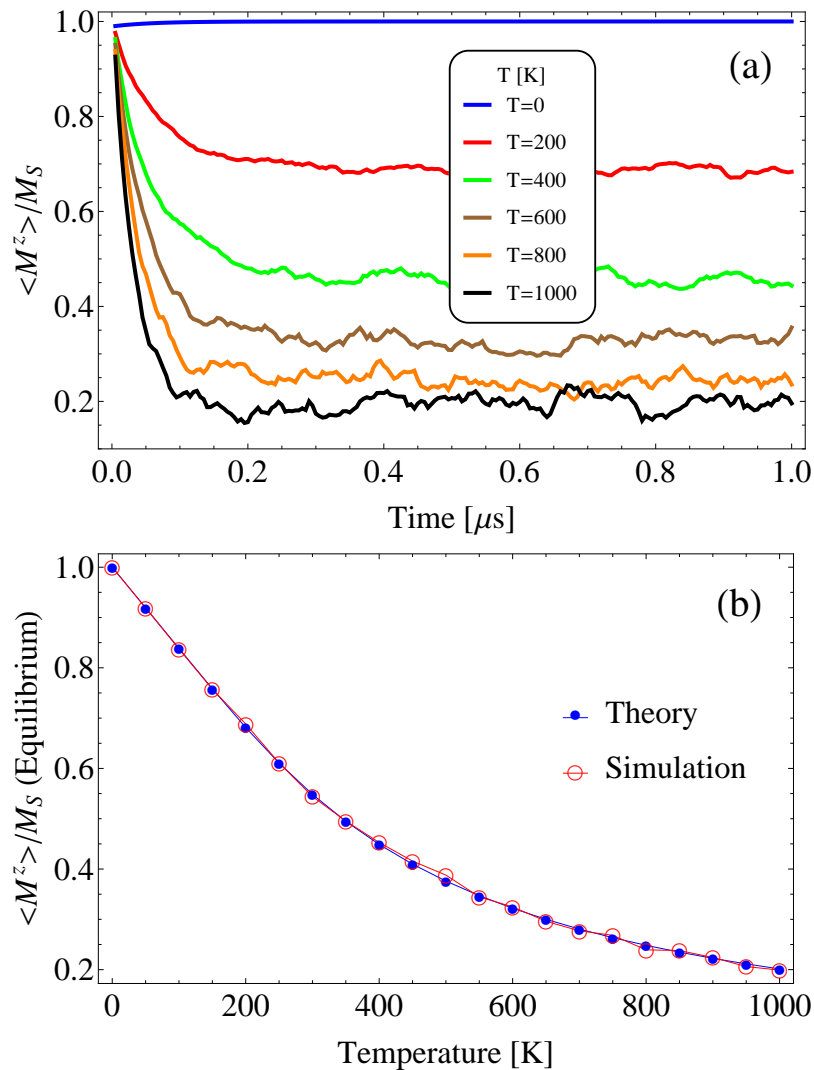


Figure 2.4: a) Trajectory of averaged reduced magnetization for a single FM domain for different temperatures are shown. To obtain them, Eq. (2.25) was solved numerically for 1000 realization of the noises and then averaged. b) The value of $\langle M^z \rangle / M_S$ when the system is relaxed versus the temperature are shown and compared with the theoretical values.

magnetization reads :

$$\langle M^z \rangle = M_S \langle \cos(\theta) \rangle = M_S \frac{\int_0^\pi \cos(\theta) \exp(a^3 M_S H_0 \cos(\theta)/k_B T) d\theta}{\int_0^\pi \exp(a^3 M_S H_0 \cos(\theta)/k_B T) d\theta} = M_S L\left(\frac{a^3 M_S H_0}{k_B T}\right), \quad (2.30)$$

where $L(x) = \coth(x) - \frac{1}{x}$ is the Langevin function [21]. For $M_S = 1.71 \times 10^6$ [A/m], $a = 10$ [nm] and $\alpha = 0.01$ the trajectory of the averaged magnetization calculated numerically is shown in Fig. 2.4a. The equilibrium magnetization is reached when its value becomes time-independent (roughly). Calculating the equilibrium magnetization for different temperatures we have Fig. 2.4b which confirms that our simulations give the correct equilibrium state of the system.

2.3.2 Second Example : Thermally Activated Magnetization Switching

Another interesting quantity is the mean-first-passage time (MFPT). It is the time that it takes for the system to pass a potential barrier due to thermal fluctuations and goes from one well to another well (see Fig. 2.5a). Here we consider a single FM domain with the following free energy density

$$F = \frac{k}{M_S^2} (M_S^2 - (M^z)^2), \quad (2.31)$$

where $k = 48$ [kJm⁻³] is the uniaxial anisotropy constant which results in two energy minima at $M^z = \pm M_S$. For $M_S = 1.7 \times 10^6$ [A/m], $a = 5$ [nm] and $\alpha = 0.01$ the trajectory of the reduced magnetization at $T = 80$ [K] is shown in Fig. 2.5a (numerical solution of LLG equation just for one realization of the noises). Theoretically $MFPT = \frac{\Omega}{\partial\Omega/\partial t}$, where Ω is the probability and is given by FPE (Eq. (2.16)). Following this instruction one can get the theoretical formula for MFPT [22] :

$$MFPT = \frac{1}{2} \frac{a^3 M_S (1 + \alpha^2) \sqrt{\pi} \exp(ka^3/k_B T)}{2\gamma\alpha k_B T (ka^3/k_B T)^{3/2}}. \quad (2.32)$$

The theoretical values for MFPT and numerically evaluated ones are compared in Fig. 2.5b which confirm that our simulations give the correct dynamics. As can be understood the competition between anisotropy energy ka^3 and thermal energy $k_B T$ determines the MFPT. For very small-volume domains the MFPT is expected to be very short and therefore their measured magnetization (time average) is expected to be zero. Due to such a property, such a small FM domains are called *superparamagnet*.

2.3.3 Some Details about Numerical Procedure

Stochastic Integration : To obtain the time propagation of a desired quantities in the presence of thermal fluctuations, using Langevin dynamics [18], we need to take

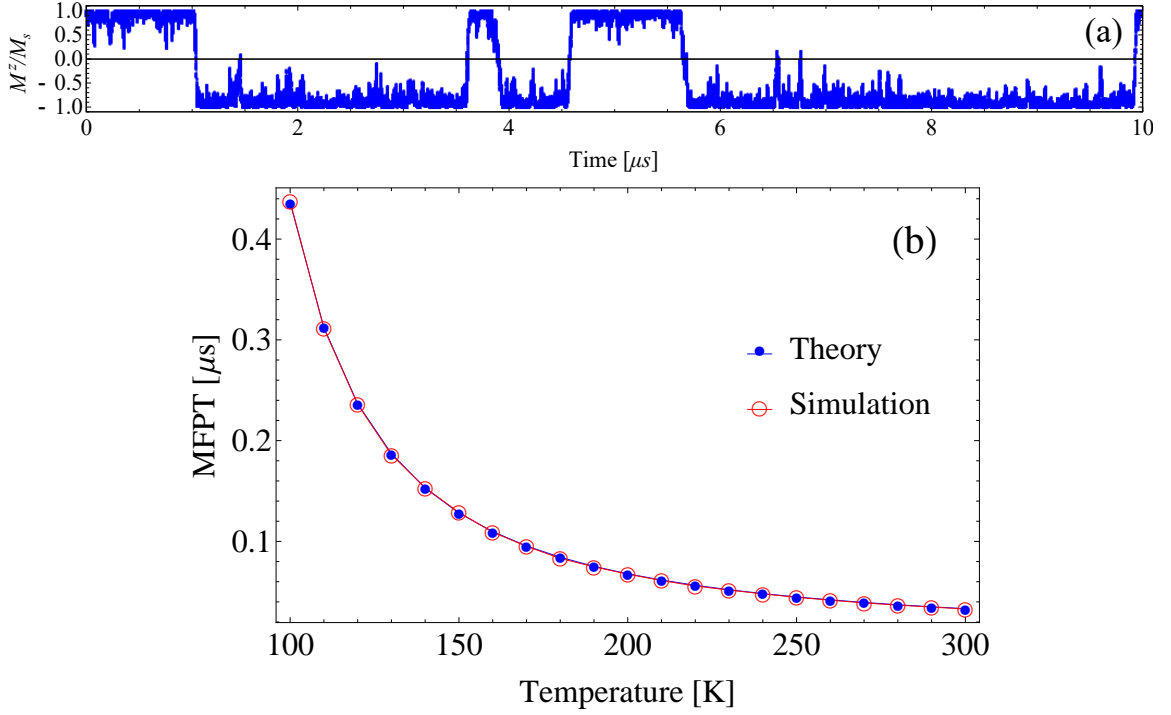


Figure 2.5: Trajectory of the z component of reduced magnetization of a single ferromagnetic domain at $T = 80$ [K] for a simulation time of 10 $[\mu s]$ is shown. The MFPT is evaluated by averaging over the times that the system spends in potential wells. b) MFPT versus temperature is evaluated and compared with theory (Eq. (2.32)). At low temperatures MFPT is large and so to get more accurate results the simulation time should be increased so that the averages are taken over more numbers of switchings. Here the simulation time is 10000 $[\mu s]$.

the integral of SDEs. Generally speaking, to integrate a stochastic function, $\Upsilon(t) = \int_0^t \xi(t')G(t')dt'$, we can follow two routes which yield two different dynamical properties : Ito and Stratonovich [9]. To see this we rewrite $\Upsilon(t)$ in the sense of Riemann-Stieltjes integral :

$$\Upsilon(t) = \int_0^t G(t')dw(t'), \quad (2.33)$$

where $w(t) = \int_0^t \xi(t')dt' = \int_0^t dw(t')$ is a Wiener process. Then we parameterize the integral by $0 \leq \lambda \leq 1$ as following :

$$\Upsilon_n^\lambda(t) = \sum_{j=1}^n G[(1-\lambda)t_{j-1} + \lambda t_j] (w(t_j) - w(t_{j-1})), \quad (2.34)$$

where $t_j = j \frac{t}{n}$. λ determines the position where $G[t]$ is evaluated within the time step interval $[t_{j-1}, t_j]$. In the limit of $n \rightarrow \infty$ a deterministic integral becomes independent of λ , however for the case of stochastic integrals the choice of λ is not arbitrary and different

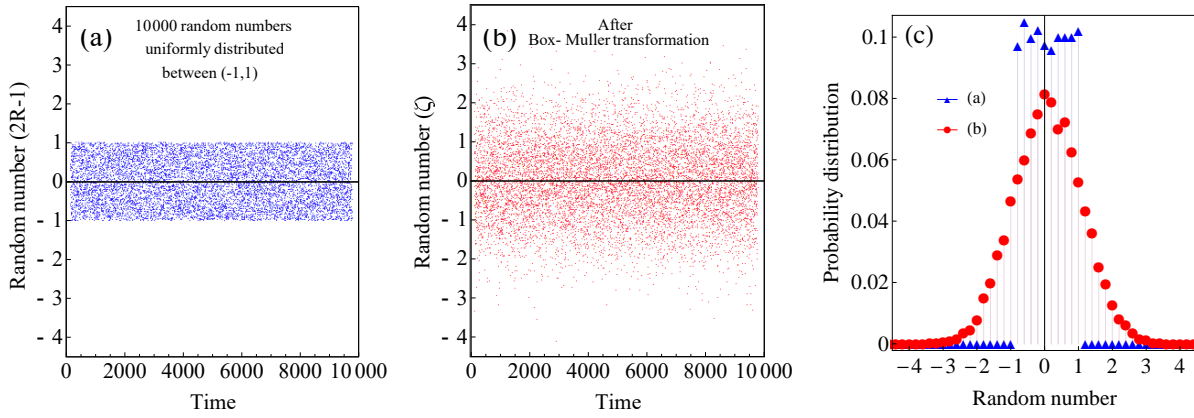


Figure 2.6: (a) 10000 random numbers generated by C++ library (*srand*) with a uniform distribution. (b) Transforming the generated numbers with uniform distribution to standard normal distribution. (c) The corresponding probability distribution of random numbers before the transformation (uniform distribution) and after transformation (standard normal distribution) are shown. As can be seen the probability of standard normal distribution in the $(-0.1, 0.1)$ interval is more or less equal to $\int_{-0.1}^{0.1} \frac{e^{-\frac{x^2}{2}}}{\sqrt{2\pi}} dx \simeq 0.08$. As the number of random numbers increases the better (more accurate) standard normal distribution is achieved.

λ s yield different dynamical properties for the system. The value of λ has to be justified based on the physical processes. Ito scheme refers to $\lambda = 0$ and Stratonovich scheme refers to $\lambda = 1/2$. The Stratonovich calculus is usually preferred in physical applications [9]. In this thesis, we also use Stratonovich scheme to integrate LLG equations. Using the *Heun* method for numerical integration we can achieve that [18, 23].

Gaussian (Normal) White Noise : As mentioned earlier for Eq. (2.28), to introduce Gaussian white noise distribution we need to generate random numbers with a standard normal distribution. The noise is already adjusted to be *white* by putting Δt in the denominator of the strength of the noise in Eq. (2.28). To have *Gaussian* property as well, assuming we have already generated random numbers with uniform distribution, we can use *Box-Muller transformation* to generate a standard normal distribution out of the uniform one [24] :

Method : Let R, R' be independent random numbers with uniform distribution on the interval $(0, 1)$. Performing the following transformation :

$$\begin{aligned}\zeta &= (-2 \ln R)^2 \cos(2\pi R'), \\ \zeta' &= (-2 \ln R)^2 \sin(2\pi R'),\end{aligned}\tag{2.35}$$

then ζ, ζ' will be independent random numbers with a standard normal distribution (Fig. 2.6).

3 Spin Seebeck Effect

Among many thermal effects in FMs, in this chapter we address the spin Seebeck effect (SSE). SSE refers to the generation of a spin current due to a temperature gradient and in analogy with the conventional Seebeck effect is called *spin* Seebeck effect. SSE has been observed in many different types of materials, however, its mechanism has not yet been understood completely. Initially, it was observed in metallic magnets [25] and later it was observed in magnetic insulators [26], paramagnets [27] and even antiferromagnetics [28] and non-magnetic materials [29]. Here we focus on the SSE in magnetic insulators. Following the treatment of FMs in finite temperature given in the previous chapter, we implement a temperature gradient over such materials and try to simulate the SSE. After succeeding in the generation of spin current, we study the different aspects of such phenomena and try to understand the fundamental mechanism(s) particularly in magnetic insulators.

Geometrically, two types of SSE have been observed, transversal and longitudinal. In the transversal one, the temperature gradient and the spin current are perpendicular while in the longitudinal SSE they are parallel. In this chapter, we address both.

Needless to say, to have a current we need some carriers. The carriers for the spin current can be diverse. In the early stage of SSE observation in metallic magnets the spin current was thought to be carried just by the spin-polarized electrons. After observation of SSE in magnetic insulators, magnons (as the quantum of spin waves (SW)) were acknowledged as another potential spin current carrier. In such a case, the generated spin current is called *SW spin current*. The latter which is our focus in this thesis is much more interesting since opposed to a spin-polarized electron current, there is no energy loss due to electrical resistance.

3.1 Spin-Wave Spin Current inside a Ferromagnetic Sample

When it comes to the relation between the current and carriers, the first equation that comes to our mind is the equation of continuity. Here we follow the same analogy to find the SW spin current formula. At first glance the Gilbert equation (Eq. (2.26)) could be the best choice because the carriers of SW spin current (i.e. spin waves) can be derived from that [26, 30]. So we start from Gilbert equation :

$$\frac{\partial \vec{S}(\vec{r}, t)}{\partial t} + \gamma \vec{S}(\vec{r}, t) \times \vec{H}^{eff}(\vec{r}, t) + \frac{\alpha\gamma}{M_S} \vec{S}(\vec{r}, t) \times \frac{\partial \vec{S}(\vec{r}, t)}{\partial t} = 0. \quad (3.1)$$

in which the spin density $\vec{S}(\vec{r}, t) = -\frac{\vec{M}(\vec{r}, t)}{\gamma}$ is used instead of magnetic moment density (magnetization). As we are interested in SW spin current and since spin waves are collective excitations governed by the exchange interaction, we separate the contribution of the

exchange field to the total effective field and rewrite the Gilbert equation in the following form

$$\frac{\partial \vec{S}(\vec{r}, t)}{\partial t} + \gamma \vec{S}(\vec{r}, t) \times \left(\vec{H}^{eff} - \vec{H}^{exch} \right) + \frac{\alpha \gamma}{M_S} \vec{S}(\vec{r}, t) \times \frac{\partial \vec{S}(\vec{r}, t)}{\partial t} + \nabla \cdot \vec{J}^s(\vec{r}, t) = 0, \quad (3.2)$$

where \vec{H}^{exch} is the exchange field and the SW spin current density tensor $\vec{J}^s(\vec{r}, t)$ is defined as [26, 31, 32] :

$$\nabla \cdot \vec{J}^s(\vec{r}, t) = \gamma \vec{S}(\vec{r}, t) \times \vec{H}^{exch}(\vec{r}, t), \quad (3.3)$$

which is equivalent to

$$\nabla \cdot \vec{J}^s(\vec{r}, t) = -\vec{M}(\vec{r}, t) \times \vec{H}^{exch}(\vec{r}, t). \quad (3.4)$$

The divergence of SW spin current density tensor is defined as

$$\begin{aligned} \nabla \cdot \vec{J}^s(\vec{r}, t) &= \left[\frac{\partial}{\partial x}, \frac{\partial}{\partial y}, \frac{\partial}{\partial z} \right] \cdot \begin{bmatrix} J_x^{s^x}(\vec{r}, t) & J_x^{s^y}(\vec{r}, t) & J_x^{s^z}(\vec{r}, t) \\ J_y^{s^x}(\vec{r}, t) & J_y^{s^y}(\vec{r}, t) & J_y^{s^z}(\vec{r}, t) \\ J_z^{s^x}(\vec{r}, t) & J_z^{s^y}(\vec{r}, t) & J_z^{s^z}(\vec{r}, t) \end{bmatrix} \\ &= \hat{i} \vec{\nabla} \cdot \vec{J}^{s^x}(\vec{r}, t) + \hat{j} \vec{\nabla} \cdot \vec{J}^{s^y}(\vec{r}, t) + \hat{k} \vec{\nabla} \cdot \vec{J}^{s^z}(\vec{r}, t), \end{aligned}$$

where e.g. $J_y^{s^x}(\vec{r}, t)$ means the contribution of the x component of the magnetization vector in SW spin current density tensor flowing in the y direction at the point (\vec{r}, t) and so on. In micromagnetism, the contribution of the exchange interaction to free energy density is $F^{exch} = \int A \left(\nabla \vec{M} / M_S \right)^2 d^3r$ where A is the stiffness constant and $\left(\nabla \vec{M} / M_S \right)^2 = \left(\nabla M_x / M_S \right)^2 + \left(\nabla M_y / M_S \right)^2 + \left(\nabla M_z / M_S \right)^2$ [33, 34]. So the corresponding exchange field would be $\vec{H}^{exch}(\vec{r}, t) = -\frac{\partial F^{exch}(\vec{r}, t)}{\partial \vec{M}(\vec{r}, t)} = \frac{2A}{M_S^2} \nabla^2 \vec{M}(\vec{r}, t)$. By substituting the exchange field in Eq. (3.4) we obtain

$$\nabla \cdot \vec{J}^s(\vec{r}, t) = -\frac{2A}{M_S^2} \vec{M}(\vec{r}, t) \times \nabla^2 \vec{M}(\vec{r}, t). \quad (3.5)$$

By reverse calculations, it is not difficult to show [26, 32] :

$$J_i^{s^j}(\vec{r}, t) = -\frac{2A}{M_S^2} \left[\vec{M}(\vec{r}, t) \times \nabla_i \vec{M}(\vec{r}, t) \right]_j = -\frac{2A}{M_S^2} \varepsilon_{j\nu\beta} M^\nu \nabla_i M^\beta, \quad (3.6)$$

where $\varepsilon_{j\nu\beta}$ is the Levi-Civita antisymmetric tensor. Finally, for numerical purposes, we discretize the gradient :

$$\begin{aligned} J_x^{s^j}(n_x, n_y, n_z, t) &= -\frac{2A}{aM_S^2} \varepsilon_{j\nu\beta} M^\nu(n_x, n_y, n_z, t) \left[M^\beta(n_x + 1, n_y, n_z, t) - M^\beta(n_x, n_y, n_z, t) \right], \\ J_y^{s^j}(n_x, n_y, n_z, t) &= -\frac{2A}{aM_S^2} \varepsilon_{j\nu\beta} M^\nu(n_x, n_y, n_z, t) \left[M^\beta(n_x, n_y + 1, n_z, t) - M^\beta(n_x, n_y, n_z, t) \right], \\ J_z^{s^j}(n_x, n_y, n_z, t) &= -\frac{2A}{aM_S^2} \varepsilon_{j\nu\beta} M^\nu(n_x, n_y, n_z, t) \left[M^\beta(n_x, n_y, n_z + 1, t) - M^\beta(n_x, n_y, n_z, t) \right], \end{aligned} \quad (3.7)$$

where e.g. $J_x^{s^z}(n_x, n_y, n_z, t)$ is the contribution of z component of the magnetization vector in SW spin current density tensor flowing in the x direction at the point (n_x, n_y, n_z, t) and

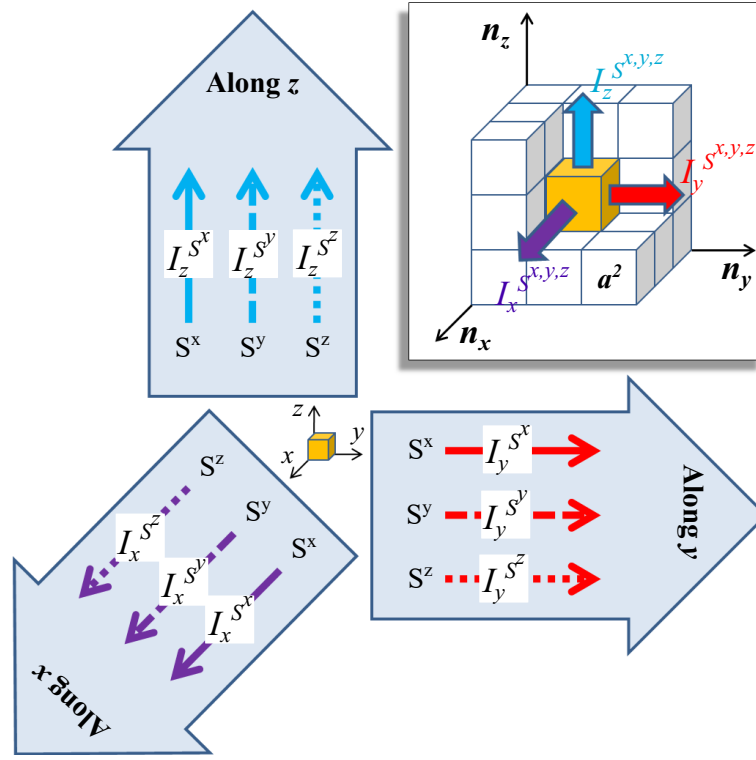


Figure 3.1: Schematic of the meaning of different components of the SW spin current tensor (Eqs. (3.8)).

so on. To get the SW spin current tensor which flows through each FM-cell faces the SW spin current density tensor is multiplied by a^2 :

$$\begin{aligned}
 I_x^{s^j}(n_x, n_y, n_z, t) &= -\frac{2Aa}{M_S^2} \varepsilon_{j\nu\beta} M^\nu(n_x, n_y, n_z, t) [M^\beta(n_x + 1, n_y, n_z, t) - M^\beta(n_x, n_y, n_z, t)] , \\
 I_y^{s^j}(n_x, n_y, n_z, t) &= -\frac{2Aa}{M_S^2} \varepsilon_{j\nu\beta} M^\nu(n_x, n_y, n_z, t) [M^\beta(n_x, n_y + 1, n_z, t) - M^\beta(n_x, n_y, n_z, t)] , \\
 I_z^{s^j}(n_x, n_y, n_z, t) &= -\frac{2Aa}{M_S^2} \varepsilon_{j\nu\beta} M^\nu(n_x, n_y, n_z, t) [M^\beta(n_x, n_y, n_z + 1, t) - M^\beta(n_x, n_y, n_z, t)] ,
 \end{aligned}
 \tag{3.8}$$

where $j = x, y, z$ stand for different components of magnetization. The first line includes 3 components of the tensor corresponding to the spin currents which all flow in the x direction and for 3 different components of magnetization vector. In the same way the second and third lines correspond to the components of spin current which all flow in the y and z direction respectively (see Fig. 3.1).

Eqs. 3.8 can be further simplified as

$$\begin{aligned}
 I_x^{sj}(n_x, n_y, n_z, t) &= -\frac{2Aa}{M_S^2} \varepsilon_{j\nu\beta} M^\nu(n_x, n_y, n_z, t) M^\beta(n_x + 1, n_y, n_z, t), \\
 I_y^{sj}(n_x, n_y, n_z, t) &= -\frac{2Aa}{M_S^2} \varepsilon_{j\nu\beta} M^\nu(n_x, n_y, n_z, t) M^\beta(n_x, n_y + 1, n_z, t), \\
 I_z^{sj}(n_x, n_y, n_z, t) &= -\frac{2Aa}{M_S^2} \varepsilon_{j\nu\beta} M^\nu(n_x, n_y, n_z, t) M^\beta(n_x, n_y, n_z + 1, t).
 \end{aligned} \tag{3.9}$$

Finally, we draw attention to the dimension of the spin current as being Joule as expected since it has the dimension of the spin divided by the dimension of time.

3.1.1 Longitudinal Spin Current in a Chain

In this chapter, we simulate the SW spin current in a chain of coupled FM domains along the x axis (Fig. 3.2). In such a case, just three components of the spin current tensor remain. At site n they are written as

$$\begin{aligned}
 I_n^{sx} &= -\frac{2Aa}{M_S^2} [M_n^y M_{n+1}^z - M_n^z M_{n+1}^y], \\
 I_n^{sy} &= -\frac{2Aa}{M_S^2} [M_n^z M_{n+1}^x - M_n^x M_{n+1}^z], \\
 I_n^{sz} &= -\frac{2Aa}{M_S^2} [M_n^x M_{n+1}^y - M_n^y M_{n+1}^x].
 \end{aligned} \tag{3.10}$$

By some straightforward calculations, it can be seen that this definition and the definition given in Ref. [30] are the same :

$$\begin{aligned}
 I_n^{s\alpha} &= -\frac{2Aa}{M_S^2} \sum_{m=1}^n M_m^\beta (M_{m-1}^\gamma + M_{m+1}^\gamma) \varepsilon_{\alpha\beta\gamma} \\
 &= -\frac{2Aa}{M_S^2} \sum_{m=1}^n [\vec{M}_m \times (\vec{M}_{m-1} + \vec{M}_{m+1})]^\alpha \\
 &= -\frac{2Aa}{M_S^2} [\vec{M}_n \times \vec{M}_{n+1}]^\alpha = -\frac{2Aa}{M_S^2} M_n^\beta M_{n+1}^\gamma \varepsilon_{\alpha\beta\gamma},
 \end{aligned} \tag{3.11}$$

where we assumed $I_0^{s\alpha} = 0$ and $\vec{M}_0 = 0$ as boundary conditions (see Ref. [30]). The benefit of writing the SW spin current in this form is that it exposes the SW spin current as

$$I_n^{s\alpha} = \frac{a^3}{\gamma} \sum_{m=1}^n \vec{Q}_m, \tag{3.12}$$

where $\vec{Q}_m = -\frac{2A\gamma}{a^2 M_S^2} \vec{M}_m \times (\vec{M}_{m-1} + \vec{M}_{m+1}) = -\gamma \vec{M}_m \times \vec{H}^{exch}$ is the exchange torque (the contribution of exchange interaction in micromagnetic free energy density in discrete form is $-\frac{2A}{a^2 M_S^2} \sum_n \vec{M}_n \cdot \vec{M}_{n+1}$). It states that the exchange torque can generate or absorb SW spin current at each site as shown in Fig. 3.2 schematically.

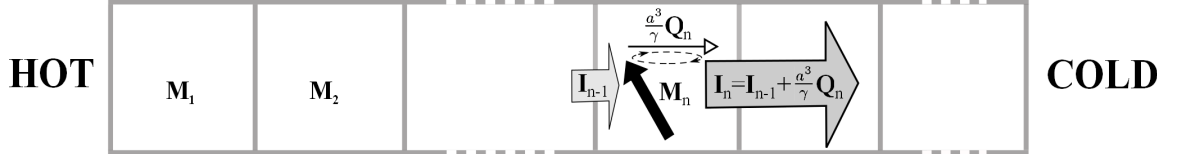


Figure 3.2: Schematic of SSE and the role of exchange torque (\vec{Q}_n) in the generation or absorption of SW spin current (\mathbf{I}_n).

An Alternative Way : Due to quantum nature of magnetic moments and spins we can use the Heisenberg equation of motion as well to derive the spin current formula. In reduced units the Heisenberg equation of motion reads as $\frac{\partial \sigma_n^\alpha}{\partial t} = i[\Lambda, \sigma_n^\alpha]$, where the Hamiltonian is assumed to have just the exchange term :

$$\Lambda = \sum_n J(\sigma_n^x \sigma_{n+1}^x + \sigma_n^y \sigma_{n+1}^y + \sigma_n^z \sigma_{n+1}^z), \quad (3.13)$$

where σ_n^α are Pauli matrices. After straightforward calculations, using spin commutator relation $[\sigma_n^\alpha, \sigma_m^\beta] = i\delta_{nm}\epsilon_{\alpha\beta\gamma}\sigma_n^\gamma$ and comparing Heisenberg equation of motion with the continuity equation $\frac{\partial \sigma_n^\alpha}{\partial t} + \{I_n^\alpha - I_{n-1}^\alpha\} = 0$ we reach the spin current formula as $I_n^\alpha = J\sigma_n^\beta \sigma_{n+1}^\gamma \epsilon_{\alpha\beta\gamma}$ which in real units ($J \rightarrow -2Aa$) is the same as the Eq. (3.11).

Model In this section we simulate the SW spin current for a FM chain with the following free energy density :

$$F = \frac{k}{M_S^2} \sum_n (M_S^2 - (M_n^z)^2) - \frac{2A}{a^2 M_S^2} \sum_n \vec{M}_n \cdot \vec{M}_{n+1}, \quad (3.14)$$

where k is the uniaxial anisotropy constant. The effective magnetic field acting on the n -th magnetic moment then reads

$$\vec{H}_n^{eff} = -\frac{\partial F}{\partial \vec{M}_n} + \vec{\xi}_n(t) = \frac{2k}{M_S^2} M_n^z \hat{z} + \frac{2A}{a^2 M_S^2} (\vec{M}_{n+1} + \vec{M}_{n-1}) + \vec{\xi}_n(t), \quad (3.15)$$

where the site-dependent noise reflects the existence of a nonuniform temperature profile. Here we implement a Gaussian white noise with the following properties :

$$\begin{aligned} \langle \xi_{ik}(t) \rangle &= 0, \\ \langle \xi_{ir}(t) \xi_{jl}(t + \Delta t) \rangle &= \frac{2k_B T_i \alpha}{\gamma M_S a^3} \delta_{ij} \delta_{rl} \delta(\Delta t), \end{aligned} \quad (3.16)$$

where i and j count the site numbers in the FM chain and r, l correspond to the Cartesian components of the random field and T_i is the site-dependent local temperature. We remind that T_i are the temperature of the environment (with all its microscopic degrees of freedom being replaced by the random magnetic field) not the temperature of FM system (magnon subsystem). In the case of FM insulators, this environment is phonon subsystem and T_i represent the local phonon temperatures. In what follows, we employ the parameters for the numerical calculations : $M_S = 1.71$ [MAm⁻¹], $A = 21$ [pJm⁻¹], $k = 48$ [kJm⁻³], and $\alpha = 0.01$ which are appropriate for Iron. Although Iron is a metallic FM and the contribution

of itinerant electrons in the spin current must be investigated as well, in our model we just study the contribution of magnetization dynamics in the spin current. Later we will see that for the contribution of magnetization dynamics to the spin current, the results are generic and valid for FM insulators (Sec. 3.3). We use Iron parameters to facilitate the numerical integrations in term of the execution time of our code. Cell size is chosen smaller than FM domain wall ($\sim \pi\sqrt{A/K} \approx 65$ [nm] [33]) to assure the magnetization within each cell is more or less uniform and moreover it will not change sharply from one cell to another cell. Here we put $a = 20$ [nm]. Finally, all the results shown here are averaged over different realization of the noises at the time that the system is relaxed unless other conditions clearly be mentioned. By *relax* here we mean that the quantities will not change anymore as the time goes on (stationary state).

Due to the exchange interaction, we need 6 constants to solve 3 components of LLG equation which in fact are the boundary conditions. Here we chose open boundary conditions, meaning that the first FM cell is assumed to interact just with the second one and the N -th FM cell is assumed to interact just with $(N-1)$ -th one.

SW Spin Current Profile In Fig. 3.3a statistically averaged components of SW spin current versus the site number is shown. As can be seen, the spin current is carried by the z component of magnetization and the contribution of two other components is roughly zero; we remind that the uniaxial anisotropy is along the z axis (Eq. (3.14)). Following the sign of exchange torque in Fig. 3.3b we understand its role in the generation (positive sign) or absorption (negative sign) of SW spin current (Eq. (3.12)). In Fig. 3.4 the dependency of the spin current profile on the temperature gradient is shown. As can be inferred it is the temperature gradient that drives the SW spin current. The zero value of the last side is the immediate consequence of open boundary conditions and our definition for the spin current (Eq. (3.11)).

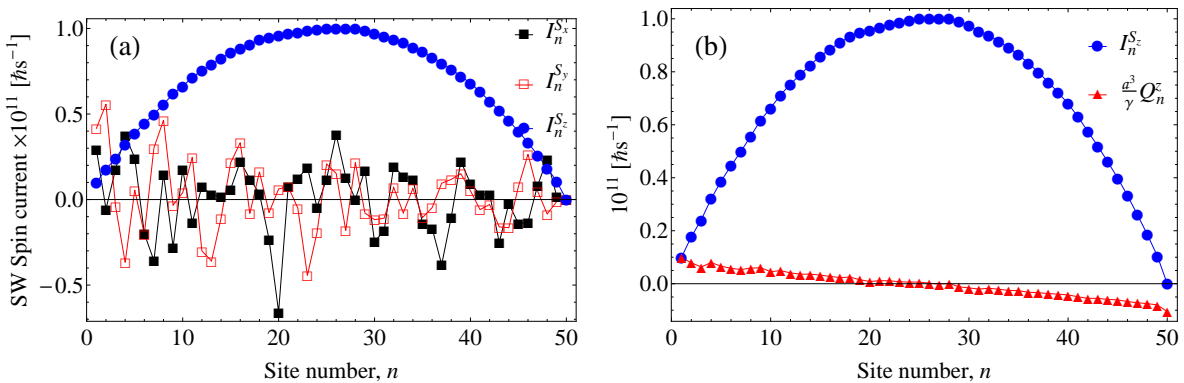


Figure 3.3: a) Statistically averaged SW spin current at the stationary state versus site number for a chain with $N = 50$ and a temperature gradient of $T_n = T_1 - \frac{\Delta T}{N}(n-1)$, where $T_1 = 10$ [K] and $\Delta T = 10$ [K]. b) The spin current profile is compared with the exchange torque profile (see also Fig. 3.2). The quantities are averaged over 1000 realizations of the noises.

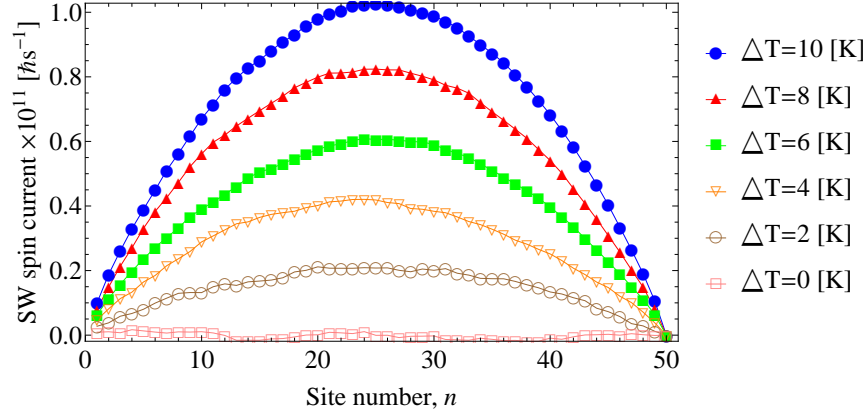


Figure 3.4: a) Statistically averaged SW spin current at stationary state versus site number for a chain with $N = 50$ and a temperature gradient of $T_n = T_1 - \frac{\Delta T}{N}(n - 1)$ for different value of ΔT are shown. $T_1 = 10$ [K] and the SW spin currents are averaged over 1000 realizations of the noises.

To consolidate our claim that the generation and absorption of SW spin current are due to exchange torque, the magnon accumulation profile is shown in Fig. 3.5b. Considering this figure along with the exchange torque profile (Fig. 3.3b) we can say that in the hot part of the chain (left) the exchange torque generates magnons (as SW spin current carriers) and so SW spin current increases and as we approach the cold part (right) the exchange torque starts to absorb magnons and so the SW spin current decreases.

To calculate magnon accumulation, following the procedure given in Ref. [35] we define two quantities : equilibrium magnetization $\overline{\langle m^z \rangle_e^{T_n}}$ and nonequilibrium steady-state magnetization $\langle m_n^z \rangle$, where $m_n^z = M_n^z / M_S$ is the reduced magnetization. First, we remind that generally speaking when there is a time-independent current in a system, the system is called to be in nonequilibrium steady-state; *nonequilibrium* because there are carriers that move along the system and carry current and *steady-state* because this current is time-independent. Steady state could happen when we let the system evolve enough in time and

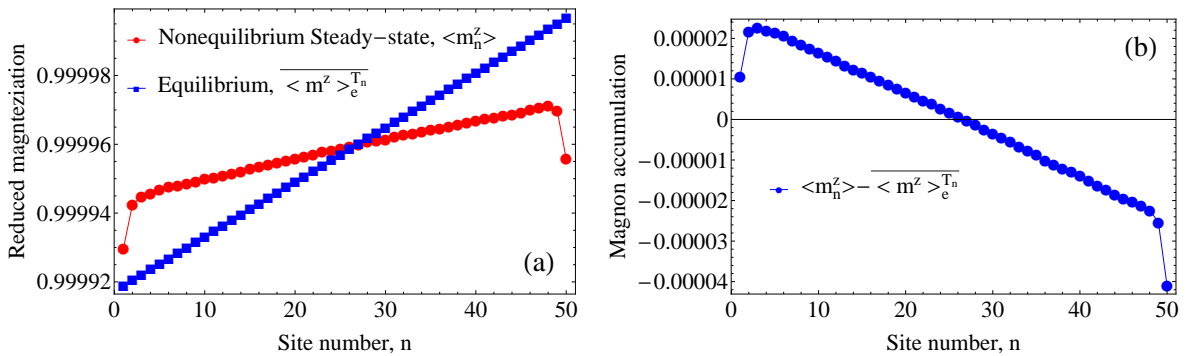


Figure 3.5: a) Corresponding equilibrium magnetization $\overline{\langle m^z \rangle_e^{T_n}}$ and nonequilibrium steady-state magnetization $\langle m_n^z \rangle$ profiles to Fig. 3.3 are shown. b) The corresponding magnon accumulation versus site number is shown.

relaxes, like what we do here. Magnetization in such conditions is called nonequilibrium steady-state magnetization. On the other hand, the equilibrium magnetization is the magnetization of the system when there is no temperature gradient and so no current along the chain. It means that we keep the temperature along the chain uniform and then let the system be relaxed and then calculate the averaged magnetization. Of course, depending on the value of this uniform temperature (T) the equilibrium magnetization could have different values $\overline{\langle m^z \rangle_e^T} = \sum_{n'=1}^N \langle m_{n'}^z \rangle_e^T / N$. Magnon accumulation is the difference between these two types of magnetization $\langle m_n^z \rangle - \overline{\langle m^z \rangle_e^T}$. To calculate corresponding $\overline{\langle m^z \rangle_e^{T_n}}$ to each $\langle m_n^z \rangle$, we take a chain with a uniform temperature equal to the corresponding temperature at site n when there is a temperature gradient along the chain (T_n). The results are shown in Fig. 3.5.

To inspect finite-size effects, we simulated the spin current for different lengths of the chain. As can be seen in Fig. 3.6 for enough long chains as we are far from the boundaries, the exchange torque is zero and so no magnon is supposed to be generated or absorbed within this range and magnons just move from hot to the cold side with a constant SW spin current. Moreover, it says that the formed uniform spin current far from the boundaries for long enough chains depends on the $\Delta T/N$, not the absolute value of temperatures.

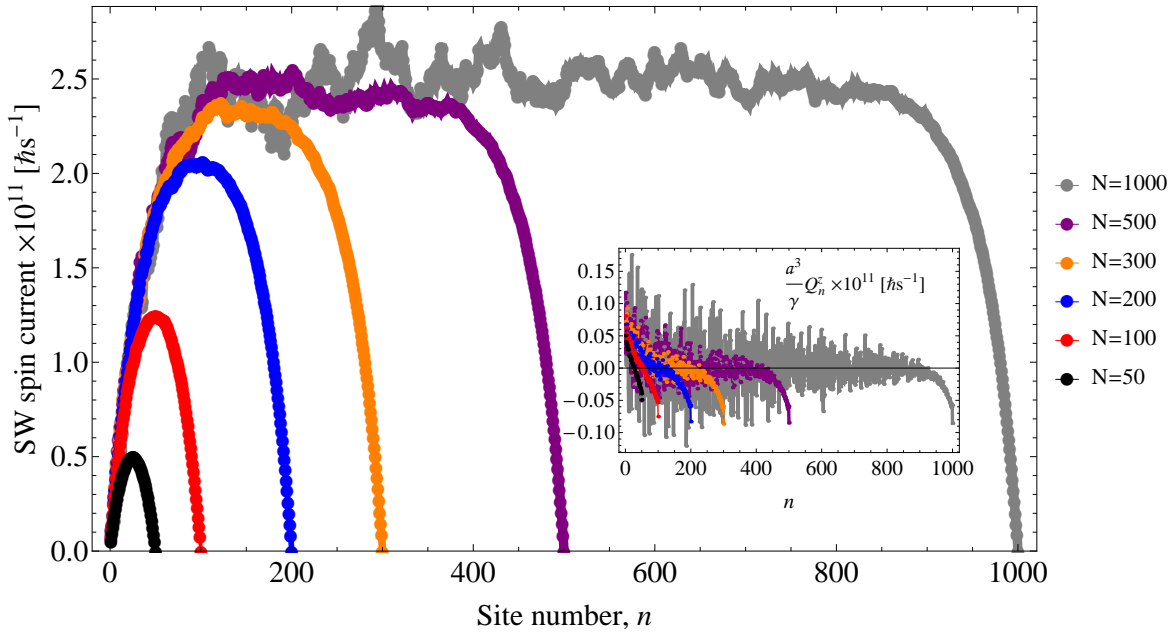


Figure 3.6: SW spin current versus site number for chains with different lengths with a temperature gradient of $T_n = T_1 - \frac{\Delta T}{N}(n - 1)$ are shown, where $T_1 = 0.1 \times N$ [K] and $\Delta T = 0.1 \times N$ [K]. As can be seen, when the size of the chains is large enough ($N > 300$) so that size effects are dismissible, same spin current is formed in the middle of the chains independent of the length of the chains ($\sim 2.5 \times 10^{11}$ [$\hbar s^{-1}$]). The inset shows the corresponding exchange torques. All quantities are averaged over 1000 realizations of the noises.

3.2 Spin Current at the Interface

Experimentally the spin current is detected as the electric voltage. The FM is attached to a normal metal (NM) so that the pumped spin current is converted to an electric current due to inverse spin-Hall effect (ISHE) [36–39] (since the spin-orbit coupling is the mechanism behind ISHE, a heavy NM such as Pt is appropriate for this propose). However, the sole attachment of the NM potentially can affect the generated SW spin current in the FM. Here we address this issue by considering two cases : (a) when the SW spin current approaches the interface (boundary of FM chain) longitudinally (Sec. 3.2.1), and (b) when the transverse spin current pumped out of FM chain transversely (perpendicular to the chain) (Sec. 3.2.2). See Fig. 3.7 for clarification.

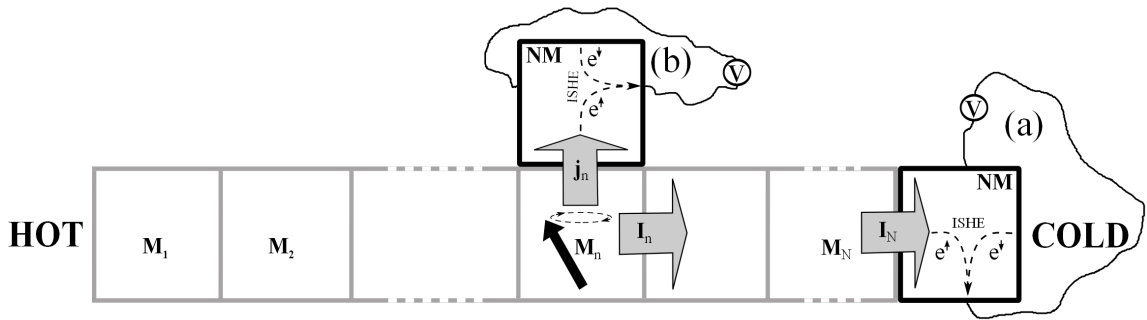


Figure 3.7: Schematic of detection of a) longitudinal SSE and b) transversal SSE.

3.2.1 Longitudinal Spin Current near the Interface

A NM attached to the boundary of a FM chain (Fig. 3.7a) affects the SW spin current in two ways : I. Enhancement of Gilbert damping at the interface and II. Adding an extra torque known as the spin–transfer torque which acts on the magnetization at the interface.

I. Enhanced Gilbert Damping : NM attached to the spin current source (here FM) can play the role of a sink for spin current. This can be seen as an extra dissipation of magnetization at the interface which is translated as the enhancement of Gilbert damping ($\Delta\alpha$) and mathematically is shown as [40] :

$$\frac{\partial \vec{M}}{\partial t} = -\gamma \vec{M} \times \vec{H}^{eff} + \frac{\alpha + \Delta\alpha}{M_S} \vec{M} \times \frac{\partial \vec{M}}{\partial t}, \quad \Delta\alpha = \frac{\gamma \hbar}{4\pi M_s} g_{eff} \delta(x - L), \quad (3.17)$$

where L is the position of interface, and g_{eff} is the real part of the *effective* spin-mixing conductance. The underlying mechanism for this phenomena is a nonlocal interaction between the angular momentum in FM and the spin of the itinerant electrons in NM which in turn causes angular momentum to be pumped into the itinerant electrons and finally magnetization losses and damping enhancement [41, 42].

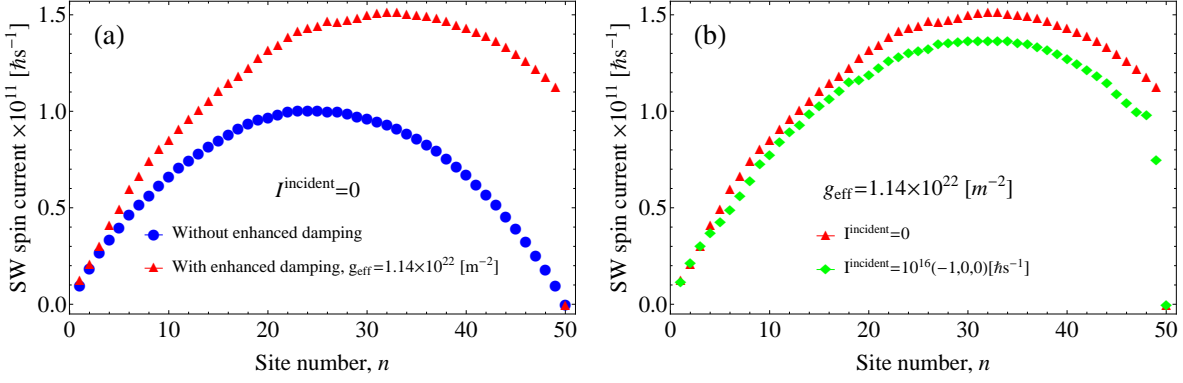


Figure 3.8: Statistically averaged SW spin current at stationary state versus site number for a chain with $N = 50$ and a linear temperature gradient with $T_1 = 10$ [K] and $T_N = 0$ [K]. a) Enhanced Gilbert damping effect b) Enhanced Gilbert damping and spin-transfer torque effects. The quantities are averaged over 1000 realization of the noises.

II. Spin-Transfer Torque : The enhanced damping is one side of the coin when it comes to the interface effects. In reality, spin-flip relaxation time in NM is not fast enough and it takes time for the spins to leave the interface and reach equilibrium within the NM. In such a case, we have a spin accumulation at the interface in NM and a flowback of spin current from NM to FM is inevitable [31, 40]. Such an incident spin current ($\vec{I}^{incident}$) can be formulated as a torque acting on the magnetization [41, 43, 44] :

$$\vec{\tau}^s = -\frac{\gamma}{M_S^2 V} \vec{M} \times \left(\vec{M} \times \vec{I}^{incident} \right), \quad (3.18)$$

known as Slonczewski's torque and it describes the dynamics of a monodomain ferromagnet of volume V subjected to the spin current $\vec{I}^{incident}$ and modifies the right-hand side of the LLG equation as a source term. In general, a correction torque to Slonczewski's torque is also allowed [41, 45]

$$\vec{\tau}^{s'} = -\frac{\gamma}{M_S V} \beta \vec{M} \times \vec{I}^{incident}, \quad (3.19)$$

where β gives the relative strength with respect to the Slonczewski's torque (Eq. (3.18)). In order to simulate the enhanced Gilbert damping and spin-transfer torque we assume that they act just on the last site. So the dynamics of our FM chain is described by the following LLG equations :

$$\frac{\partial \vec{M}_n}{\partial t} = -\frac{\gamma}{1 + \alpha^2} \vec{M}_n \times \vec{H}_n^{eff} - \frac{\gamma \alpha}{(1 + \alpha^2) M_S} \vec{M}_n \times (\vec{M}_n \times \vec{H}_n^{eff}) \quad ; n = 1, \dots, (N - 1), \quad (3.20)$$

and

$$\begin{aligned} \frac{\partial \vec{M}_N}{\partial t} = & -\frac{\gamma}{1 + \alpha_N^2} \vec{M}_N \times \vec{H}_N^{eff} - \frac{\gamma \alpha_N}{(1 + \alpha_N^2) M_S} \vec{M}_N \times (\vec{M}_N \times \vec{H}_N^{eff}) \\ & - \frac{\gamma}{M_S^2 a^3} \vec{M}_N \times \left(\vec{M}_N \times \vec{I}^{incident} \right) - \frac{\gamma}{M_S a^3} \beta \vec{M}_N \times \vec{I}^{incident}, \end{aligned} \quad (3.21)$$

where $\alpha_N = \alpha + \frac{\gamma\hbar}{4\pi a M_s} g_{eff}$. The results are shown in Fig. 3.8. As can be seen in Fig. 3.8a the enhanced damping facilitates draining the spin current in NM and causes the enhancement of the spin current at the interface. On the other hand, the inclusion of the effect of the flowback of spin currents (Fig. 3.8b) causes the spin current to decrease at the interface.

3.2.2 Transversal Spin Current

Besides the generated longitudinal SW spin current along the temperature gradient, a transversal spin current perpendicular to the temperature gradient can also be detected thanks to a NM attached on the top of the chain as shown in Fig. 3.7b. Similar to the previous case, this transversal current stems from the interplay between the angular momentums in FM and the spin of itinerant electrons in NM. In other words, the fluctuation of magnetization in FM determines the pumped spin current from the FM to the NM and the spin fluctuation of the itinerant electrons in NM determines the backflow of the spin current from NM to the FM. We follow the procedure given in Ref. [32] to calculate these currents. The first is given by $\frac{a^3}{M_S\gamma} \langle \vec{M}_n \times \partial_t \vec{M}_n \rangle^z$ when there is a temperature gradient along the chain and the second is given by $\frac{a^3}{M_S\gamma} \langle \vec{M} \times \partial_t \vec{M} \rangle^{T_n} = \frac{a^3}{M_S\gamma} \sum_{n'=1}^N \langle \vec{M}_{n'} \times \partial_t \vec{M}_{n'} \rangle^{T_n} / N$ at a uniform temperature equal to the corresponding temperature at site n when there is a temperature gradient along the chain (similar to the procedure followed to calculate equilibrium magnetization and magnon accumulation). The total spin current pumped to the NM is $\frac{a^3}{M_S\gamma} \left(\langle \vec{M}_n \times \partial_t \vec{M}_n \rangle^z - \langle \vec{M} \times \partial_t \vec{M} \rangle^{T_n} \right)$. The results are shown in Fig. 3.9.

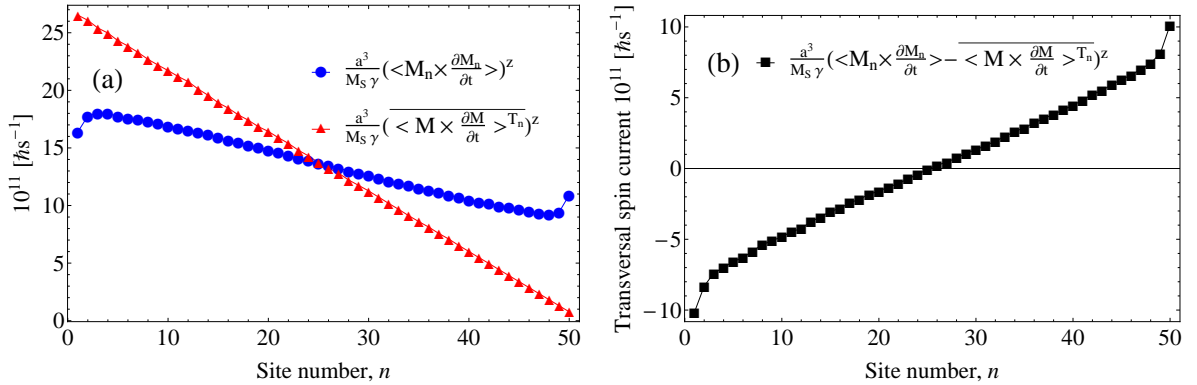


Figure 3.9: a) The contributors to the transversal spin current. b) Statistically averaged net transversal spin current injected to the NM (see Fig. 3.7b) at the stationary state versus site number for a chain with $N = 50$ and a temperature gradient of $T_n = T_1 - \frac{\Delta T}{N}(n - 1)$, where $T_1 = 10$ [K] and $\Delta T = 10$ [K]. The quantities are averaged over 1000 realization of the noises.

Unlike longitudinal SW spin current which is attributed to the magnon accumulation, transversal spin current is attributed to the difference between phonon and magnon temperatures. Phonon temperature is in fact approximated as the temperatures of spin current carriers in NM (i.e. electrons) and is equal to the temperature we put into LLG equation via the noise $T = T^p \approx T^e$ (due to a fast electron-phonon relaxation). The magnon

temperature reflects the density of magnons generated due to thermal activation of magnetization. To calculate that, we follow the procedure given in Ref. [35]. It is based on the fact that when there is a uniform temperature along the chain, *at equilibrium* the magnon temperature is equal to the phonon temperature and equilibrium magnetization is equal to the steady-state magnetization $\overline{\langle m^z \rangle_e^T} = \langle m^z \rangle$ (see Sec. 3.1.1). We calculate the equilibrium magnetization for different values of uniform phonon temperatures (which is equal to the magnon temperature) and by fitting we find the relation between magnetization and magnon temperature $\langle m^z \rangle = f(T^m)$. Later, when there is a temperature gradient along the chain, we calculate nonequilibrium steady-state magnetization at each site $\langle m_n^z \rangle$ and using the derived relation (f), we obtain the magnon temperature at each site $T_n^m = f^{-1}(\langle m_n^z \rangle)$. The results are shown in Fig. 3.10. Comparing Fig. 3.9b and 3.10b we can claim that the difference between magnon and phonon temperatures is the mechanism behind the formed transversal spin current.

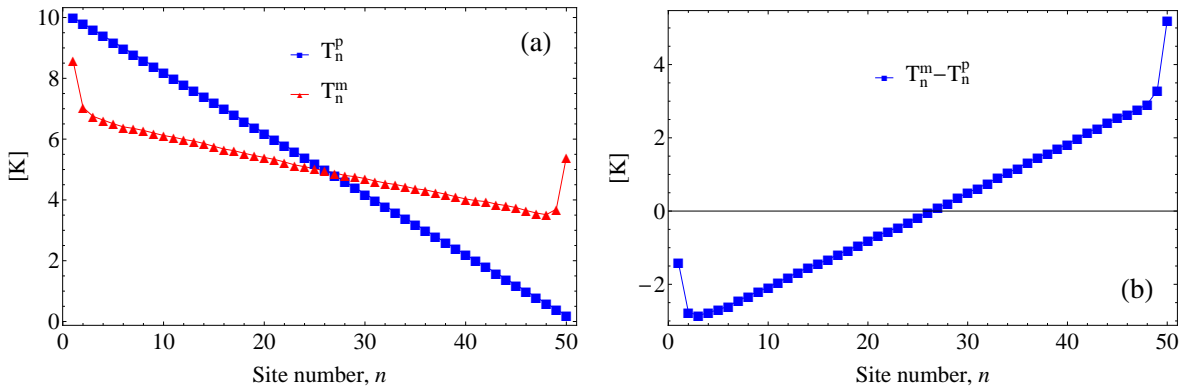


Figure 3.10: Corresponding phonon and magnon temperatures to Fig. 3.9 and their differences. When the magnon temperature is bigger than the phonon temperature (which is approximated as the electron temperature in NM due to a fast phonon-electron relaxation) as expected the net transversal spin current injected into the NM is positive and vice versa (Fig. 3.9b).

3.3 Yttrium Iron Garnet

We have simulated the spin current which is carried by spin waves (or their quantum, magnons). This type of spin current could be a dominant source of spin current when there is no itinerant electron in the systems. One material that has this property and experimentally has been used widely in SSE experiments is Yttrium iron garnet (YIG) with a chemical composition of $\text{Y}_3\text{Fe}_5\text{O}_{12}$. It has a complex unit cell with a cubic crystal structure. Three of Fe^{3+} ions are on tetrahedral sites and two others on octahedral sites. Y^{3+} has no magnetic moment, but the moments of Fe^{3+} ions on the tetrahedral sites are antiparallel to those on the octahedral sites so that there is a net magnet moment. Because of this incomplete spin compensation, YIG is classified as a ferrimagnet with a spontaneous magnetization of $4\pi M_S = 1.4 \times 10^5 [\text{A}\cdot\text{m}^{-1}]$ [46]. Numerically, however, it has been simulated

as a FM successfully [26, 31, 46, 47] with the free energy

$$F = -H_0 \sum_{n=1}^N M_n^z - \frac{2A}{a^2 M_S^2} \sum_{n=1}^N \vec{M}_n \cdot \vec{M}_{n+1}. \quad (3.22)$$

H_0 is an external magnetic field. The results for a chain under a temperature gradient are shown in Fig. 3.14. As can be seen, as before the SW spin current has a concave shape.

3.4 Spectral Characteristics of Spin-Wave Spin Current

So far we talked about the SW spin current generally as the spin current that is carried by magnons. However the magnons, themselves, can be classified based on their wave vectors. In this section we want to find which of these magnons have the main contribution to the generated SW spin current. The key to distinguishing the contribution of different magnons in the SW spin current is that they have different relaxation times $\tau_{pm}^q = (\alpha\omega_q)^{-1}$, depending on their wave vector q , which can be inferred from the solution of LLG equation [26] :

$$M_x(\vec{r}, t) + iM_y(\vec{r}, t) \propto \exp(i\vec{q} \cdot \vec{r} + i\omega_q t) \exp(-\alpha\omega_q t). \quad (3.23)$$

In the insulators the phonon-magnon scattering could be the main mechanism for this relaxation. The frequency spectrum of magnons is given by the dispersion relation which for the energy density given in Eq. (3.22) reads [33] :

$$\omega_q = \gamma \left(H_0 + \frac{4A}{a^2 M_S} (1 - \cos(qa)) \right), \quad (3.24)$$

which results in a phonon-magnon relaxation time as

$$\tau_{pm}^q = \left[\alpha\gamma \left(H_0 + \frac{4A}{a^2 M_S} (1 - \cos(qa)) \right) \right]^{-1}, \quad q = 2n\pi/d, n = 0, \pm 1, \dots \quad (3.25)$$

where $d = Na$ is the length of the chain. Using YIG parameters ($A = 4.6 \times 10^{-12}$ [Jm⁻¹] and $\gamma = 1.76 \times 10^{11}$ [T⁻¹s⁻¹] [46]) the phonon-magnon relaxation times and the corresponding frequencies are shown in Tab. 3.1. For the sake of accelerating the convergence of numerical routines, we put Gilbert damping rather large $\alpha = 0.1$. Of course, this scaling of Gilbert damping ($\alpha^{real} \sim 10^{-4}$) will scale the relaxation times (Eq. (3.25)), however after back rescaling we obtain the phonon-magnon relaxation times that exactly match with the experimentally measured ones (e.g. for uniform magnons $\tau_{mp}^{q=0} \approx 1$ [μ s] [47]).

Before proceeding further, let us look at the spectrum of all active spin waves. In Fig. 3.11 the simulated dispersion relation is shown. Comparing the results with the theoretical formula for the dispersion relation (Eq. 3.24) we will find the active spectrum of spin waves in our system. The next task is to find which part of this spectrum plays the main role in the SSE.

Table 3.1: Phonon-magnon relaxation times (τ_{pm}^q) and the corresponding frequencies ($\Omega_{mp}^q = 2\pi/\tau_{pm}^q$) according to Eq. (3.25) for $N = 50$, $a = 10$ [nm], $H_0 = 0.057$ [T] and $\alpha = 0.1$.

n	0	1	2	3	4	5
$ q_n = 2\pi n/Na$ [$10^8 m^{-1}$]	0.00	0.13	0.25	0.38	0.50	0.63
$\tau_{mp}^{q_n}$ [ns]	1.000	0.304	0.099	0.047	0.027	0.018
$\Omega_{mp}^{q_n}/2\pi$ [GHz]	1.0	3.3	10.1	21.4	36.9	56.5

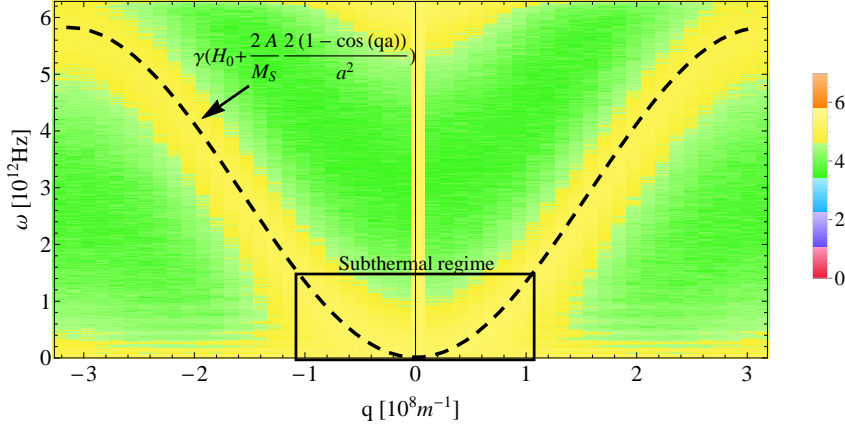


Figure 3.11: Spin-wave dispersion : The colormap in the background shows the absolute value of the discrete Fourier transformation of $m_x + im_y$ based on our simulations for a chain of 50 FM cells under a linear temperature gradient [48]. $T_1 = 0$, $T_N = 10$ [K], $a = 10$ [nm], $H_0 = 0.057$ [T] and the other parameters belong to YIG. The dashed black curve represents the theoretical dispersion relation formula (Eq. (3.24)). The black frame shows the subthermal regime of the spectrum.

3.4.1 Time-Resolved Study

To find which part of magnon spectrum (Fig. 3.11) has the main contribution to the SW spin current we do a time-resolve study as performed in experiment [50]. Experimentally, first we need to implement different time-dependent temperature gradients with different modulation frequencies (ω_{mod}) on the chain. We do this by solving the heat equation for the corresponding chain to our FM system with a periodic boundary condition (T_0) with a modulation frequency of ω_{mod} as shown in Fig. 3.12 [49]. After solving the heat equation and getting the temperature profile as a function of time and space we put it into LLG equation (in the noise term) to get magnetization dynamics. In this process, the feedback of magnon subsystem to phonon subsystem has been dismissed. However, implementing colored noise it can be seen that the results are generic [49]. For clarification of the mentioned recipe see Fig. 3.12 and Ref. [49].

The next step is to use a low-pass filter to filter the SW spin current. The low-pass filter puts a cutoff frequency (ω_c) on the SW spin current so that the contribution of spin waves with frequencies higher than ω_c is cut. We should note that this cutoff frequency is an extrinsic cutoff that experimentally can be tuned by external parameters such as capacitance

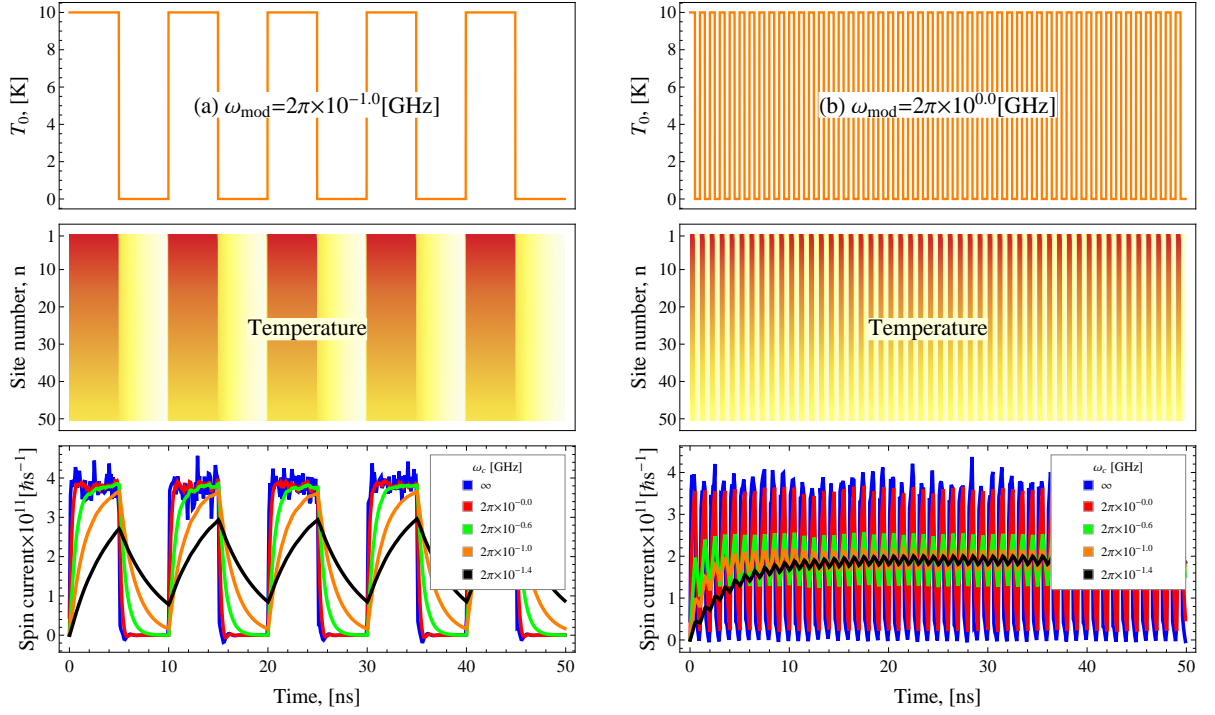


Figure 3.12: The time-resolved study of SSE for two different modulation frequencies. T_0 shows the boundary condition used to solve the heat equation. The figures in the second row show the colormap of phonon temperatures obtained from solving of the heat equation; the red color shows the maximum temperature (10 [K]) and the white color shows the minimum temperature (0 [K]). In the figures in the left and right columns the system is heated up periodically with the modulation frequencies of $\omega_{mod} = 2\pi \times 10^{-1.0}$ [GHz] and $\omega_{mod} = 2\pi \times 10^{0.0}$ [GHz], respectively. Putting the obtained temperature profiles into LLG equation the magnetization dynamics and SW spin current are evaluated (statistically averaged over 1000 realization of the noises). Here the spin current in the middle of the chain is shown. Different colors show the spin current after passing low-pass filter with different extrinsic cutoff frequencies (ω_c). For the blue curve no cutoff frequency is implemented on the spin current ($\omega_c = \infty$) but for the red, green, orange and black curves the cutoff frequencies are $\omega_c = 2\pi \times 10^{0.0}$ [GHz], $\omega_c = 2\pi \times 10^{-0.6}$ [GHz], $\omega_c = 2\pi \times 10^{-1.0}$ [GHz] and $\omega_c = 2\pi \times 10^{-1.4}$ [GHz], respectively. We choose $a = 10$ [nm], $H_0 = 0.057$ [T], $T_{00} = 10$ [K] and $\alpha = 0.1$. Other parameters belong to YIG. [49]

or resistance of low-pass filter circuit and numerically is just an input parameter. The effect of low-pass filter is characterized by a cascade in the amplitude of SW spin current at the modulation frequency equal to the cutoff frequency of the filter. However, the important observation is that as we increase this extrinsic cutoff frequency, at one stage the cascade will not follow that anymore and it happens earlier (see Fig. 3.13). It is the sign of an *intrinsic* cutoff frequency. Comparing these cascades which happen earlier than extrinsic ones (and happens step by step) with the phonon-magnon frequencies ($\Omega_{mp}^q = 2\pi/\tau_{pm}^q$) in Tab. 3.1, we find that they exactly match with the subthermal regime of magnon spectrum,

meaning these magnons play the main role in SW spin current in the SSE (see Fig. 3.11).

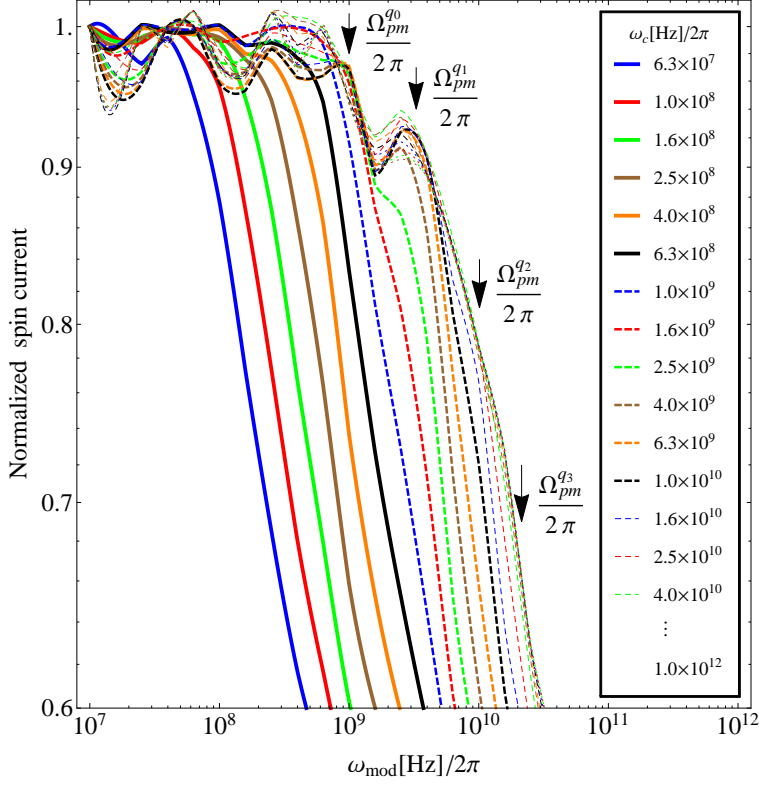


Figure 3.13: Normalized spin current ($\frac{I_{\omega_{mod}}}{I_{2\pi \times 10^7}}$) at the middle of a chain of 50 FM cells versus the modulation frequency for different extrinsic cutoff frequencies (ω_c) with the parameters $a = 10$ [nm], $H_0 = 0.057$ [T], $T_{00} = 10$ [K], $\alpha = 0.1$. Other parameters belong to YIG. The spin current is statistically averaged over 1000 noise realizations. For $\omega_c < 2\pi \times 10^9$ [Hz] the cascades follow the extrinsic cutoff frequencies which are characteristic of low-pass filter. However, for $\omega_c > 2\pi \times 10^9$ [Hz] the cascades occur earlier than the corresponding extrinsic cutoff which is a sign of intrinsic cutoff in the system. The arrows show the phonon-magnon frequencies ($\Omega_{pm}^{q_n}/2\pi$ in Tab. 3.1) for different wave vectors evaluated theoretically which coincide with the appearance of intrinsic cutoff frequencies (cascades) in the curves. Since the Gilbert damping chosen much larger than the real value, all the frequencies must be rescaled back to achieve the real ones correspond to the real value of Gilbert damping. For example, for $\alpha = 0.1$ the first cascade which corresponds to the uniform precession mode appears at [GHz]. It means that the corresponding real (experimental) cutoff frequency for the uniform precession mode must appear at [MHz] and so on for higher modes. [49]

3.5 White Noise vs Colored Noise

The basis of the stochastic LLG equation with a white noise is the separation of time scales, assuming that the heat bath (phonon subsystem) acts much faster than the magnon subsystem. In this case, the bath degrees of freedom can be averaged out and replaced by a stochastic field with a white noise correlation function. However, in case that our magnon subsystem changes as fast as the phonon subsystem (environment), like ultrafast magnetization dynamics, the correlation between the sequence of the noise fields is not dismissible and the back-reaction of magnon subsystem on the phonon subsystem must be included. In other words, the system is not memoryless (Markovian) anymore and a finite correlation time between phonon and magnon subsystems exists. In such a case, using white noise is not appropriate and colored noise should be used [11] and technically the Fokker-Planck equation will not be the same as we derived earlier in Sec. 2.1.1 and the dynamics of magnetization is given by a set of new equations. The generalized formulation of this approach for a multispin system has been given in Ref. [51] :

$$\begin{aligned}
 \frac{d}{dt} \vec{M}_i &= -\frac{\gamma}{1+\alpha^2} \vec{M}_i \times \left[\vec{H}_i^{eff} + \vec{\eta}_i \right], \\
 \frac{d}{dt} \vec{\eta}_i &= -\frac{1}{\tau_c} \left[\vec{\eta}_i - \frac{\alpha}{\gamma \tau_c M_S} \vec{M}_i \right] + \vec{R}_i, \\
 \langle R_{nr}(t) R_{ml}(t + \Delta t) \rangle &= \frac{2\alpha K_B T_n(t)}{\gamma \tau_c^2 M_S a^3} \delta_{nm} \delta_{rl} \delta(\Delta t), \\
 \langle R_{nr}(t) \rangle &= 0,
 \end{aligned} \tag{3.26}$$

where $\langle \dots \rangle$ represents the average over different realization of the noises, n and m are numbering magnetization vectors and r and l represent the Cartesian components of it. τ_c is the correlation time, α is the Gilbert damping and the coupling of magnon subsystem to heat bath is described by $\alpha/\gamma\tau_c$ so that in the limit $\tau_c \rightarrow 0$ the white noise approximation is recovered. In Fig. 3.14 the results for the spin current in a FM chain under a temperature

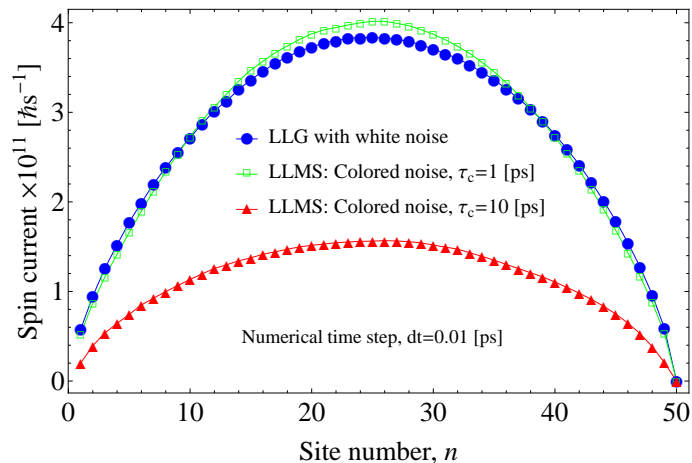


Figure 3.14: Statistically averaged spin currents as a function of the site number for a chain including 50 FM cells with white noise and colored noise for different values of correlation time are shown. The temperature gradient is linear with $\Delta T = 10$ [K]. All the parameters are the same as in the previous section.

gradient are shown. As expected for small correlation times colored noise approach and white noise approximation give more or less the same results. The mentioned approach which goes beyond the white noise approximation and takes into account the back reaction of the magnon subsystem to the surroundings phonon subsystem is known as Landau-Lifshitz-Miyasaki-Seki (LLMS) approach [51, 52].

3.6 Domain-Wall Motion

Finally, we address another important aspect of SSE which is spin-current driven Domain-wall (DW) motion. We enforce a Bloch DW in the system by anti-parallel boundary conditions, meaning that we fix $\vec{M}_0 = -M_S \hat{z}$ and $\vec{M}_{N+1} = +M_S \hat{z}$. When there is no temperature gradient, it is expected that the DW appears in the middle of the chain due to the symmetry of our system. In Fig. 3.15 a periodic temperature gradient as the previous section is implemented on the system. As can be seen, as long as there is a temperature gradient the DW tends to approach the hot part and as the gradient is removed the DW

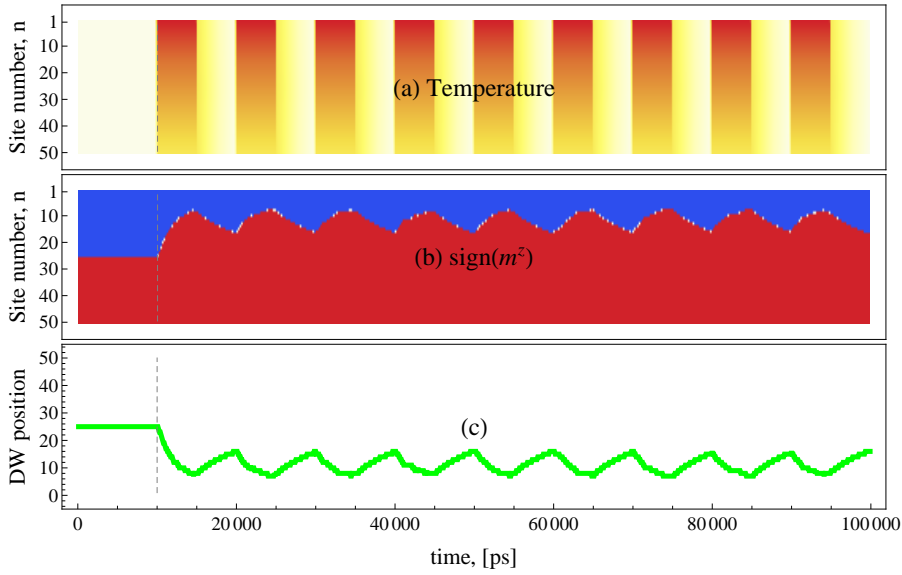


Figure 3.15: a) Shows the colormap of phonon temperature obtained from solving the heat equation [49]; the red color shows the maximum temperature ($T^{max} = 50$ [K]) and the white color shows the minimum temperature (0 [K]). b) shows the colormap of reduced magnetization. Blue region shows the sites with negative m^z sign and red region shows the sites with positive m^z sign. c) shows the sites in which the sign of m^z changes. When there is no temperature gradient the DW stays in the middle of the chain. For $t = [0 - 10000]$ [ps] no temperature gradient is implemented to be sure that the system has been stabilized. For $t > 10000$ [ps] a temperature pulse with a frequency of $\omega = 2\pi \times 10^{-4}$ [THz] is implemented on the first site of the chain. Here $N = 50$ and the amplitude of the temperature pulse is $T^{max} = 50$ [K].

approaches the middle of the chain as expected. In principle the DW can move either in the same direction or in the opposite direction of SW spin current [53]. When magnons pass through the DW, the induction of a reaction torque pushes the DW in the opposite direction of magnon current (SW spin current) [17, 54]. The DW cannot reach the end of the chain completely because of the antiparallel boundary conditions. However as can be seen in Fig. 3.16a higher absolute values for temperature helps further approaching the edge. Moreover, higher absolute values for temperature gradient results in a faster DW motion.

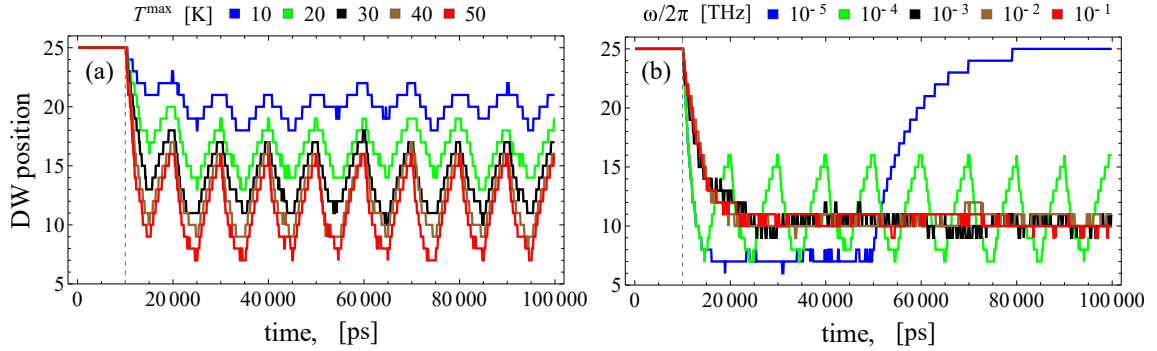


Figure 3.16: a) DW motion for different value of T^{max} for a chain with $N = 50$. b) DW motion for $T^{max} = 50$ [k] and different frequencies of temperature pulses for chain with $N = 50$. As can be seen for a small frequency of $\omega = 2\pi \times 10^{-5}$ [THz] DW comes back to the middle of the chain in the second half of the pulse ($t > 50000$ [ps]) as expected. Looking at the interval [10000 – 15000] [ps] we find that increasing the frequency will not increase the speed of DW motion and it saturates at a smaller value.

We did the same simulations for different frequencies to see if we can increase the speed of DW motion or not. As can be seen in Fig. 3.16b increasing the frequency is not favorable.

In these simulations, again for the sake of accelerating the convergence of numerical routines we used the Iron parameters with saturation magnetization $M_S = 1.71 \times 10^6$ [A.m⁻¹], stiffness constant $A = 2.1 \times 10^{-11}$ [Jm⁻¹], anisotropy constant $k = 4.8 \times 10^4$ [Jm⁻³], Gilbert damping $\alpha = 0.01$, gyromagnetic ratio $\gamma = 1.76 \times 10^{11}$ [T⁻¹s⁻¹], mass density $\rho = 7874.0$ [kgm⁻³], heat capacity $\kappa = 447.668$ [Wm⁻¹K⁻¹] and heat conductivity $C = 80.4$ [Jkg⁻¹K⁻¹]. Uniaxial anisotropy is along z and $a = 1$ [nm].

4 Temperature in Ferroelectrics

In line with our goal to study the thermal effects in ferroics, now we turn our attention to ferroelectrics (FEs). FEs are the electrostatic analog to the FMs with some common features like coercivity, though there are differences as well. They are characterized by a spontaneous polarization (net dipole moment per unit volume) due to the breaking of centrosymmetry of their crystallographic unit cell. This order parameter can be reversed through the application of an external electric field which is greater than a coercive field. FEs have been under investigation since their discoveries in early twenty century and they have been used in cooling technology, field effect transistors, data storage applications etc. [55–58]. But as the devices are miniaturized to the nanoscales nowadays the modeling of these materials needs to be revised. In this chapter, we will show that one of the major players to determine the behavior of FEs in reduced sizes are thermal fluctuations. Although temperature-dependent potential coefficients is a common way to address the influence of temperature on FE properties [59–63], however, we will show that the secondary consideration of temperature as a stochastic electric field is also vital to get a full picture of finite size effects. Based on this understanding we simulate some FE-based thermal phenomena at nanoscales.

4.1 Temperature in Ferroelectrics as Noise

We start from the typical over-damped polarization equation of motion, for a single FE domain in the tetragonal phase, which is supplemented by noise :

$$\gamma_v \frac{\partial P}{\partial t} = -\frac{\partial F}{\partial P} + \eta(t), \quad (4.1)$$

which in fact is the time-dependent Ginzburg-Landau (TDGL) equation [64, 65] (for under-damped equation of motion see Eqs. (4.11) and (4.12)). P , F , γ_v and η are the polarization, free energy density, internal resistivity (the inverse of kinetic coefficient) and the stochastic electric field corresponding to the thermal fluctuations respectively. The noise is assumed to be Gaussian white with an autocorrelation $\langle \eta(t)\eta(t') \rangle = b\delta(t - t')$. To calculate b first we need the corresponding Fokker-Planck equation. Following the Kramers-Moyal recipe given in Ref. [9] (see also Sec. 2.1.1), the drift and diffusion coefficients are derived as $D^{(1)} = -\frac{\partial F}{\gamma_v \partial P}$ and $D^{(2)} = \frac{b}{2\gamma_v^2}$ respectively. By substitution of drift and diffusion coefficients into the Kramers-Moyal expansion, we reach the corresponding Fokker-Planck equation :

$$\frac{\partial}{\partial t} \Omega(P, t) = \frac{\partial}{\gamma_v \partial P} \left[\Omega \frac{\partial F}{\partial P} + \frac{b}{2\gamma_v} \frac{\partial \Omega}{\partial P} \right], \quad (4.2)$$

where $\Omega(P, t)dP$ denotes the differential probability of finding polarization between P and $P + dP$. Now if we impose the requirement that in statistical equilibrium ($\partial \Omega / \partial t = 0$) the Boltzmann distribution $\Omega = \Omega_0 \exp(-a^3 F / k_B T)$ is reached, we get $b = \frac{2k_B T \gamma_v}{a^3}$ [64–66].

a^3 is the FE domain volume and the important message is that, as the volume decreases the effect of thermal fluctuations is expected to increase. To check this formalism, we will calculate the thermally activated switching time numerically, as an example, and compare the results with existing formula for switching time based on other formalisms.

4.1.1 Thermally Activated Switching Time

Since at this stage our goal is to have an insight into the formalism provided earlier and compare it with other formalisms, we evaluate switching time for a very simple model so that using other formalisms is feasible. We consider a single FE domain in tetragonal phase with a free energy density of (Landau-Devonshire model) :

$$F = \frac{\alpha}{2}P^2 + \frac{\beta}{4}P^4 - PE, \quad (4.3)$$

with E as an external electric field. α and β are Landau coefficients. In the absence of external electric field, the system has two symmetric minima which correspond to two different stable orientations of polarization, up(\uparrow) and down(\downarrow). Thermally activated switching time (τ) is the averaged time in which the polarization stays in one orientation without switching to another one. When there is an external electric field, the symmetry is broken and different switching times are expected ($\tau_{\downarrow\uparrow}$ and $\tau_{\uparrow\downarrow}$). Using the Heun method for solving Eq. (4.2), polarization dynamics, including the switchings are obtained and shown in Fig. 4.1. Due to the stochastic nature of switchings at finite temperatures, we should take an average over switching times to reach a convergence.

In Fig. 4.2 switching times versus electric field and inverse temperature for sufficient simulation time interval ($\Delta \gg \tau$) are shown. As expected increasing temperature decreases the switching times and the external electric field is/isn't in favor of $\tau_{\uparrow\downarrow}/\tau_{\downarrow\uparrow}$.

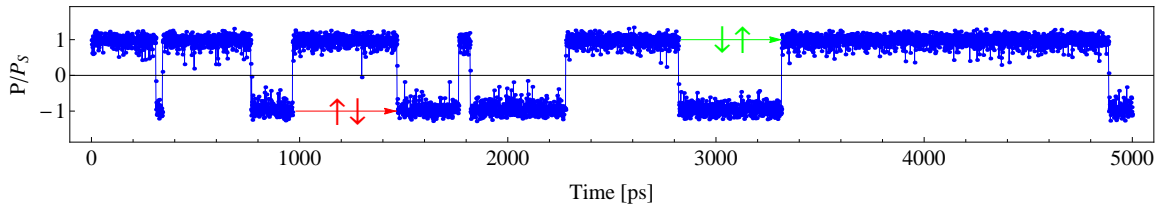


Figure 4.1: Reduced polarization $p(t) = P(t)/P_S$ versus time is shown, where $P_S = \sqrt{-\alpha/\beta} \approx 0.74 \text{ Cm}^{-2}$ is the spontaneous polarization. By averaging over red time intervals we evaluate $\tau_{\downarrow\uparrow}$ and by averaging over green time intervals we evaluate $\tau_{\uparrow\downarrow}$. Since the polarization will not relax *exactly* at the potential minima even after switching (due to thermal fluctuations), we define switching time as the time which reduced polarization passes from $p > 0.5$ to $p < -0.5$ and vice versa. In order to get more accurate results we should increase the simulation time interval Δ so that the averages are taken over more numbers of switchings. Here we put Landau coefficients as $\alpha = -11.57 \times 10^7 \text{ [VmC}^{-1}\text{]}$ and $\beta = 2.1 \times 10^8 \text{ [Vm}^5\text{C}^{-3}\text{]}$ [67] and $\Delta = 5000 \text{ [ps]}$, $a^3 = 10^{-27} \text{ [m}^3\text{]}$, $\gamma_v = 25 \times 10^{-6} \text{ [VmsC}^{-1}\text{]}$, $T = 200 \text{ [K]}$ and $E = 1 \text{ [MVm}^{-1}\text{]}$.

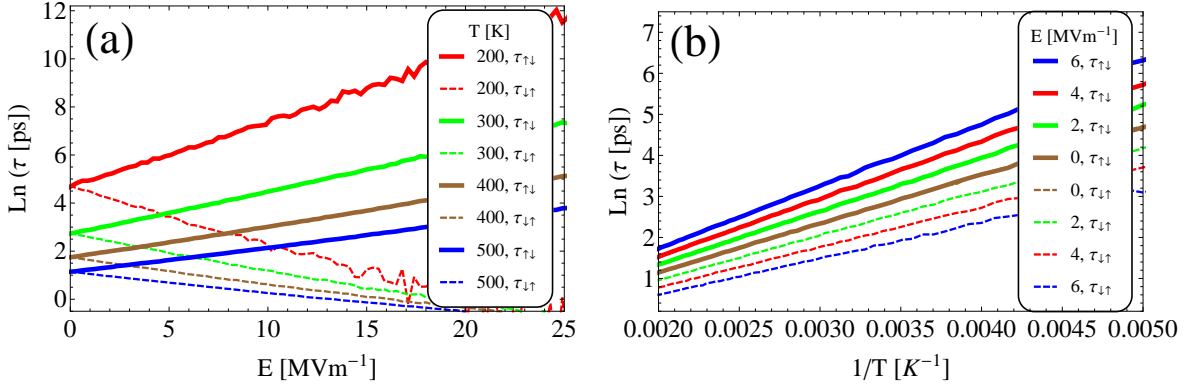


Figure 4.2: a) Switching times as a function of electric field for different temperatures. b) Switching times as a function of inverse temperature for different electric fields. For $E = 0$, τ_{\downarrow} (the solid brown curve) is over τ_{\uparrow} (the dashed brown curve). τ_{\downarrow} is the averaged time which polarization can stay up without switching and τ_{\uparrow} is the averaged time which polarization can stay down without switching (see Fig. 4.1). As switching time increases, to get a more accurate evaluation, the simulation time interval should be increased. Here the simulation time interval is fixed for all the cases ($\Delta = 1 \mu\text{s}$) and so a noisy behavior is seen as the switching time increases (either τ_{\downarrow} or τ_{\uparrow}). Here we assume for the Landau coefficients $\alpha = -11.57 \times 10^7 \text{ [VmC}^{-1}\text{]}$, $\beta = 2.1 \times 10^8 \text{ [Vm}^5\text{C}^{-3}\text{]}$ [67], $a^3 = 10^{-27} \text{ [m}^3\text{]}$, and $\gamma_v = 25 \times 10^{-6} \text{ [VmsC}^{-1}\text{]}$.

Another Formalism to Evaluate Switching Time : We introduced temperature as noise into the equation of motion and used Fokker-Planck formalism to find the relation between temperature and the strength of the noise and simulated the thermally activated switching times. Fortunately, there is a closed theoretical formula for switching time for our simple model (which enables us to assess our formalism) [67] :

$$\tau_{\downarrow\uparrow}^{-1} = v_0 \left(e^{W_{\uparrow}/k_B T} + e^{W_{\downarrow}/k_B T} \right), \quad (4.4)$$

where $W_{\uparrow,\downarrow}$ are the energies at minima. At small electric fields ($E \ll \frac{4}{3} \sqrt{-\frac{\alpha^3}{\beta}} \approx 114 \text{ MVm}^{-1}$) these energies can be approximated as $W_{\uparrow,\downarrow} \approx a^3 \left(-\frac{\alpha^2}{4\beta} \mp \sqrt{-\frac{\alpha}{\beta}} E \right)$. v_0 is the total number of trials per second to overcome the energy barrier between minima which experimentally corresponds to the frequency of the optical phonons in the crystals. The derivation of switching time formula can be found in Ref. [67] in details, however briefly we mention that it is derived from Pauli master equations : $\frac{d\Omega_{\uparrow}}{dt} = a_{\downarrow\uparrow}\Omega_{\downarrow} - a_{\uparrow\downarrow}\Omega_{\uparrow}$ and $\frac{d\Omega_{\downarrow}}{dt} = a_{\uparrow\downarrow}\Omega_{\uparrow} - a_{\downarrow\uparrow}\Omega_{\downarrow}$, where Ω_{\uparrow} and Ω_{\downarrow} are the probabilities for polarization oriented up and down and $a_{\downarrow\uparrow} = v_0 \exp(W_{\uparrow}/k_B T)$ are the transition probabilities at temperature T . By fitting $\ln(\tau) = -\ln(2v_0) + \frac{W}{k_B T}$ over the data at $E = 0$ in Fig. 4.2b we get $W \approx -1.63 \times 10^{-20} \text{ [J]}$ which is in good agreement with the theoretical value of the minimum energy $W = -a^3 \frac{\alpha^2}{4\beta} \approx -1.59 \times 10^{-20} \text{ [J]}$. Moreover, we can evaluate the frequency of the optical phonons as $v_0 \approx 1.68 \text{ [THz]}$.

Evaluating v_0 for different electric fields, Fig. 4.3a shows that there is an increase in frequency by increasing the electric field. Besides the experimental evidence [68], the dependency of v_0 on the electrical field is understandable since it presents the total number

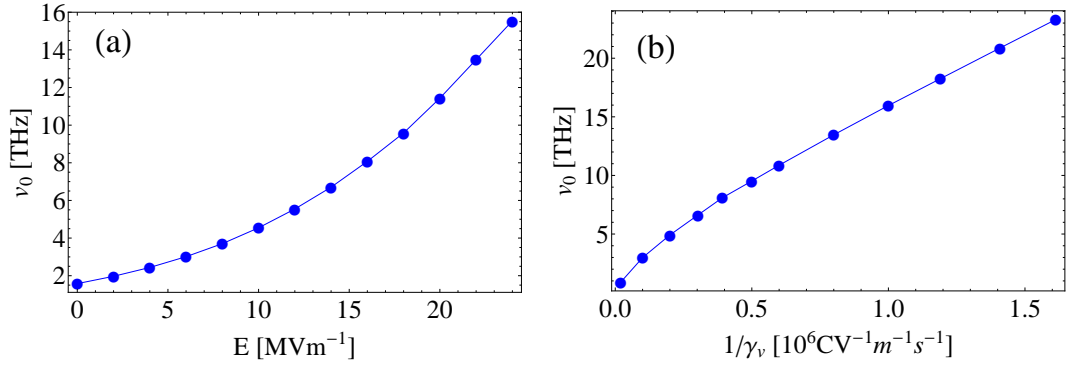


Figure 4.3: a) The frequency of optical phonons v_0 versus electric field for $a^3 = 10^{-27}$ [m³] and $\gamma_v = 25 \times 10^{-6}$ [VmsC⁻¹] is shown. v_0 is evaluated by fitting the switching time formula (Eq. (4.4)) on the simulated switching times. For better accuracy, we used the Taylor expansion of $W_{\uparrow,\downarrow}$ up to $O[E]^5$ in Eq. (4.4). b) The frequency of the optical phonons v_0 versus inverse internal resistivity at low temperatures for $a^3 = 10^{-27}$ [m³] and $E = 0$ is shown.

of trials per second to overcome the potential barrier which itself depends on the electric field. Increasing electric field decreases the potential barrier and so increases v_0 . Furthermore, the optical phonon frequency is expected to be related to the internal resistivity (γ_v) since there is no direct correspondence for internal resistivity in the Pauli master equation. Conceptually, γ_v shows the resistivity of FEs to release charges by the destruction of polarization (with a current density of $J = \frac{\partial P}{\partial t}$ (Eq. (4.1)), which reasonably should be related to the vibration of anions and cations in the FE atomic structures. In other word γ_v determines the resistivity of FE to go from one state to another state. In this sense, the inverse relation between optical phonon frequency and internal resistivity is understandable as shown in Fig. 4.3b.

4.2 Ferroelectric Phase Diagrams : Barium Titanate

In the previous section, we used a simple model just to show how we can introduce temperature as noise into the FEs. However to simulate FEs for a broad range of temperatures correctly, comparable with experimental measurements, the temperature must be introduced in the potential coefficients as well. The potential we use is the eight-order Ginzburg-Landau-Devonshire (GLD) for a prototypical perovskite FE, BaTiO₃ (BTO), which its phase dia-

gram has already studied extensively [61–63] :

$$\begin{aligned}
 F^{FE} = F^G + \sum_{\mathbf{n}} (\alpha_1(T_{\mathbf{n}}) + \Pi(Q_{11} + 2Q_{12})) \times (P_{x,\mathbf{n}}^2 + P_{y,\mathbf{n}}^2 + P_{z,\mathbf{n}}^2) + \alpha_{11}(P_{x,\mathbf{n}}^4 + P_{y,\mathbf{n}}^4 + P_{z,\mathbf{n}}^4) \\
 + \alpha_{12}(P_{x,\mathbf{n}}^2 P_{y,\mathbf{n}}^2 + P_{y,\mathbf{n}}^2 P_{z,\mathbf{n}}^2 + P_{x,\mathbf{n}}^2 P_{z,\mathbf{n}}^2) + \alpha_{111}(P_{x,\mathbf{n}}^6 + P_{y,\mathbf{n}}^6 + P_{z,\mathbf{n}}^6) \\
 + \alpha_{112}[P_{x,\mathbf{n}}^2(P_{y,\mathbf{n}}^4 + P_{z,\mathbf{n}}^4) + P_{y,\mathbf{n}}^2(P_{x,\mathbf{n}}^4 + P_{z,\mathbf{n}}^4) + P_{z,\mathbf{n}}^2(P_{x,\mathbf{n}}^4 + P_{y,\mathbf{n}}^4)] \\
 + \alpha_{123}P_{x,\mathbf{n}}^2 P_{y,\mathbf{n}}^2 P_{z,\mathbf{n}}^2 + \alpha_{1111}(P_{x,\mathbf{n}}^8 + P_{y,\mathbf{n}}^8 + P_{z,\mathbf{n}}^8) \\
 + \alpha_{1112}[P_{x,\mathbf{n}}^6(P_{y,\mathbf{n}}^2 + P_{z,\mathbf{n}}^2) + P_{y,\mathbf{n}}^6(P_{x,\mathbf{n}}^2 + P_{z,\mathbf{n}}^2) + P_{z,\mathbf{n}}^6(P_{x,\mathbf{n}}^2 + P_{y,\mathbf{n}}^2)] \\
 + \alpha_{1122}(P_{x,\mathbf{n}}^4 P_{y,\mathbf{n}}^4 + P_{y,\mathbf{n}}^4 P_{z,\mathbf{n}}^4 + P_{x,\mathbf{n}}^4 P_{z,\mathbf{n}}^4) \\
 + \alpha_{1123}(P_{x,\mathbf{n}}^4 P_{y,\mathbf{n}}^2 P_{z,\mathbf{n}}^2 + P_{y,\mathbf{n}}^4 P_{z,\mathbf{n}}^2 P_{x,\mathbf{n}}^2 + P_{z,\mathbf{n}}^4 P_{x,\mathbf{n}}^2 P_{y,\mathbf{n}}^2) \\
 - E_x P_{x,\mathbf{n}} - E_y P_{y,\mathbf{n}} - E_z P_{z,\mathbf{n}}, \\
 F^G = \sum_{\mathbf{n}} \frac{G_{11}}{2a^2} [(P_{x,x})^2 + (P_{y,y})^2 + (P_{z,z})^2] \\
 + G_{12}[P_{x,x}P_{y,y} + P_{y,y}P_{z,z} + P_{x,x}P_{z,z}] \\
 + \frac{G_{44}}{2a^2} [(P_{x,y} + P_{y,x})^2 + (P_{y,z} + P_{z,y})^2 + (P_{z,x} + P_{x,z})^2],
 \end{aligned} \tag{4.5}$$

where $\vec{P}_{\mathbf{n}}$, \vec{E} , Π and Q_{ij} are the polarization at site $\mathbf{n} = (n_x, n_y, n_z)$, electric field, hydrostatic pressure, and electrostrictive coefficients respectively. In F^G , $P_{x,y}$ means $P_{x,(n_x, n_y+1, n_z)}$ – $P_{x,(n_x, n_y, n_z)}$ and so on for other terms [69]. In this section, we focus on a single domain to get its phase diagram and later come back to the coupled FE domains. We use the parameters given in Tab. 4.1 and the same equation of motion as Eq. (4.1) with $\gamma_v \sim 2.5 \times 10^{-5}$ [VmsC⁻¹] [66] to evolve the system to its stationary state. Since the BTO has some structural phase transitions, calculation of its phase diagram is a bit tricky. First, we need to calculate the stationary value of the free energy of the system and the corresponding polarization at the stationary state for three different cases as shown in Fig. 4.5a, which correspond to three different structural phases (see Fig. 4.4). Then at each temperature we choose the polarization whose corresponding free energy has the minimum value. Within this recipe the transition temperatures are also obtained automatically which according to Fig. 4.5b are $T \sim 210$ [K] for Rhombohedral to Orthorhombic, $T \sim 280$ [K] for Orthorhombic to Tetragonal and $T \sim 390$ [K] for Tetragonal to Cubic. All presented quantities here, such as the free energy and the polarization, are averaged over the different realization of the noises. We can follow the same recipe to evaluate the phase diagrams for different pressures and electric fields. The results are shown in Figs. 4.6 and 4.7.

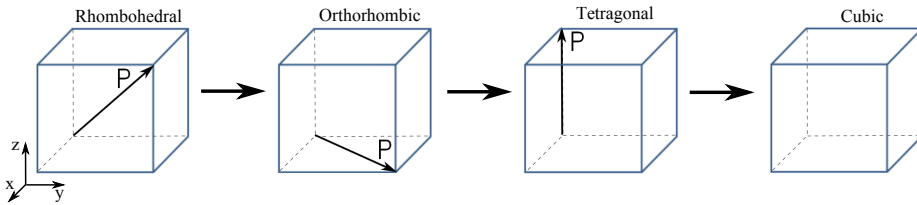


Figure 4.4: Polarization vector at different phases of BTO.

Table 4.1: BTO parameters [63] : T is temperature in Kelvin and $\sigma_1 = \sigma_2 = \sigma_3 = -\Pi$ are stress along the x,y and z direction in unit of [GPa].

Coefficients	Value	Units
α_1	$8.0 \times 10^7 \times \left[\coth\left(\frac{160}{T}\right) - \coth\left(\frac{160}{390}\right) \right]$	$[\text{C}^{-2}\text{mJ}]$
α_{11}	$-1.154 \times 10^8 \times [1 + 0.037(\sigma_1 + \sigma_2 + \sigma_3)]$	$[\text{C}^{-4}\text{m}^5\text{J}]$
α_{12}	$+6.530 \times 10^8 \times [1 + 0.037(\sigma_1 + \sigma_2 + \sigma_3)]$	$[\text{C}^{-4}\text{m}^5\text{J}]$
α_{111}	$-2.106 \times 10^9 \times [1 + 0.023(\sigma_1 + \sigma_2 + \sigma_3)]$	$[\text{C}^{-6}\text{m}^9\text{J}]$
α_{112}	$+4.091 \times 10^9 \times [1 + 0.023(\sigma_1 + \sigma_2 + \sigma_3)]$	$[\text{C}^{-6}\text{m}^9\text{J}]$
α_{123}	$-6.688 \times 10^9 \times [1 + 0.023(\sigma_1 + \sigma_2 + \sigma_3)]$	$[\text{C}^{-6}\text{m}^9\text{J}]$
α_{1111}	$+7.590 \times 10^{10}$	$[\text{C}^{-8}\text{m}^{13}\text{J}]$
α_{1112}	-2.193×10^{10}	$[\text{C}^{-8}\text{m}^{13}\text{J}]$
α_{1122}	-2.221×10^{10}	$[\text{C}^{-8}\text{m}^{13}\text{J}]$
α_{1123}	$+2.416 \times 10^{10}$	$[\text{C}^{-8}\text{m}^{13}\text{J}]$
Q_{11}	0.11	$[\text{C}^{-2}\text{m}^4]$
Q_{12}	-0.045	$[\text{C}^{-2}\text{m}^4]$

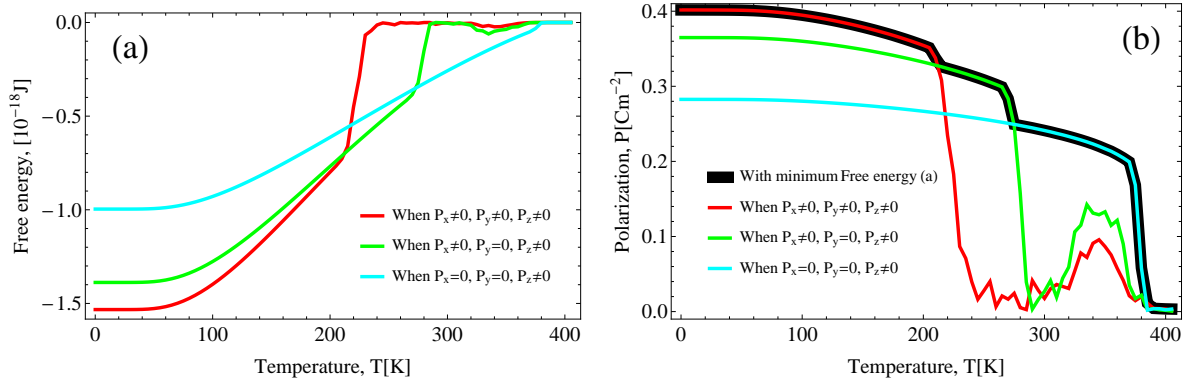


Figure 4.5: The procedure to obtain the phase diagram including the structural phase transitions. a) shows the free energies for three different cases which correspond to the three different structural phases. b) shows the corresponding polarization $P = \sqrt{P_x^2 + P_y^2 + P_z^2}$ to three different structural phases. At each temperature the polarization in which its corresponding free energy has the minimum value, represents the correct polarization which is marked by the thick black curve. Here $a = 5$ [nm].

Phase Instability in Reduced Sizes : The phase-transition temperatures as a function of the cell size are shown in Fig. 4.8. As expected, as the size of the FEs reduces the thermal fluctuations suppress polarization. In fact such a finite-size effect has already been observed in experiment [70–75], however, it has been mainly attributed to the depolarization field. Since the depolarization field is dismissed in our simulations we can conclude

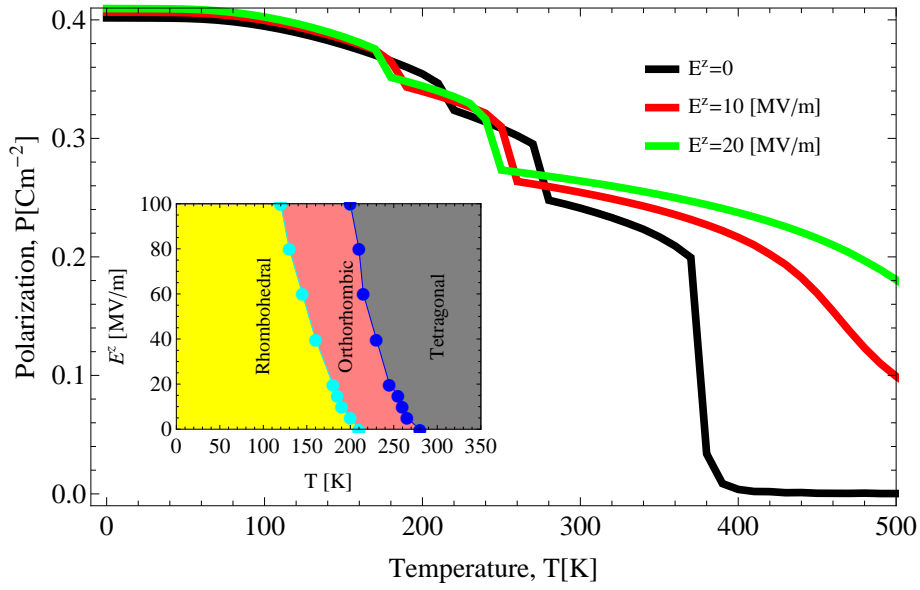


Figure 4.6: The BTO polarization and its phase diagram for different electric fields. Here $a = 5$ [nm] and $\Pi = 0$.

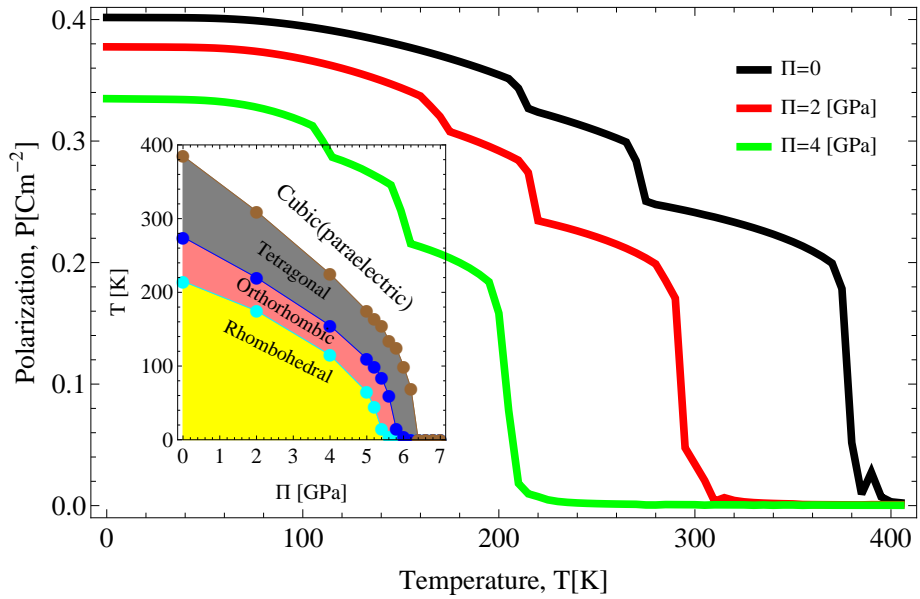


Figure 4.7: The BTO polarization and its phase diagram for different pressures. Here $a = 5$ [nm] and $E = 0$.

that the thermal fluctuations also could be a key factor for having polarization suppression at reduced sizes. As can be seen, as the size of the system increases the finite-size effects disappear gradually and we approach the well-known macroscopic values for the transition temperatures [63].

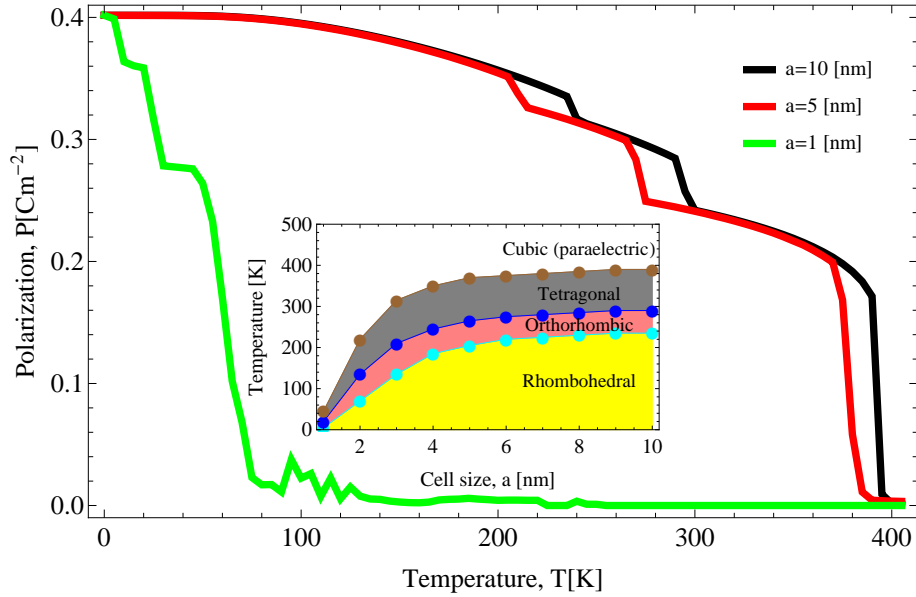


Figure 4.8: The BTO polarization and its phase diagram for different cell sizes. Here $E = 0$ and $\Pi = 0$.

4.3 Pyroelectric Effect : Barium Titanate

In this section, we show how a FE material can be used as a heat engine. The core idea is the temperature-dependency of hysteresis loops in FEs as shown in Fig. 4.9. This way of harvesting thermal energy out of FEs is known as pyroelectric effect [76–83]. Here we use the provided formalism in previous sections to simulate hysteresis loops. To exploit pyroelectric effect, we implement the Olsen cycle (Fig. 4.10), though other thermal-electrical cycles also exist [81, 83]. Our interested range of temperature is room temperature.

The temperature-dependency of hysteresis loops (or in other word polarization) is the key here because it provides us with an opportunity to have clockwise cycles (see Figs. 4.9 and 4.10). The area enclosed by the clockwise P-E loop determines the amount of harvested thermal energy which is in the form of electrical energy :

$$\varepsilon = -V_{FE} \oint \vec{E} \cdot d\vec{P} = V_{FE} \oint \vec{P} \cdot d\vec{E}, \quad (4.6)$$

where V_{FE} is the total volume of the FE material. Experimentally, the pyroelectric effect is observed as a flow of electric charges to and from the surface of FE materials and therefore to increase the efficiency of the pyroelectric engines the lost electrical energy must be decreased as much as possible. In principle, there are two main sources for this loss, hysteresis and Joule heating. Joule heating stems from finite resistance of ferroelectric material, however it could be eliminated by squeezing cycling time much smaller than the characteristic time of the system [81] $\tau \sim \varepsilon_r \varepsilon_0 \rho \simeq 1$ [s] where $\varepsilon_0 \sim 10^{-11}$ [AsV⁻¹m⁻¹], $\varepsilon_r \sim 10^4$ and $\rho \sim 10^7$ [VmA⁻¹] are the vacuum permittivity, relative permittivity and resistivity of BTO around room temperature respectively. In our simulations the cycling time is chosen much smaller than τ so that the relative loss due to charging and recharging can be neglected [84]. The inevitable energy loss for thermodynamic engines, which is manifested in the second law of thermodynamics, determines the maximum possible efficiency

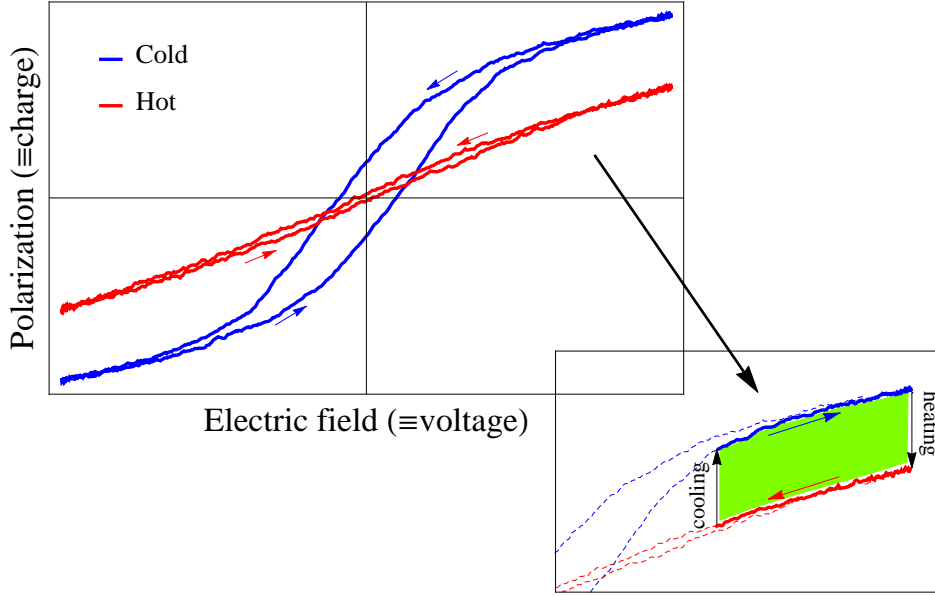


Figure 4.9: The area inside the anticlockwise cycles are equal to the amount of electrical energy converted to heat and the area inside the clockwise cycle is equal to the amount of converted heat to electrical energy. As can be seen, we can exploit the temperature-dependency of hysteresis loops to create a clockwise cycle. The green area shows the amount of produced electricity per cubic meter per cycle when the pyroelectric engine switches between cold and hot baths.

achieved by a heat engine. This maximum efficiency is known as *Carnot* efficiency :

$$\eta^c = 100 \times \left(1 - \frac{T_{cold}}{T_{hot}} \right). \quad (4.7)$$

On the other hand, we have a pyroelectric engine efficiency which indicates the percentage of heat converted to the electricity due to pyroelectric effect and is evaluated as

$$\eta^p = 100 \times \frac{\varepsilon}{Q}, \quad (4.8)$$

where Q is the thermal energy (heat) pumped into the FE material :

$$Q = c\rho V_{FE} (T_{hot} - T_{cold}), \quad (4.9)$$

with the specific heat $c \sim 450$ [Jkg⁻¹K⁻¹] and the mass density $\rho \sim 6000$ [kgm⁻³] at room temperature for BTO [85]. We take the temperature span ($T_{hot} - T_{cold}$) sufficiently large, so that the pumped transition heat leads to a constant temperature [77, 81, 83]. To get a feeling about the experimentally achieved pyroelectric engine efficiency, we refer to one of the earliest studies on $\text{Pb}_{0.99}\text{Nb}_{0.02}(\text{Zr}_{0.68}, \text{Sn}_{0.25}, \text{Ti}_{0.07})_{0.98}\text{O}_3$ for a temperature span of 20 [K] performed by Olsen [80, 81] which an efficiency of $\eta^p \sim 0.2$ % obtained while the Carnot efficiency was $\eta^c \sim 5$ %. Theoretically the efficiency of pyroelectric engines at room temperatures is known to be less than 1 % [77] because the energy required to increase the temperature of the lattice is nearly always much larger than the energy required to destroy the polarization, thus releasing electric charges. [84]

4.3.1 Model

At room temperature which is our interest, the BTO is in tetragonal phase. In such a case and under an external electric field for a set of coupled FE domains in x-y plane, the GLD potential reads :

$$F = F^G + \sum_{\mathbf{n}} (\alpha_1(T_{\mathbf{n}}) + \Pi(Q_{11} + 2Q_{12})) \times P_{\mathbf{n}}^2 + \alpha_{11}(\Pi)P_{\mathbf{n}}^4 + \alpha_{111}(\Pi)P_{\mathbf{n}}^6 + \alpha_{1111}P_{\mathbf{n}}^8 - EP_{\mathbf{n}},$$

$$F^G = \sum_{\mathbf{n}} \frac{G_{44}}{2a^2} (P_{(n_x+1, n_y)} - P_{(n_x, n_y)})^2 + \frac{G_{44}}{2a^2} (P_{(n_x, n_y+1)} - P_{(n_x, n_y)})^2,$$
(4.10)

where $G_{44} = 2 \times 10^{-11}$ [C⁻²m³J] [69]. Temperature is introduced into the system via the potential coefficients (see Tab. 4.1) plus a Gaussian white noise added to the non-

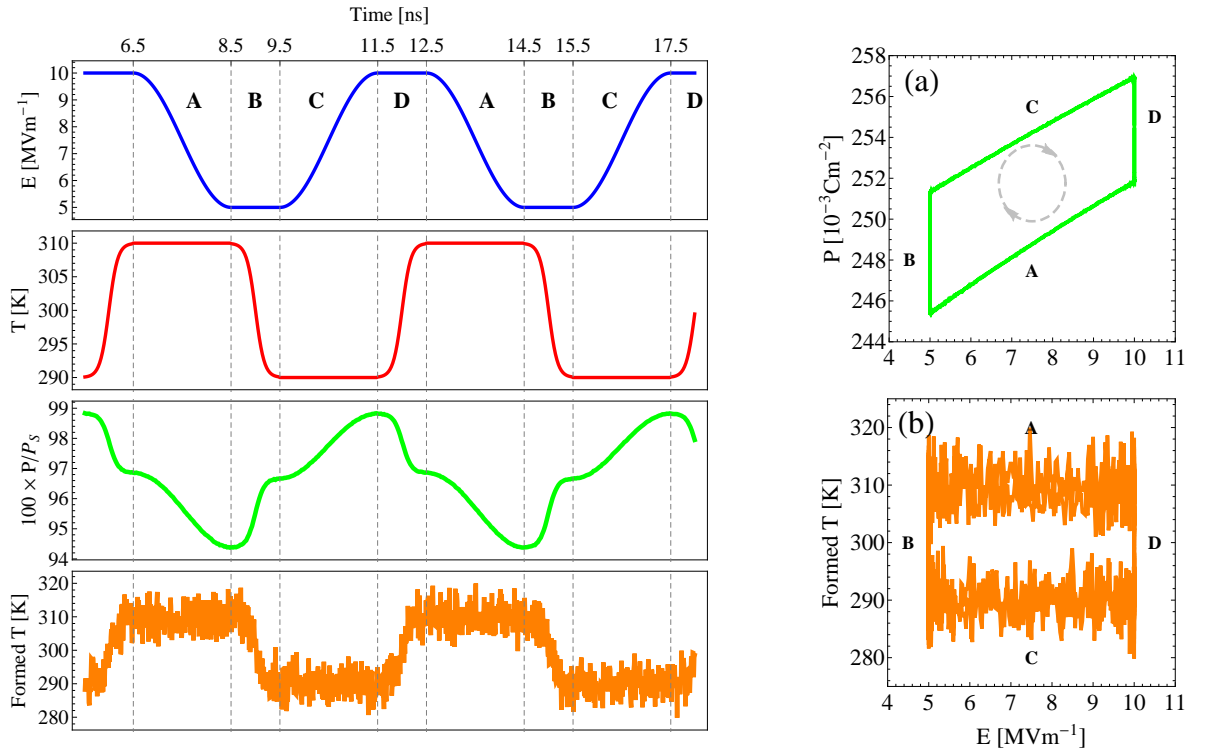


Figure 4.10: At the left the performance of an Olsen cycle is shown which includes : **A** isothermal discharging at high temperature, **B** isoelectric field cooling, **C** isothermal charging at low temperature, **D** isoelectric field heating. As can be understood from the formed temperature, during heating and cooling (**B** and **D**) the system has enough time to equilibrate with the heat baths. In the left the produced Olsen cycle is shown. The area inside the cycle is the produced electrical energy per cubic meter per cycle $e/V_{FE} = \oint PdE$. The system is kept at the standard atmosphere pressure $\Pi \sim 100$ [KPa].

equilibrium effective field :

$$E_{\mathbf{n}}^{eff} = -\frac{\partial F}{\partial P_{\mathbf{n}}} - \gamma_v \frac{dP_{\mathbf{n}}}{dt} + \eta_{\mathbf{n}}(t), \quad (4.11)$$

$$\langle \eta_{\mathbf{n}}(t) \eta_{\mathbf{n}'}(t') \rangle = \frac{2k_B T \gamma_v}{a^3} \delta(\mathbf{n} - \mathbf{n}') \delta(t - t').$$

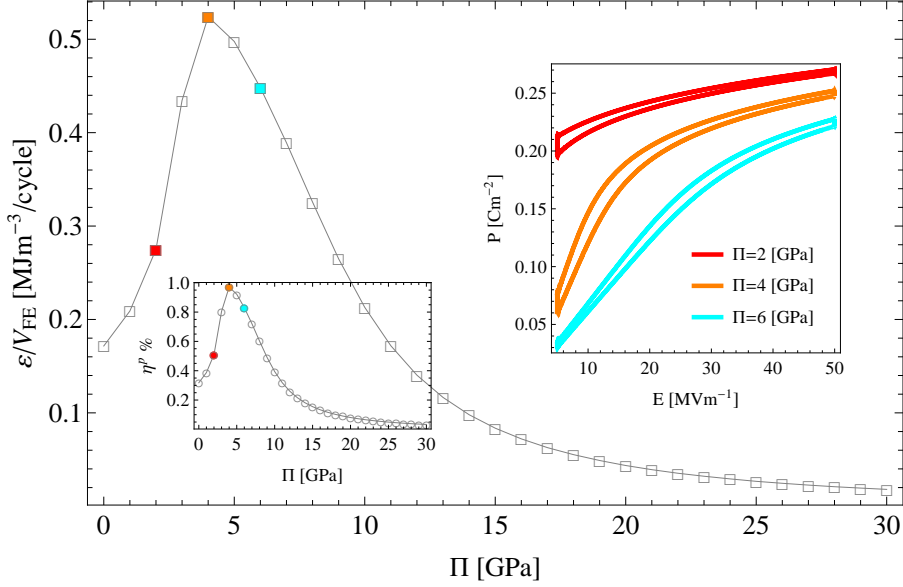


Figure 4.11: The produced electrical energy per cubic meter per cycle (ε/V_{FE}) and the corresponding efficiency (η^p) versus hydrostatic pressure (Π) is shown. The inset shows that increasing hydrostatic pressure is not necessarily in favor of Olsen cycle. The system is at room temperature ($T_{cold} = 290$ [K], $T_{hot} = 310$ [K]), $E_{low} = 5$ [MVm $^{-1}$], $E_{high} = 50$ [MVm $^{-1}$] and the cycling time is 12 [ns].

Here we use an under-damped equation of motion to get the dynamics of polarization :

$$\alpha_0 \frac{d^2 P_{\mathbf{n}}}{dt^2} = E_{\mathbf{n}}^{eff}, \quad (4.12)$$

which in fact is the extended Landau-Khalatnikov-Tani model with α_0 as the plasma frequency [65, 86–88] $\omega_0^2 = (\frac{G_{11}}{a^2})\alpha_0^{-1} \sim 10^{24}$ [s $^{-2}$]. Equivalently, we can add the kinetic term $\frac{1}{2}\alpha_0 \dot{P}_{\mathbf{n}}^2$ to the free energy density and use the over-damped TDGL equation (Eq. 4.1). It assists us to calculate the formed temperature in the system self-consistently via equipartition theorem to be sure that the system is equilibrated with the heat baths [89] :

$$T_{\mathbf{n}}^{Formed} = \frac{\alpha_0 a^3}{k_B} \langle \dot{P}_{\mathbf{n}}^2 \rangle, \quad (4.13)$$

where $\langle \dots \rangle$ means the average over the different realization of noises. All other quantities here are averaged over different realization of noises too.

We consider a system including 10×10 coupled FE cells with $a = 5$ [nm]. The non-zero component of polarization and external electric field are along the z axis and we switch the system between the heat baths with temperatures around room temperature ($T_{cold} = 290$ [K] and $T_{high} = 310$ [K]). In such a case $Q/V_{FE} = 54$ [MJm⁻³] and $\eta^c \sim 6.45$ % during all the simulations. As can be seen in Fig. 4.10 the temperature-dependency of the polarization can be used effectively to create a clockwise cycle. The produced electrical energy for such engine is evaluated at different pressures and shown in Fig. 4.11. As can be seen in the inset, the area enclosed by the Olsen cycles, and so the produced electrical energy, can be manipulated by changing an external parameter such as hydrostatic pressure.

4.4 An Alternative : Deterministic Heat Baths

In the attempt of providing a description for thermal effects, besides the mentioned stochastic heat baths, deterministic heat baths have also been proposed [90–93]. We close this chapter by addressing this alternative way briefly. We model a FE chain connected to the heat baths on both ends ($n = 1, N$) as thermostats, with a simple potential as :

$$F = F^G + \sum_{n=1}^N \alpha_1 P_n^2 + \alpha_{11} P_n^4, \quad F^G = \sum_{n=1}^N \frac{k}{2} (P_{n+1} - P_n)^2, \quad (4.14)$$

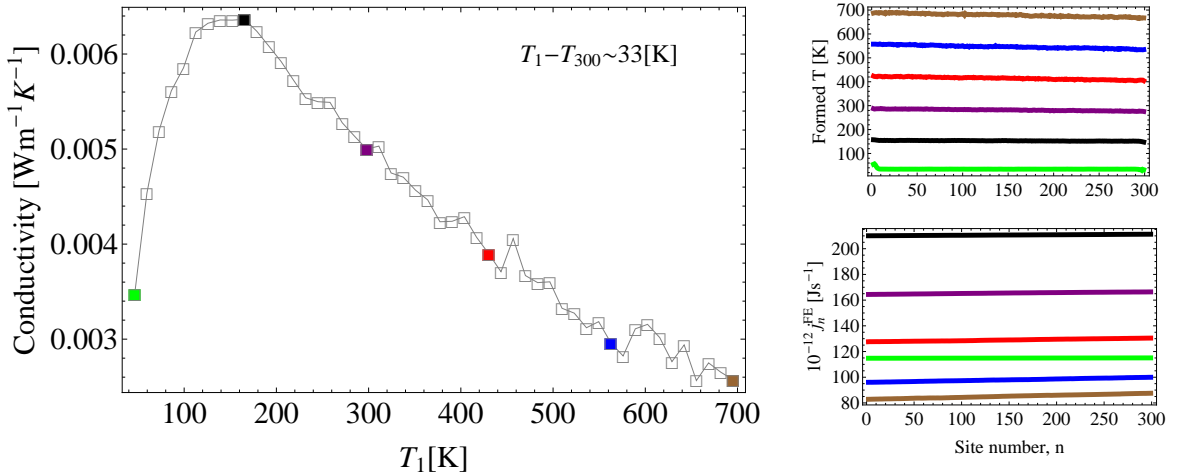


Figure 4.12: The left figure shows the conductivity of a FE chain under Nose-Hoover thermostats with $\alpha_1 = -1.385 \times 10^7$ [C⁻²mJ], $\alpha_{11} = 0.425 \times 10^8$ [C⁻⁴m⁵J]. We put $k = 1.3 \times 10^8$ [C⁻²mJ], $a = 1$ [nm] and $\alpha_0 = 1.3 \times 10^{-16}$ [C⁻²mJs²] as well. For the sake of simplicity, we assume that within the inspected temperature range system is in tetragonal phase and the potential coefficients are temperature independent. The right figures show the corresponding formed temperatures and heat currents.

and under the under-damped equation of motion (Eq. (4.12)) with :

$$\begin{aligned}
 E_n^{eff} &= -\frac{\partial F}{\partial P_n}, \quad n = 2, \dots, N-1, \\
 E_n^{eff} &= -\frac{\partial F}{\partial P_n} - g_n \dot{P}_n, \quad \dot{g}_n = \frac{\kappa}{T_n} \left[\frac{\alpha_0 a^3}{k_B} \dot{P}_n^2 - T_n \right], \quad n = 1, N
 \end{aligned}
 \tag{4.15}$$

where $g_{1,N}$ model the action of kind of thermostat known as the Nose-Hoover thermostat [90–93]. It works as the following : whenever the *formed* temperatures inside the system at the edges ($\frac{\alpha_0 a^3}{k_B} \dot{P}_n^2$) become larger than the temperature of the baths ($T_{1,N}$), $g_{1,N}$ increases and acts as a dissipator and vice versa, which altogether stabilize the formed temperatures on the edges around $T_{1,N}$. We evaluated the heat currents $\langle j_n^{FE} \rangle = -a^3 \langle \dot{P}_n \frac{\partial F^G}{\partial P_n} \rangle$ and formed temperatures $T_n^{Formed} = \frac{\alpha_0 a^3}{k_B} \langle \dot{P}_n^2 \rangle$ along the chain and calculated the conductivity $\frac{\sum \langle j_n^{FE} \rangle}{(T_1 - T_N) N a}$ [89, 90, 93]. Here by $\langle \dots \rangle$ we mean the time average when the system is more or less relaxed. The results are shown in Fig. 4.12. As expected, there is a peak in the conductivity which is related to the energy band structure of the system.

5 Multiferroics and Thermal Effects

So far we have studied the thermal effects in FMs and FEs separately. Now we want to focus on a new type of materials that show the properties of both FMs and FEs, i.e. Multiferroics (MFs). MFs are materials which simultaneously possess both spontaneous magnetization and spontaneous polarization [94, 95]. The interplay between magnetization and polarization in these materials allows a magnetic control of ferroelectric properties and an electric control of magnetic properties. Therefore, such materials have offered many possibilities for new devices. For example control of spin ordering in magnetic insulators with an applied electric field can significantly reduce the power consumption of memory devices. They can be used in integrated magnetic/electric devices, sensors, microelectromechanical systems, high-density memories, spintronics, etc. [84, 88, 96, 97].

The interplay between magnetization and polarization in MFs is done by magnetoelectric (ME) coupling which describes the influence of a magnetic field on the polarization, and an electric field on the magnetization. ME coupling may arise directly between the order parameters as in single-phase MFs [98, 99], or indirectly in composite MFs [96, 100–102]. We will discuss the single-phase and composite MFs in more details in the following sections, although finally we focus on composite ones due to their technological attractiveness.

5.1 Single-Phase Multiferroics : Bismuth Ferrite

In single-phase MFs the ferroelectricity and magnetism coexist with each other naturally. Bismuth ferrite BiFeO_3 (BFO) is a prototypical one. It is a commensurate FE and an incommensurate G-type antiferromagnet (AFM) (see Fig. 5.1a) with a Neel temperature of approximately 673 [K]. The spins are not collinear, but instead, take the form of a long-wavelength (~ 62 [nm]) spiral structure [103–105]. Being the only room-temperature MF so far, BFO has attracted great interest and extensive investigation in recent decades [106]. Using our experiences with FMs in previous chapters, here we simulate the magnetic phase of BFO and show how a stripe-pattern FE domain can be induced by the magnetic spiral structure (in the absence of thermal noises).

Micromagnetic simulation of AFMs, however, is not a trivial task because micromagnetic simulations are based on the continuity of magnetization and in AFMs the direction of the spins usually changes from lattice point to lattice point, which would result in a discretization length equal to the atomic lattice size. One way to tackle this problem is to divide the system into two FM sublattices with opposite magnetization so that within each sublattice the magnetic moments varies slowly in space and the micromagnetic simulations can be implemented [6]. But there is another way too, which is atomistic spin model simulations. We do the latter one. To do so, we choose a 2D system including 100×100 magnetic moments in a rectangular mesh (Fig. 5.1b) in which all the parameters involved in the Hamiltonian are in the order of the corresponding atomic-size ones (Tab. 5.1).

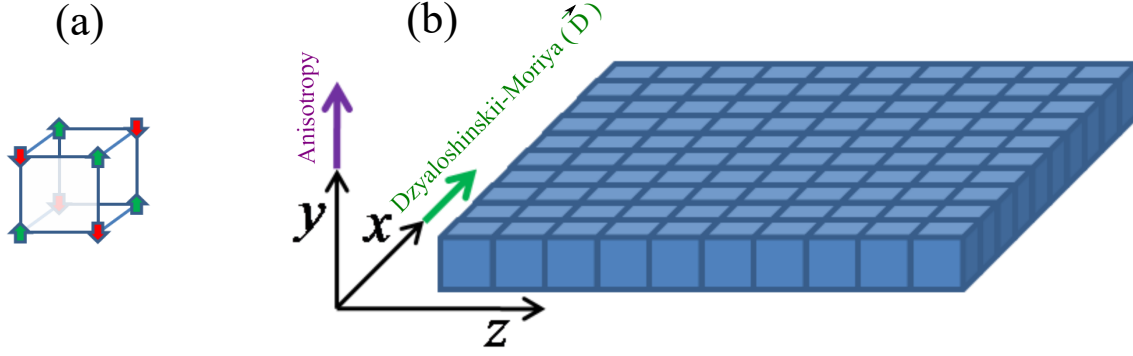


Figure 5.1: a) Schematic of a G-type AFM. b) Schematic of the simulated system for BFO. A two-dimensional system including $N_x \times N_z$ atomic cells in a rectangular mesh. The direction of anisotropy and DM interaction are shown.

Table 5.1: BFO parameters [103, 104]

Parameter	Values
Magnetic moment μ	$5.8 \mu_B$
Uniaxial anisotropy k	0.0068 [meV]
Nearest neighbors exchange interaction J	4.38 [meV]
Next-nearest neighbors exchange interaction J'	0.15 [meV]
DM interaction $ \vec{D} $	$ \vec{D} = 0.321^\ddagger$ [meV]
Damping parameter α	1.0^\dagger

[†] We have chosen a rather big value for the damping parameter to reduce the relaxation time of the system.

[‡] We have chosen a rather big value for DM interaction so that the spiral structure can be seen within our small model.

The Hamiltonian of BFO includes the following terms [103, 104] :

$$\begin{aligned}
 H = & J \sum_{n.n.} \hat{m}_{(n_x, n_z)} \cdot \hat{m}_{(n'_x, n'_z)} + J' \sum_{n.n.n.} \hat{m}_{(n_x, n_z)} \cdot \hat{m}_{(n'_x, n'_z)} \\
 & - \vec{D} \cdot \sum_{n.n.n.} \hat{m}_{(n_x, n_z)} \times \hat{m}_{(n'_x, n'_z)} - k \sum_{n_x, n_z} \left(m_{(n_x, n_z)}^y \right)^2,
 \end{aligned} \tag{5.1}$$

where $\hat{m}_{(n_x, n_z)}$ is the unit vector in the direction of magnetic moment at the site (n_x, n_z) and $\vec{\mu}_{(n_x, n_z)} = \mu \hat{m}_{(n_x, n_z)}$. \vec{D} is the chiral vector that characterizes the Dzyaloshinskii-Moriya (DM) interaction that underlies the magnetic spiral structure. The dynamics of magnetic moments are described by the atomistic LLG equations [6–8] :

$$\frac{\partial}{\partial t} \hat{m}_n(t) = -\frac{\gamma}{1 + \alpha^2} \hat{m}_n(t) \times \left[\vec{H}_n^{eff}(t) + \alpha \hat{m}_n(t) \times \vec{H}_n^{eff}(t) \right]. \tag{5.2}$$

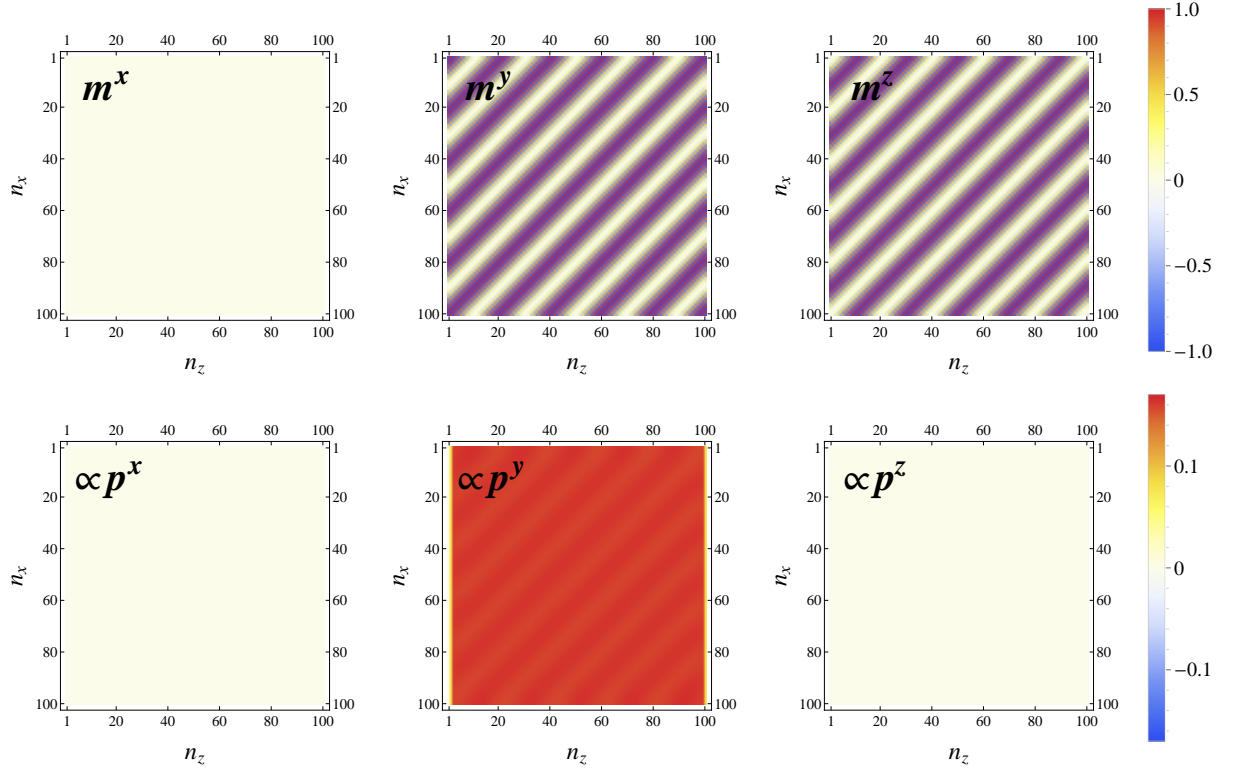


Figure 5.2: Top row : x,y and z components of the reduced magnetic moment vectors for a system of 100×100 atomic cells for the given parameters in Tab. 5.1. The purple color is, in fact, a visual effect that stems from mixing of red and blue colors because of the AFM structure of the system. The magnetic chirality and cycloid as a result of DM interaction ($|\vec{D}| = 0.321$ [meV]) can be seen more clearly in the 3D picture of the configuration of the magnetic moments in Fig. 5.3. Bottom row represents the structure of magnetically-induced electric polarization according to the Eq. (5.4).

The results are shown in Fig. 5.2 (top row). To get a better picture of the formed spiral structure, one row and one column of the system are shown in Fig. 5.3. We know that magnetism implies a breaking of time-reversal symmetry. For conventional ferroelectricity the spatial-inversion symmetry is broken. The non-centrosymmetric magnetic ordering induces so a ferroelectric state [107–110]; the polarization is therefore expected to be coupled to the magnetic ordering in such cases [111, 112]. The ME coupling between polarization and magnetization is derived from this general symmetry argument [113, 114] and leads to the following ME coupling term in the free energy

$$\Phi_{ME} \propto \vec{P} \cdot [\vec{\mu}(\vec{\nabla} \cdot \vec{\mu}) - (\vec{\mu} \cdot \vec{\nabla})\vec{\mu} + \dots], \quad (5.3)$$

with its minimization with respect to \vec{P} gives us the *magnetically-induced electric polarization* [98, 113, 115] :

$$\vec{P}_{(n_x, n_z)} \propto \left[\left(\vec{\mu}_{(n_x, n_z)} \cdot \vec{\partial} \right) \vec{\mu}_{(n_x, n_z)} - \vec{\mu}_{(n_x, n_z)} \left(\vec{\partial} \cdot \vec{\mu}_{(n_x, n_z)} \right) \right]. \quad (5.4)$$

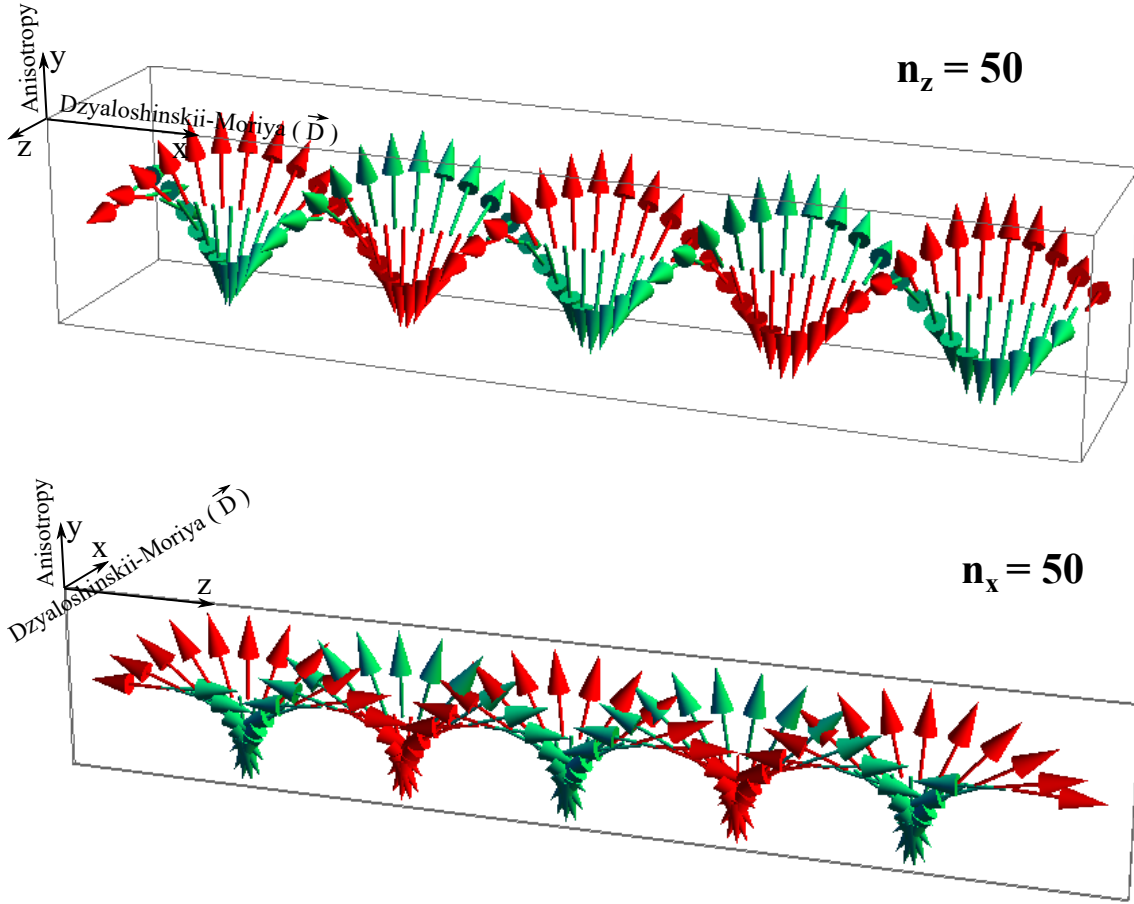


Figure 5.3: A 3D picture of magnetic moments for a chosen column and row of our 2D system in Fig. 5.2, top row. Different colors are given to the odd and even cell numbers to see the AFM order more clearly. As expected the magnetic moment vectors are perpendicular to the chiral vector ($|\vec{D}| = 0.321[\text{meV}]$) and the periodicity is close to the theoretical one : $2\pi \left(\frac{J-4J'}{2|\vec{D}|} \right) \approx 37$ [103].

Applying Eq. (5.4) to the formed magnetic spiral structure, the structure of induced polarization is obtained. As can be seen in the second row of Fig. 5.2, stripe-pattern FE domains appear in the system. However we should emphasize here that what we observe is the *induced* polarization and its contribution to the total polarization is more or less nothing due to the weakness of ME coupling. BFO belongs to the class of *proper* MFs in which the magnetism and ferroelectricity each arises from different sources [116, 117].

5.2 Composite Multiferroics

Single-phase MFs are rare and their ME coupling is either relatively weak or occurs at temperatures too low for practical applications. So with recent advances in deposition techniques, attentions have shifted beyond the single-phase MFs to manufacture composite MFs which possess much higher ME coupling even at room temperature [96]. In such MFs a break of time-reversal and spatial-inversion symmetry occurs between the magnetization and polarization across the interface of FM and FE materials [118–124]. Composite

MFs are particularly appealing not only because they have the properties of their parent compounds, but also because interactions between the magnetic and electric orders lead to additional functionalities. Here we mention two of these functionalities : MF diode and magnetically-controlled pyroelectric engine.

5.2.1 Multiferroic Diode

In electronics, the diodes are devices that allow a flow of current just in one direction. Similar devices have been proposed and made in other systems too. E.g. in phononics we can have diodes that allow a flow of phonons just in one direction [89] or in spintronics/magnonics the flow of magnons [125]. Such an asymmetry in conduction is called rectification. Here we show that a rectification can also occur in a composite MF (Fig. 5.4) [88].

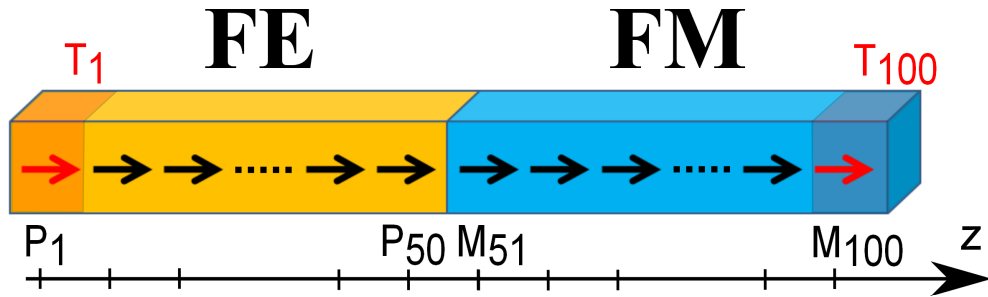


Figure 5.4: Schematic presentation of the MF diode including 50 FE cells and 50 FM cells. The first FE cell (with polarization P_1 at temperature T_1) and the last FM cell (with magnetization M_{100} at temperature T_{100}) play the role of thermostats. ME coupling happens at the interface between P_{50} and \vec{M}_{51} .

We use the following free energy density for our composite MF :

$$\begin{aligned}
 F &= F^{FM} + F^{FE} + F^{ME}, \\
 F^{FE} &= \sum_{n=1}^{50} \alpha_1 P_n^2 + \alpha_{11} P_n^4 + \sum_{n=1}^{50} \frac{\kappa}{2} (P_{n+1} - P_n)^2, \\
 F^{FM} &= -\frac{k}{M_S^2} \sum_{n=51}^{100} (M_n^z)^2 - \frac{2A}{a^2 M_S^2} \sum_{n=51}^{100} \vec{M}_n \cdot \vec{M}_{n+1}, \\
 F^{ME} &= -\lambda P_{50} M_{51}^z
 \end{aligned} \tag{5.5}$$

where f^{ME} corresponds to the ME coupling. The dynamics of order parameters are given by the extended Landau-Khalatnikov-Tani and LLG equations as the previous chapters :

$$\begin{aligned}
 \alpha_0 \frac{d^2 P_n}{dt^2} &= E_n^{eff}, \\
 \frac{\partial \vec{M}_n}{\partial t} &= -\frac{\gamma}{1 + \alpha^2} \vec{M}_n \times \vec{H}_n^{eff} - \frac{\gamma \alpha}{(1 + \alpha^2) M_S} \vec{M}_n \times (\vec{M}_n \times \vec{H}_n^{eff}),
 \end{aligned} \tag{5.6}$$

where the effective fields include a noise term due to finite temperature. However, here we just couple the edges of our MF (site $n = 1$ and $n = 100$) to the heat baths as thermostats (Langevin thermostat) and investigate the flow of heat current inside the FE/FM composite. The formula to calculate heat current in FE chain is the same as the one given in the previous chapter (Sec. 4.4). To calculate the heat current in FM chain, we use the Heisenberg equation of motion (similar to Sec. 3.1.1 to derive the spin current) $\frac{\partial h_{n,n+1}}{\partial t} = i[\Lambda, h_{n,n+1}]$, where $h_{n,n+1}$ is the local Hamiltonian (in reduced units) :

$$\Lambda = \sum_n h_{n,n+1} = \sum_n [J(\sigma_n^x \sigma_{n+1}^x + \sigma_n^y \sigma_{n+1}^y + \sigma_n^z \sigma_{n+1}^z) + K(\sigma_n^z)^2]. \quad (5.7)$$

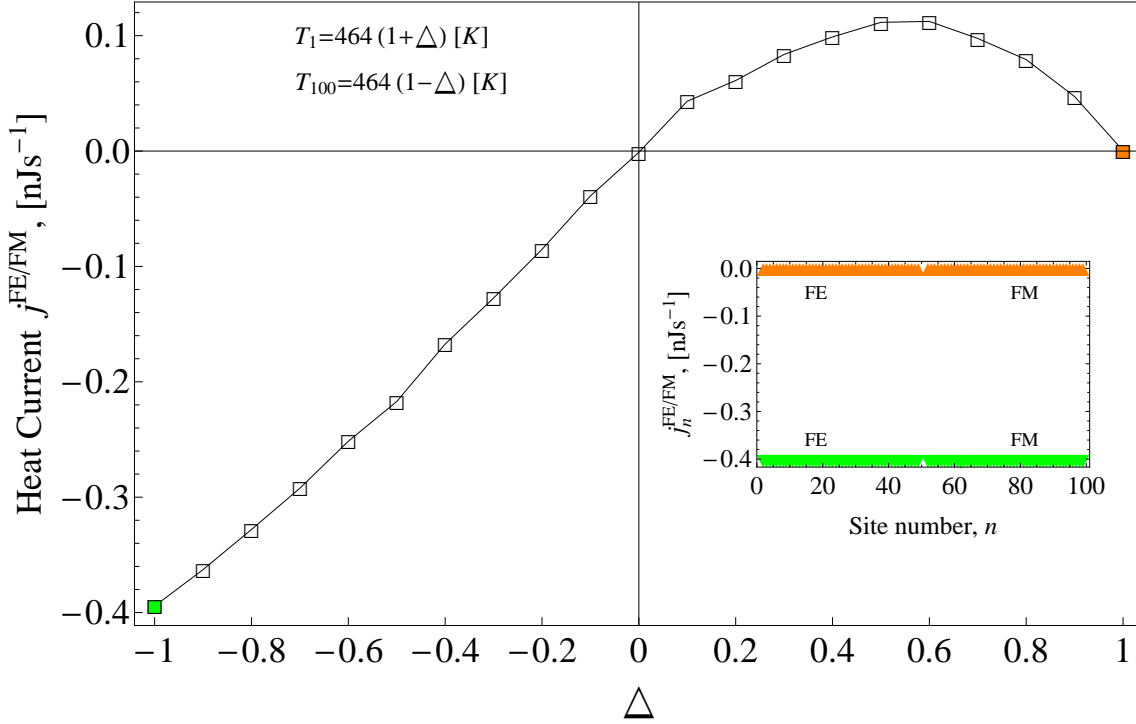


Figure 5.5: Heat current flowing inside the MF diode for different biased temperatures are shown. The rectification effect as the main characteristics of diodes is obvious. The FE parameters are the same as the Sec. 4.4 and the FM parameters belong to the Iron which we put $k \sim 2 \times 10^6$ $[\text{Jm}^{-3}]$ to include shape anisotropy and $\alpha = 1.0$ for fast convergence of numerical integration. Moreover, inside the system ($n = 2, \dots, 99$) we put internal resistivity (γ_v) and Gilbert damping (α) to zero so that the FE and FM subsystems play the role of perfect carriers and therefore we can conclude that rectification arises due to ME coupling at the interface. Here $\lambda \sim 20$ $[\text{sF}^{-1}]$.

After straightforward calculations, using spin commutator relation and considering the continuity equation we reach :

$$j_n^{FM} = J^2 (\sigma_{n-1}^x \sigma_n^y \sigma_{n+1}^z - \sigma_{n-1}^x \sigma_n^z \sigma_{n+1}^y + \sigma_{n-1}^y \sigma_n^z \sigma_{n+1}^x - \sigma_{n-1}^y \sigma_n^x \sigma_{n+1}^z + \sigma_{n-1}^z \sigma_n^x \sigma_{n+1}^y - \sigma_{n-1}^z \sigma_n^y \sigma_{n+1}^x) - 2KJ (\sigma_n^y \sigma_n^z \sigma_{n+1}^x - \sigma_n^x \sigma_n^z \sigma_{n+1}^y). \quad (5.8)$$

Considering the fact that the precession of magnetization is the negative of spin ($\vec{S}(\vec{r}, t) = -\frac{\vec{M}(\vec{r}, t)}{\gamma}$), in real units the heat current in FM chain reads [88]

$$j_n^{FM} = -\frac{4A^2\gamma}{M_S^4 a} (M_{n-1}^x M_n^y M_{n+1}^z - M_{n-1}^x M_n^z M_{n+1}^y + M_{n-1}^y M_n^z M_{n+1}^x - M_{n-1}^y M_n^x M_{n+1}^z + M_{n-1}^z M_n^x M_{n+1}^y - M_{n-1}^z M_n^y M_{n+1}^x) + \frac{4Aka\gamma}{M_S^4} (M_n^y M_n^z M_{n+1}^x - M_n^x M_n^z M_{n+1}^y). \quad (5.9)$$

The results are shown in Fig. 5.5. The rectification effect is evident. Conceptually, the rectifying effect is a nonlinear effect that stems from the temperature-dependency of the power spectrums. If the biased temperatures are chosen so that the power spectrums of FE and FM part overlap, a conduction is expected [89].

5.2.2 Magnetically-Controlled Pyroelectric Engine

Here we follow the same idea as the previous chapter to harvest thermal energy via BTO. However, here we couple BTO electromagnetically to a Co layer so that we can control the generated electrical energy magnetically. Our system of study is a 2D layer of BTO deposited by Co (Fig. 5.6) at room temperature. The contribution of ME coupling to the total free energy density is assumed to be $F^{ME} = -\lambda M_{\mathbf{n}}^z P_{\mathbf{n}}$ which results in a ME-mediated electric field as $E_{\mathbf{n}}^{ME} = -\frac{\partial F^{ME}}{\partial P_{\mathbf{n}}} = \lambda M_{\mathbf{n}}^z$ along the z axis. The FE potential and its equation of motion is the same as Sec. 4.3. We use the following free energy density for Co layer :

$$F^{FM} = \sum_{\mathbf{n}} \frac{k}{M_S^2} (M_{\mathbf{n}}^2 - (M_{\mathbf{n}}^z)^2) - \frac{A}{a^2 M_S^2} \vec{M}_{\mathbf{n}} \cdot \vec{M}_{\mathbf{n}'} + \frac{1}{2} \mu_0 (M_{\mathbf{n}}^z)^2 - H M_{\mathbf{n}}^z, \quad (5.10)$$

with $k = 410$ [kJm⁻³], $A = 31$ [pJm⁻¹] and $M_S = 1.44$ [MAm⁻¹] [33]. H is the external magnetic field along z, \mathbf{n}' represents the nearest neighbors and $\frac{1}{2} \mu_0 (M_{\mathbf{n}}^z)^2$ stands for the shape anisotropy. The dynamics of the magnetization are described by LLG equation with a Gilbert damping of $\alpha = 0.01$ [126].

We perform an Olsen cycle as the previous chapter (Sec. 4.3) for a FE and a FM layer with 10×10 cells and cell size of $a = 5$ [nm]. However, here an oscillatory magnetic field is applied to the composite so that during the cold isothermal process (C) be in +z direction and during the hot isothermal process (A) be in -z direction (Fig. 5.6). Due to ME coupling, this oscillatory magnetic field stretches the Olsen cycle and enhances the

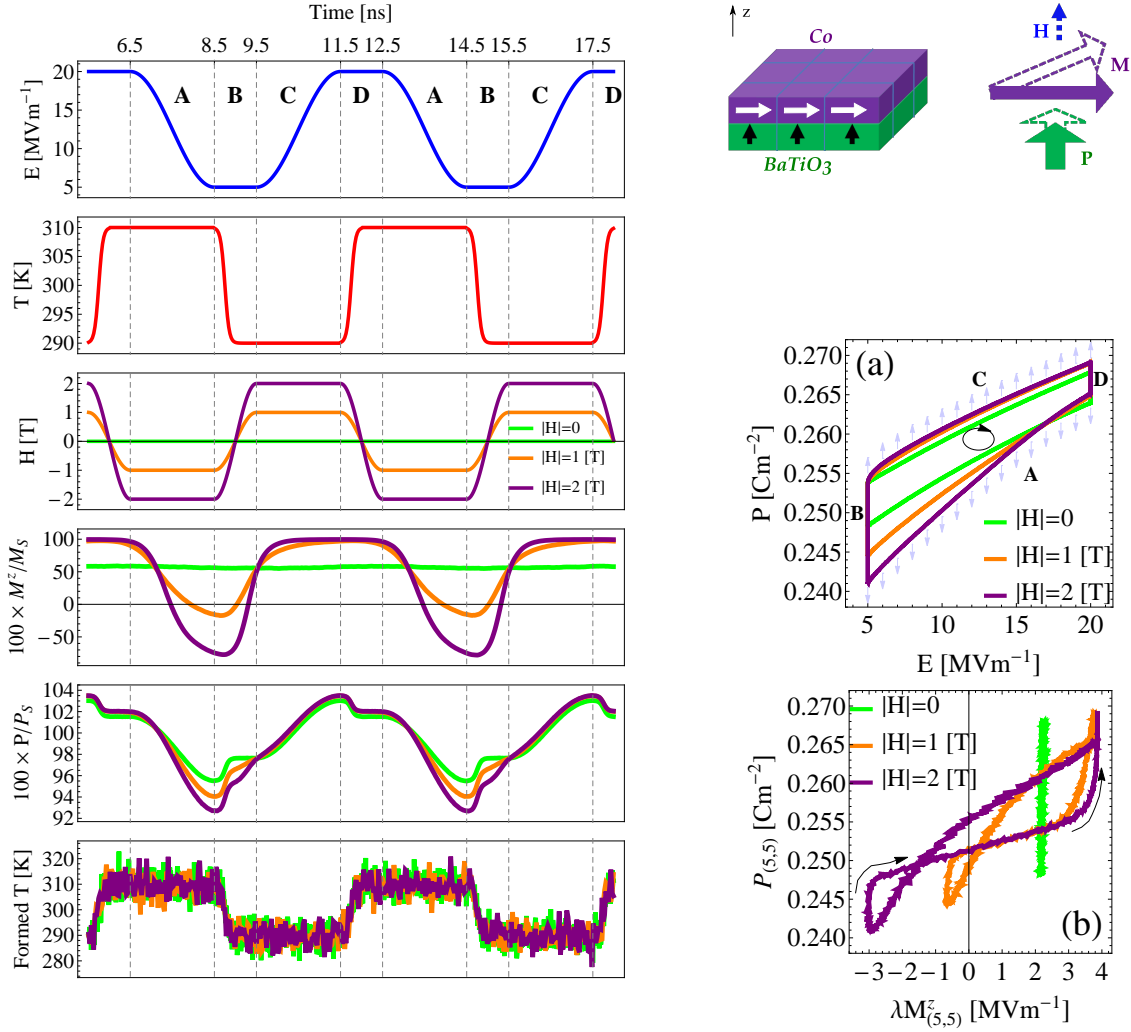


Figure 5.6: Up-right figure is the schematics of the magneto-electrically coupled Co/BaTiO₃. Both the ferroelectric polarization \mathbf{P} and the magnetization \mathbf{M} respond to an external magnetic field \mathbf{H} . Left figures show the time structure of the applied electric field E , the bath temperature T , the polarization $P = \sum_{\mathbf{n}} a^3 P_{\mathbf{n}} / V_{FE}$, and the magnetization $M^z = \sum_{\mathbf{n}} a^3 M_{\mathbf{n}}^z / V_{FM}$. The Olsen cycle passes through four processes as the previous chapter. To demonstrate the enhancement of the pyroelectric effect via the magnetic field, three magnetic field profiles are considered with $|H|^{max} = 0$ (green color), $|H|^{max} = 1$ [T] (orange color) and $|H|^{max} = 2$ [T] (purple color). Down-right figures : a) The corresponding Olsen cycle in $E - P$ space. The small arrows show the direction of the external magnetic field (H) which during **A** is directed along $-z$, and for **C** it is directed along $+z$. b) The polarization versus ME-mediated electric field ($E_{\mathbf{n}}^{ME} = \lambda M_{\mathbf{n}}^z$) at site $\mathbf{n} = (5, 5)$ is shown. The area enclosed by the loops determines the ME-mediated work per cubic meter done on the corresponding FE cell. To evaluate the total work done on the whole FE subsystem, the contribution of all other cells must be taken into account $w^{ME} = \sum_{\mathbf{n}} w_{\mathbf{n}}^{ME}$ (Eq. (5.11)). The calculations are performed at room temperature ($T_{cold} = 290$ [K], $T_{hot} = 310$ [K]) for $\lambda = 2.7$ [sF⁻¹] for a system of 10×10 FM/FE cells.

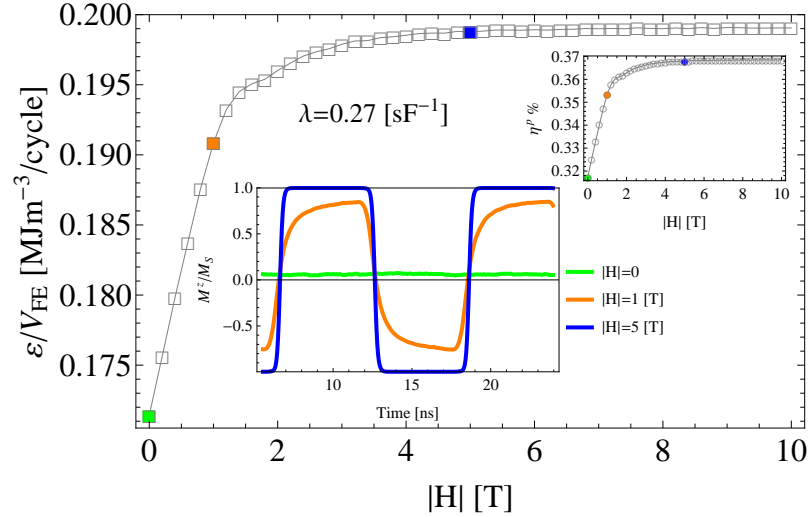


Figure 5.7: The produced electrical energy per cubic meter per cycle (ε/V_{FE}) and the corresponding efficiency (η^p) versus the amplitude of the oscillatory magnetic field ($|H|$). The system is at room temperature ($T_{cold} = 290$ [K], $T_{hot} = 310$ [K]) with $E_{low} = 5$ [MVm $^{-1}$], $E_{high} = 50$ [MVm $^{-1}$] and a cycling time of 12 [ns].

produced electrical energy, though it comes at the cost of doing some work on the FE subsystem :

$$w^{ME} = \sum_{\mathbf{n}} w_{\mathbf{n}}^{ME} = - \sum_{\mathbf{n}} a^3 \oint \lambda P_{\mathbf{n}} dM_{\mathbf{n}}^z. \quad (5.11)$$

Having w^{ME} we can evaluate the pyroelectric efficiency :

$$\eta^p = 100 \times \frac{\varepsilon}{Q + w^{ME}}. \quad (5.12)$$

The inspiration for applying this oscillatory magnetic field comes from the experiment in Ref. [127] where a compressive stress is used to stretch the Olsen cycle to enhance the pyroelectric effect. In fact, the strain-mediated ME coupling is a well-established mechanism in two-phase MFs (the strain induced in one component, either by magnetostriction in the FM or by the piezoelectric effect in the FE, is transferred to the other component and altering the polarization or magnetization) [102, 128–132].

Following the given procedure to perform the adapted Olsen cycle, in Fig. 5.7 the effect of the amplitude of the oscillatory magnetic field on the produced electrical energy and the corresponding efficiency is shown. Since magnetic field solely interacts with magnetization, it must be mediated by ME-mediated electric field $E_{\mathbf{n}}^{ME} = \lambda M_{\mathbf{n}}^z$ to affect the pyroelectric effect. It means that for the oscillatory magnetic fields with high amplitudes in which the z-component of the magnetization is saturated ($\uparrow |H| \Rightarrow M_{\mathbf{n}}^z \rightarrow M_S \Rightarrow E_{\mathbf{n}}^{ME} \rightarrow \lambda M_S$) (see the inset in Fig. 5.7) the effect of magnetic field to enhance the produced electrical energy is also saturated. [84]

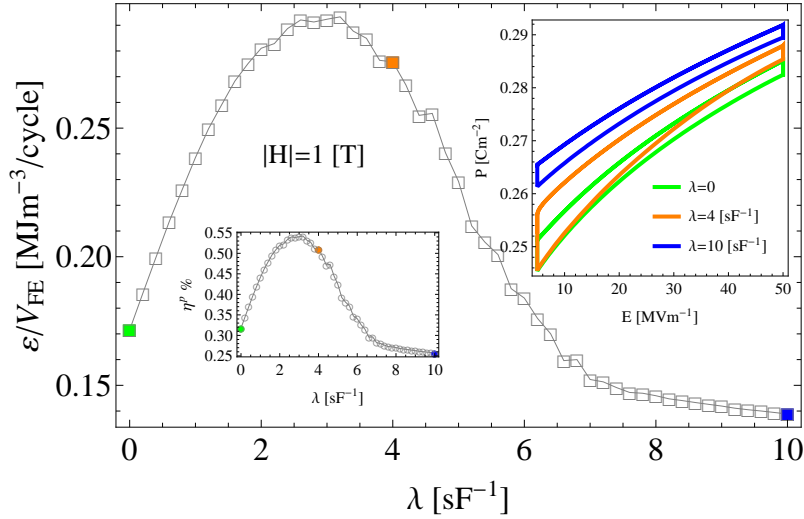


Figure 5.8: The produced electrical energy per cubic meter per cycle (ε/V_{FE}) and the corresponding efficiency (η^p) versus ME coupling (λ) is shown. The system is at room temperature ($T_{cold} = 290$ [K], $T_{hot} = 310$ [K]) with $E_{low} = 5$ [MVm^{-1}], $E_{high} = 50$ [MVm^{-1}] and a cycling time of 12 [ns].

One of the advantages of two-phase MFs is the possibility to manipulate their ME coupling [96, 98, 101, 128]. Although increasing the ME-coupling increases the effectiveness of the magnetic field to enhance the pyroelectric effect, but it also stabilizes the polarization so that releasing electric charges becomes more difficult. Therefore, it is expected that there is an optimum value for ME coupling in which the produced electrical energy has its maximum value as shown in Fig. 5.8.

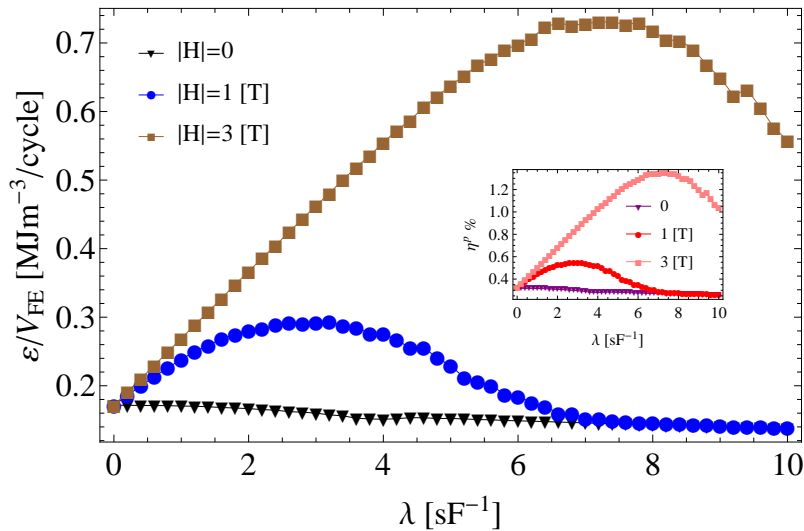


Figure 5.9: The produced electrical energy per cubic meter per cycle (ε/V_{FE}) and the corresponding efficiency (η^p) versus ME coupling for different values of $|H|$ is shown. The parameters are the same as the Fig. 5.8.

Finally, performing the simulations for different amplitudes of the oscillatory magnetic field (Fig. 5.9) we find that the ME coupling *alone* is not in favor of the pyroelectric effect ($|H| = 0$) and an oscillatory magnetic field is needed to enhance the produced electrical energy. It is because the ME coupling, alone, just makes the polarization more resistance to releasing charges. More important, comparison of the produced electrical energy in the presence and absence of ME coupling and in the presence and absence of the oscillatory magnetic field indicate that MFs potentially are better candidates to harvest thermal energy, than sole FEs. [84]

6 Summary, Conclusions, and Outlooks

6.1 Summary and Conclusions

Coming back to our motivation and goal in the General Introduction, in this thesis we investigated thermal effects in nanoscale ferromagnets, ferroelectrics, and their composition.

In chapter 2 we started from the building block of ferromagnets, i.e. magnetic moments, and step by step showed how the thermal fluctuations can be introduced into the ferromagnetic systems. We introduced the temperature by adding a stochastic magnetic field to the effective magnetic field (Eq. (2.10)). Using Kramers-Moyal expansion we derived the Fokker-Planck equation (Eq. (2.16)) which was the same as the one that had been derived earlier by other methods. The Fokker-Planck equation was used to uncover the quantitative relation between the temperature and the strength of the stochastic magnetic field (Eq. (2.17)). Having this relation, in the end of the chapter we investigated some thermal effects for a single ferromagnetic domain numerically. We calculated the thermal average of magnetization at equilibrium (Fig. 2.4) and the mean-first-passage time (Fig. 2.5). The theoretical formula for these quantities and for our simple model had already existed and confirmed the validity of our formalism and the reliability of our own developed code.

In chapter 3 we expanded our formalism to more complicated systems to study one of the most cited magnetothermal phenomena in recent years, i.e. spin Seebeck effect. First, we defined the spin current for a ferromagnetic insulator (Eq. (3.9)) and then calculated the spin current for a chain under a temperature gradient (Fig. 3.3). Calculating the spin current for different temperature gradients (Fig. 3.4) we reached the conclusion that it is the temperature gradient that drives the spin current. Moreover, calculating the magnon accumulation along the chain (Fig. 3.5), we uncovered the mechanism behind the longitudinal spin current in a ferromagnetic insulator as the following. Due to the temperature gradient, a nonuniform magnon accumulation is formed in the system so that in the hot part we have more magnons than the cold part. Therefore, the magnons flow from the hot to the cold part and form a spin current. Comparison of the magnon accumulation and the exchange torque profile (Fig. 3.3) indicated that it is the exchange torque that creates magnons in the hot part and absorbs them in the cold part. For sufficiently large systems, however, the exchange torque was zero far from the boundaries and no magnon was created or absorbed within this region and they just were moving from the hot to the cold part (Fig. 3.6).

Another important issue that we addressed was the frequency-characteristic of the generated spin current. We did time-resolved spin Seebeck effect in order to separate the contribution of different magnons with different modes in the spin current (Fig. 3.12). Using a low-pass filter we observed the occurrence of some intrinsic cutoff frequencies which corresponded to the magnons with low-wave vectors (Fig. 3.13). We concluded that the subthermal magnons have the main contribution to the longitudinal spin Seebeck effect.

To detect spin Seebeck effect experimentally, the spin current should be converted to an

electric current and it is done by a heavy normal metal, exploiting the inverse spin-Hall effect. Therefore, to have a better understanding of spin Seebeck effect measurements, we investigated the effect of the normal metal attached to the ferromagnet on the magnetization dynamics and the spin current. We found that the enhanced damping at the interface enhances the spin current and on the other hand the spin-transfer torque suppresses the spin current (Fig. 3.8).

In principle, the spin current can also flow perpendicular to the temperature gradient. This phenomenon is known as the transversal spin Seebeck effect. Calculating the magnon and phonon temperatures along the chain, we found that it is the difference between these temperatures that drives the transversal spin current (Figs. 3.9 and 3.10). When the magnon temperature is higher than the phonon temperature (which is assumed to be equal to the electron temperature in the adjacent normal metal) the angular momenta are passed from the magnetization in the ferromagnet to the spin system in the normal metal and vice versa.

At the end of chapter 3 we showed how the spin Seebeck effect can be used to move domain walls. We found that the speed of domain-wall motion increases as the temperature gradient increases (Fig. 3.16). We implemented a periodic temperature gradient to inspect the frequency-dependency of domain-wall motion. We found that increasing the frequency is not in favor of speeding the domain-wall motion (Fig. 3.16).

In line with our goal to study the thermal effects in ferroics, in chapter 4 we turned our attention to ferroelectrics. Again, using the same method as chapter 2, we derived the Fokker-Planck equation and showed how the thermal fluctuations can be introduced into the models for such materials (Eq. (4.2)). We calculated thermally activated switching time for a single ferroelectric domain and compared it with the theory to assure our formalism and our code works properly. As a result of this comparison, we also evaluated the frequency of optical phonons versus electric field and inverse internal resistivity (Fig. 4.3).

Since our specific ferroelectric materials of interest in this thesis have a Curie temperature much lower than the ones for ferromagnets and so consideration of the phase transitions is relevant, besides the thermal noise we also addressed the conventional way of introducing temperature in ferroelectrics via potential coefficients (Figs. 4.5, 4.6 and 4.7). We found that introducing temperature as a thermal noise along with temperature-dependent potential coefficients is the most appropriate way to describe the thermal behavior of ferroelectrics at nanoscales. We observed a phase instability at reduced sizes (Fig. 4.8) which has been reported frequently in the literature. Later, we simulated one of the most well-known effects used for thermal energy harvesting, that is the pyroelectric effect. We performed an Olsen cycle to exploit the temperature-dependency of hysteresis loops to produce electrical energy out of the heat baths (Fig. 4.10).

Finally, we collected all our experiences with ferromagnets and ferroelectrics to address multiferroics. Our main interest was two-phase multiferroics, though we also briefly showed how the Dzyaloshinskii-Moriya interaction can induce polarization in the single-phase multiferroics (Fig. 5.2). We simulated a multiferroic diode and showed the occurrence of rectification in a two-phase multiferroic (Fig. 5.5). Moreover, we exploited magnetoelectric coupling to enhance the pyroelectric effect via an external magnetic field (Fig. 5.6). Adapting the Olsen cycle by applying an oscillatory magnetic field to a two-phase multiferroic we got much higher efficiency for the pyroelectric engine in comparison with pyroelectric engines made of sole ferroelectrics (Fig. 5.9).

6.2 Outlooks

6.2.1 Pyromagnetic Engine

As we showed already, in a pyroelectric engine the temperature-dependency of hysteresis loops in ferroelectrics (polarization versus electric field) is used to harvest thermal energy as an electric current (via destruction of polarization). In analogy with this engine, we propose a pyromagnetic engine in which the temperature-dependency of hysteresis loops in ferromagnets (magnetization versus magnetic field) is used to harvest thermal energy as a magnon current (via destruction of magnetization) (Fig. 6.1). This new type of engine can be integrated into the spintronic devices as a spin current source. The performance of such engine is straightforward, as done for pyroelectric engine, however we need to extend our code to include transversal relaxation to have a pronounced effect. This is done by including Landau-Lifshitz-Bloch equation [2, 3, 16, 17].

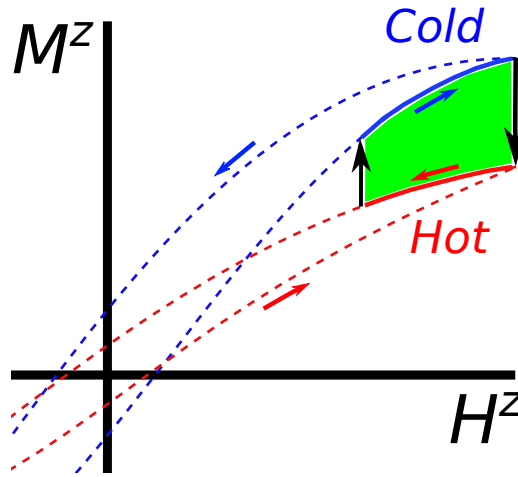


Figure 6.1: Schematic of the proposed pyromagnetic engine. The pyromagnetic engine exploits the temperature-dependency of ferromagnet hysteresis loops to create a clockwise loop.

To detect the generated spin current, we couple the pyromagnetic engine to a ferromagnetic chain with a uniform temperature and evaluate the spin current within this chain. Since the spin current within such FM chain in the absence of pyromagnetic engine must be zero (Fig. 3.4), the detection of spin current should be attributed to the coupled pyromagnetic engine.

6.2.2 Spin Seebeck Diode and Ratchet Spin Current via Dzyaloshinskii-Moriya Interaction

The second proposal is based on the nonreciprocity of spin waves due to Dzyaloshinskii-Moriya interaction (Fig. 6.2). We suspect that a rectification might appear when such

systems are biased to the heat baths, leading us to a new type of spin Seebeck diode. Moreover, this nonreciprocity might rise the chance of observing a spin current even when the system is not thermally biased but is at a finite temperature, leading us to a ratchet spin current [133].

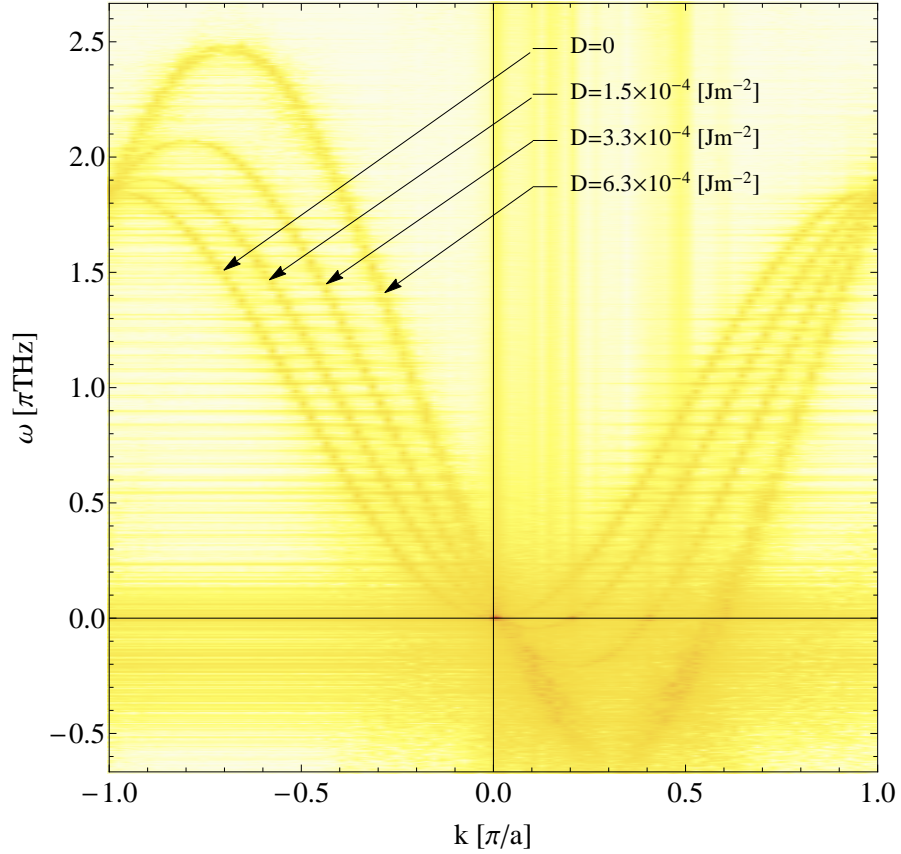


Figure 6.2: Spin-wave dispersion for different values of Dzyaloshinskii-Moriya interaction for a chain with $N = 100$ and $a = 10$ [nm] is shown. $H_0 = 0.1$ [T] and the other parameters belong to the Yttrium Iron Garnet (although in reality there is no such an interaction in this material, however, here just for the sake of showing the effect of Dzyaloshinskii-Moriya interaction, it is added). To achieve this, the term $\frac{2}{aM_S^2} \vec{D} \cdot \sum_{n=1}^N \vec{M}_n \times \vec{M}_{n+1}$ is added to the free energy density given in Eq. (3.22). Nonreciprocity due to Dzyaloshinskii-Moriya interaction is evident. Chiral vector (\vec{D}) is perpendicular to the chain and the simulations exactly match with $\omega_q = \gamma \left(H_0 + \frac{4A}{a^2 M_S} (1 - \cos(qa)) - \frac{4D}{a M_S} \sin(qa) \right)$ [134–136].

Bibliography

- [1] J. D. Jackson, *Classical Electrodynamics Third Edition* (Wiley, New York, 1998), 3rd ed.
- [2] N. Kazantseva, D. Hinzke, U. Nowak, R. W. Chantrell, U. Atxitia, and O. Chubykalo-Fesenko, *Physical Review B* **77**, 184428 (2008), URL <http://link.aps.org/doi/10.1103/PhysRevB.77.184428>.
- [3] D. A. Garanin and O. Chubykalo-Fesenko, *Physical Review B* **70**, 212409 (2004), URL <http://link.aps.org/doi/10.1103/PhysRevB.70.212409>.
- [4] R. Kubo, *Reports on Progress in Physics* **29**, 255 (1966), URL <http://stacks.iop.org/0034-4885/29/i=1/a=306>.
- [5] S. Blundell, *Magnetism in Condensed Matter* (OUP Oxford, 2001).
- [6] D. Suess, T. Schrefl, W. Scholz, J. V. Kim, R. L. Stamps, and J. Fidler, *IEEE Transactions on Magnetics* **38**, 2397 (2002).
- [7] R. F. L. Evans, W. J. Fan, P. Chureemart, T. A. Ostler, M. O. A. Ellis, and R. W. Chantrell, *Journal of Physics: Condensed Matter* **26**, 103202 (2014), URL <http://stacks.iop.org/0953-8984/26/i=10/a=103202>.
- [8] J. Barker, R. F. L. Evans, R. W. Chantrell, D. Hinzke, and U. Nowak, *Applied Physics Letters* **97**, 192504 (2010), URL <http://scitation.aip.org/content/aip/journal/apl/97/19/10.1063/1.3515928>.
- [9] H. Risken and T. Frank, *The Fokker-Planck Equation: Methods of Solution and Applications* (Springer, New York, 1996), 2nd ed.
- [10] K. L. Chung and F. AitSahlia, *Elementary Probability Theory: With Stochastic Processes and an Introduction to Mathematical Finance* (Springer, New York, 2006), 4th ed.
- [11] *Noise-Induced Transitions*, vol. 15 of *Springer Series in Synergetics* (Springer Berlin Heidelberg, 2006), URL <http://link.springer.com/10.1007/3-540-36852-3>.
- [12] G. B. Arfken, H. J. Weber, and F. E. Harris, *Mathematical Methods for Physicists, Seventh Edition: A Comprehensive Guide* (Academic Press, Amsterdam ; Boston, 2012), 7th ed.
- [13] W. F. Brown, *Physical Review* **130**, 1677 (1963), URL <http://link.aps.org/doi/10.1103/PhysRev.130.1677>.

- [14] I. D. Mayergoyz, G. Bertotti, and C. Serpico, *Nonlinear Magnetization Dynamics in Nanosystems* (Elsevier, 2009).
- [15] B. Hillebrands and K. Ounadjela, eds., *Spin Dynamics in Confined Magnetic Structures II*, vol. 87 of *Topics in Applied Physics* (Springer Berlin Heidelberg, Berlin, Heidelberg, 2003), URL <http://link.springer.com/10.1007/3-540-46097-7>.
- [16] D. A. Garanin, *Physical Review B* **55**, 3050 (1997), URL <http://link.aps.org/doi/10.1103/PhysRevB.55.3050>.
- [17] D. Hinzke and U. Nowak, *Physical Review Letters* **107** (2011), URL <http://link.aps.org/doi/10.1103/PhysRevLett.107.027205>.
- [18] J. L. Garcia-Palacios and F. J. Lazaro, *Physical Review B* **58**, 14937 (1998), URL <http://link.aps.org/doi/10.1103/PhysRevB.58.14937>.
- [19] W. Scholz, T. Schrefl, and J. Fidler, *Journal of Magnetism and Magnetic Materials* **233**, 296 (2001), URL <http://www.sciencedirect.com/science/article/pii/S0304885301000324>.
- [20] Y. Nakatani, Y. Uesaka, N. Hayashi, and H. Fukushima, *Journal of Magnetism and Magnetic Materials* **168**, 347 (1997), URL <http://www.sciencedirect.com/science/article/pii/S0304885396007251>.
- [21] R. K. Pathria and P. D. Beale, *Statistical Mechanics, Third Edition* (Academic Press, Amsterdam ; Boston, 2011), 3rd ed.
- [22] W. T. Coffey and Y. P. Kalmykov, *Journal of Applied Physics* **112**, 121301 (2012), URL <http://scitation.aip.org/content/aip/journal/jap/112/12/10.1063/1.4754272>.
- [23] P. E. Kloeden and E. Platen, *Numerical Solution of Stochastic Differential Equations* (Springer, Berlin ; New York, 1992), corrected edition ed.
- [24] G. E. P. Box and M. E. Muller, *The Annals of Mathematical Statistics* **29**, 610 (1958), URL <http://projecteuclid.org/euclid.aoms/1177706645>.
- [25] K. Uchida, S. Takahashi, K. Harii, J. Ieda, W. Koshibae, K. Ando, S. Maekawa, and E. Saitoh, *Nature* **455**, 778 (2008), URL <http://www.nature.com/nature/journal/v455/n7214/full/nature07321.html>.
- [26] Y. Kajiwara, K. Harii, S. Takahashi, J. Ohe, K. Uchida, M. Mizuguchi, H. Umezawa, H. Kawai, K. Ando, K. Takanashi, et al., *Nature* **464**, 262 (2010), URL <http://www.nature.com/nature/journal/v464/n7286/full/nature08876.html>.
- [27] S. M. Wu, J. E. Pearson, and A. Bhattacharya, *Physical Review Letters* **114**, 186602 (2015), URL <http://link.aps.org/doi/10.1103/PhysRevLett.114.186602>.

- [28] S. Seki, T. Ideue, M. Kubota, Y. Kozuka, R. Takagi, M. Nakamura, Y. Kaneko, M. Kawasaki, and Y. Tokura, *Physical Review Letters* **115**, 266601 (2015), URL <http://link.aps.org/doi/10.1103/PhysRevLett.115.266601>.
- [29] C. M. Jaworski, R. C. Myers, E. Johnston-Halperin, and J. P. Heremans, *Nature* **487**, 210 (2012), URL <http://www.nature.com/nature/journal/v487/n7406/full/nature11221.html>.
- [30] S. R. Etesami, L. Chotorlishvili, A. Sukhov, and J. Berakdar, *Physical Review B* **90**, 014410 (2014), URL <http://link.aps.org/doi/10.1103/PhysRevB.90.014410>.
- [31] S. Hoffman, K. Sato, and Y. Tserkovnyak, *Physical Review B* **88** (2013), URL <http://link.aps.org/doi/10.1103/PhysRevB.88.064408>.
- [32] J.-i. Ohe, H. Adachi, S. Takahashi, and S. Maekawa, *Physical Review B* **83**, 115118 (2011), URL <http://link.aps.org/doi/10.1103/PhysRevB.83.115118>.
- [33] J. M. D. Coey, *Magnetism and Magnetic Materials* (Cambridge University Press, 2010).
- [34] Wiley: *Handbook of Magnetism and Advanced Magnetic Materials, 5 Volume Set - Helmut Kronmüller, Stuart Parkin*, URL <http://eu.wiley.com/WileyCDA/WileyTitle/productCd-0470022175.html>.
- [35] U. Ritzmann, D. Hinzke, and U. Nowak, *Physical Review B* **89**, 024409 (2014), URL <http://link.aps.org/doi/10.1103/PhysRevB.89.024409>.
- [36] E. Saitoh, M. Ueda, H. Miyajima, and G. Tatara, *Applied Physics Letters* **88**, 182509 (2006), URL <http://scitation.aip.org/content/aip/journal/apl/88/18/10.1063/1.2199473>.
- [37] J.-i. Ohe, A. Takeuchi, and G. Tatara, *Physical Review Letters* **99**, 266603 (2007), URL <http://link.aps.org/doi/10.1103/PhysRevLett.99.266603>.
- [38] S. O. Valenzuela and M. Tinkham, *Nature* **442**, 176 (2006), URL <http://www.nature.com/nature/journal/v442/n7099/abs/nature04937.html>.
- [39] T. Kimura, Y. Otani, T. Sato, S. Takahashi, and S. Maekawa, *Physical Review Letters* **98**, 156601 (2007), URL <http://link.aps.org/doi/10.1103/PhysRevLett.98.156601>.
- [40] A. Kapelrud and A. Brataas, *Physical Review Letters* **111**, 097602 (2013), URL <http://link.aps.org/doi/10.1103/PhysRevLett.111.097602>.
- [41] A. Brataas, A. D. Kent, and H. Ohno, *Nature Materials* **11**, 372 (2012), URL <http://www.nature.com/nmat/journal/v11/n5/full/nmat3311.html>.

- [42] X. Jia, K. Liu, K. Xia, and G. E. W. Bauer, *EPL (Europhysics Letters)* **96**, 17005 (2011), URL <http://stacks.iop.org/0295-5075/96/i=1/a=17005>.
- [43] J. Stöhr and H. C. Siegmann, *Magnetism: from fundamentals to nanoscale dynamics* (Springer, 2006).
- [44] Y. Tserkovnyak, A. Brataas, G. E. W. Bauer, and B. I. Halperin, *Reviews of Modern Physics* **77**, 1375 (2005), URL <http://link.aps.org/doi/10.1103/RevModPhys.77.1375>.
- [45] L. Chotorlishvili, Z. Toklikishvili, A. Sukhov, P. P. Horley, V. K. Dugaev, V. R. Vieira, S. Trimper, and J. Berakdar, *Journal of Applied Physics* **114**, 123906 (2013), URL <http://scitation.aip.org/content/aip/journal/jap/114/12/10.1063/1.4822058>.
- [46] K. Uchida, J. Xiao, H. Adachi, J. Ohe, S. Takahashi, J. Ieda, T. Ota, Y. Kajiwara, H. Umezawa, H. Kawai, et al., *Nature Materials* **9**, 894 (2010), URL <http://www.nature.com/nmat/journal/v9/n11/full/nmat2856.html>.
- [47] J. Xiao, G. E. W. Bauer, K.-c. Uchida, E. Saitoh, and S. Maekawa, *Physical Review B* **81**, 214418 (2010), URL <http://link.aps.org/doi/10.1103/PhysRevB.81.214418>.
- [48] D. Kumar, O. Dmytriiev, S. Ponraj, and A. Barman, *Journal of Physics D: Applied Physics* **45**, 015001 (2012), URL <http://stacks.iop.org/0022-3727/45/i=1/a=015001>.
- [49] S. R. Etesami, L. Chotorlishvili, and J. Berakdar, *Applied Physics Letters* **107**, 132402 (2015), URL <http://scitation.aip.org/content/aip/journal/apl/107/13/10.1063/1.4931701>.
- [50] N. Roschewsky, M. Schreier, A. Kamra, F. Schade, K. Ganzhorn, S. Meyer, H. Huebl, S. Geprägs, R. Gross, and S. T. B. Goennenwein, *Applied Physics Letters* **104**, 202410 (2014), URL <http://scitation.aip.org/content/aip/journal/apl/104/20/10.1063/1.4879462>.
- [51] U. Atxitia, O. Chubykalo-Fesenko, R. W. Chantrell, U. Nowak, and A. Rebei, *Physical Review Letters* **102**, 057203 (2009), URL <http://link.aps.org/doi/10.1103/PhysRevLett.102.057203>.
- [52] K. Miyazaki and K. Seki, *The Journal of Chemical Physics* **108**, 7052 (1998), URL <http://scitation.aip.org/content/aip/journal/jcp/108/17/10.1063/1.476123>.
- [53] X.-g. Wang, G.-h. Guo, Y.-z. Nie, G.-f. Zhang, and Z.-x. Li, *Physical Review B* **86**, 054445 (2012), URL <http://link.aps.org/doi/10.1103/PhysRevB.86.054445>.
- [54] P. Yan, X. S. Wang, and X. R. Wang, *Physical Review Letters* **107**, 177207 (2011), URL <http://link.aps.org/doi/10.1103/PhysRevLett.107.177207>.

- [55] J. F. Scott, *Science* **315**, 954 (2007), URL <http://science.sciencemag.org/content/315/5814/954>.
- [56] J. F. Scott and C. A. P. d. Araujo, *Science* **246**, 1400 (1989), URL <http://science.sciencemag.org/content/246/4936/1400>.
- [57] Z. Hu, M. Tian, B. Nysten, and A. M. Jonas, *Nature Materials* **8**, 62 (2009), URL <http://www.nature.com/nmat/journal/v8/n1/abs/nmat2339.html>.
- [58] V. Garcia and M. Bibes, *Nature* **483**, 279 (2012), URL http://www.nature.com/nature/journal/v483/n7389/full/483279a.html?WT.ec_id=NATURE-20120315.
- [59] W. J. Merz, *Physical Review* **76**, 1221 (1949), URL <http://link.aps.org/doi/10.1103/PhysRev.76.1221>.
- [60] A. von Hippel, *Reviews of Modern Physics* **22**, 221 (1950), URL <http://link.aps.org/doi/10.1103/RevModPhys.22.221>.
- [61] Y. L. Li, L. E. Cross, and L. Q. Chen, *Journal of Applied Physics* **98**, 064101 (2005), URL <http://scitation.aip.org/content/aip/journal/jap/98/6/10.1063/1.2042528>.
- [62] Y. L. Wang, A. K. Tagantsev, D. Damjanovic, N. Setter, V. K. Yarmarkin, A. I. Sokolov, and I. A. Lukyanchuk, *Journal of Applied Physics* **101**, 104115 (2007), URL <http://scitation.aip.org/content/aip/journal/jap/101/10/10.1063/1.2733744>.
- [63] J. J. Wang, P. P. Wu, X. Q. Ma, and L. Q. Chen, *Journal of Applied Physics* **108**, 114105 (2010), URL <http://scitation.aip.org/content/aip/journal/jap/108/11/10.1063/1.3504194>.
- [64] S. Nambu and D. A. Sagala, *Physical Review B* **50**, 5838 (1994), URL <http://link.aps.org/doi/10.1103/PhysRevB.50.5838>.
- [65] S. Sivasubramanian, A. Widom, and Y. N. Srivastava, *Ferroelectrics* **300**, 43 (2004), URL <http://dx.doi.org/10.1080/00150190490442173>.
- [66] P. Marton and J. Hlinka, *Ferroelectrics* **373**, 139 (2008), URL <http://www.tandfonline.com/doi/abs/10.1080/00150190802409067>.
- [67] M. Vopsaroiu, J. Blackburn, M. G. Cain, and P. M. Weaver, *Physical Review B* **82**, 024109 (2010), URL <http://link.aps.org/doi/10.1103/PhysRevB.82.024109>.
- [68] J. M. Worlock and P. A. Fleury, *Physical Review Letters* **19**, 1176 (1967), URL <http://link.aps.org/doi/10.1103/PhysRevLett.19.1176>.
- [69] J. Hlinka and P. Marton, *Physical Review B* **74**, 104104 (2006), URL <http://link.aps.org/doi/10.1103/PhysRevB.74.104104>.

- [70] P. Sedykh, D. Michel, E. V. Charnaya, and J. Haase, *Ferroelectrics* **400**, 135 (2010), URL <http://dx.doi.org/10.1080/00150193.2010.505514>.
- [71] S. Li, J. A. Eastman, Z. Li, C. M. Foster, R. E. Newnham, and L. E. Cross, *Physics Letters A* **212**, 341 (1996), URL <http://www.sciencedirect.com/science/article/pii/0375960196000771>.
- [72] T. Hoshina, H. Kakemoto, T. Tsurumi, S. Wada, and M. Yashima, *Journal of Applied Physics* **99**, 054311 (2006), URL <http://scitation.aip.org/content/aip/journal/jap/99/5/10.1063/1.2179971>.
- [73] K. Ishikawa, K. Yoshikawa, and N. Okada, *Physical Review B* **37**, 5852 (1988), URL <http://link.aps.org/doi/10.1103/PhysRevB.37.5852>.
- [74] C. Lichtensteiger, J.-M. Triscone, J. Junquera, and P. Ghosez, *Physical Review Letters* **94**, 047603 (2005), URL <http://link.aps.org/doi/10.1103/PhysRevLett.94.047603>.
- [75] J. Junquera and P. Ghosez, *Nature* **422**, 506 (2003), URL <http://www.nature.com/nature/journal/v422/n6931/abs/nature01501.html>.
- [76] J. D. Childress, *Journal of Applied Physics* **33**, 1793 (1962), URL <http://scitation.aip.org/content/aip/journal/jap/33/5/10.1063/1.1728833>.
- [77] E. Fatuzzo, H. Kiess, and R. Nitsche, *Journal of Applied Physics* **37**, 510 (1966), URL <http://scitation.aip.org/content/aip/journal/jap/37/2/10.1063/1.1708205>.
- [78] A. v. d. Ziel, *Journal of Applied Physics* **45**, 4128 (1974), URL <http://scitation.aip.org/content/aip/journal/jap/45/9/10.1063/1.1663926>.
- [79] R. B. Olsen, J. M. Briscoe, D. A. Bruno, and W. F. Butler, *Ferroelectrics* **38**, 975 (1981), URL <http://dx.doi.org/10.1080/00150198108209595>.
- [80] R. B. Olsen and D. D. Brown, *Ferroelectrics* **40**, 17 (1982), URL <http://dx.doi.org/10.1080/00150198208210592>.
- [81] R. B. Olsen, *Journal of Energy* **6**, 91 (1982), URL <http://dx.doi.org/10.2514/3.62580>.
- [82] R. B. Olsen, D. A. Bruno, J. M. Briscoe, and J. Dullea, *Ferroelectrics* **59**, 205 (1984), URL <http://dx.doi.org/10.1080/00150198408240091>.
- [83] R. B. Olsen, D. A. Bruno, and J. M. Briscoe, *Journal of Applied Physics* **58**, 4709 (1985), URL <http://scitation.aip.org/content/aip/journal/jap/58/12/10.1063/1.336244>.
- [84] S. R. Etesami and J. Berakdar, *Applied Physics Letters* **108**, 053903 (2016), URL <http://scitation.aip.org/content/aip/journal/apl/108/5/10.1063/1.4941541>.

- [85] S. T. Davitadze, S. N. Kravchun, B. A. Strukov, B. M. Goltzman, V. V. Lemanov, and S. G. Shulman, *Applied Physics Letters* **80**, 1631 (2002), URL <http://scitation.aip.org/content/aip/journal/apl/80/9/10.1063/1.1454212>.
- [86] J. L. Servoin, F. Gervais, A. M. Quittet, and Y. Luspín, *Physical Review B* **21**, 2038 (1980), URL <http://link.aps.org/doi/10.1103/PhysRevB.21.2038>.
- [87] J. Hlinka, J. Petzelt, S. Kamba, D. Noujni, and T. Ostapchuk, *Phase Transitions* **79**, 41 (2006), URL <http://dx.doi.org/10.1080/01411590500476438>.
- [88] L. Chotorlishvili, S. R. Etesami, J. Berakdar, R. Khomeriki, and J. Ren, *Physical Review B* **92**, 134424 (2015), URL <http://link.aps.org/doi/10.1103/PhysRevB.92.134424>.
- [89] N. Li, J. Ren, L. Wang, G. Zhang, P. Hänggi, and B. Li, *Reviews of Modern Physics* **84**, 1045 (2012), URL <http://link.aps.org/doi/10.1103/RevModPhys.84.1045>.
- [90] S. Lepri, R. Livi, and A. Politi, *Physical Review Letters* **78**, 1896 (1997), URL <http://link.aps.org/doi/10.1103/PhysRevLett.78.1896>.
- [91] S. Nose, *The Journal of Chemical Physics* **81**, 511 (1984), URL <http://scitation.aip.org/content/aip/journal/jcp/81/1/10.1063/1.447334>.
- [92] W. G. Hoover, *Physical Review A* **31**, 1695 (1985), URL <http://link.aps.org/doi/10.1103/PhysRevA.31.1695>.
- [93] S. Lepri, *Physics Reports* **377**, 1 (2003), URL <http://linkinghub.elsevier.com/retrieve/pii/S0370157302005586>.
- [94] W. Eerenstein, N. D. Mathur, and J. F. Scott, *Nature* **442**, 759 (2006), URL <http://www.nature.com/nature/journal/v442/n7104/abs/nature05023.html>.
- [95] D. Khomskii, *Physics* **2** (2009), URL <http://link.aps.org/doi/10.1103/Physics.2.20>.
- [96] C.-W. Nan, M. I. Bichurin, S. Dong, D. Viehland, and G. Srinivasan, *Journal of Applied Physics* **103**, 031101 (2008), URL <http://scitation.aip.org/content/aip/journal/jap/103/3/10.1063/1.2836410>.
- [97] M. Mostovoy, *Physics* **5** **16** (2012), URL <http://physics.aps.org/articles/v5/16>.
- [98] K. F. Wang, J.-M. Liu, and Z. F. Ren, *Advances in Physics* **58**, 321 (2009), URL <http://dx.doi.org/10.1080/00018730902920554>.
- [99] M. Fiebig, *Journal of Physics D: Applied Physics* **38**, R123 (2005), URL <http://stacks.iop.org/0022-3727/38/i=8/a=R01>.

- [100] Y. Wang, J. Hu, Y. Lin, and C.-W. Nan, *NPG Asia Materials* **2**, 61 (2010), URL <http://www.nature.com/am/journal/v2/n2/full/am201054a.html>.
- [101] C. A. F. Vaz and U. Staub, *Journal of Materials Chemistry C* **1**, 6731 (2013), URL <http://pubs.rsc.org/en/content/articlelanding/2013/tc/c3tc31428f>.
- [102] S. Valencia, A. Crassous, L. Bocher, V. Garcia, X. Moya, R. O. Cherifi, C. Deranlot, K. Bouzehouane, S. Fusil, A. Zobelli, et al., *Nature Materials* **10**, 753 (2011), URL <http://www.nature.com/nmat/journal/v10/n10/full/nmat3098.html>.
- [103] J. Jeong, E. A. Goremychkin, T. Guidi, K. Nakajima, G. S. Jeon, S.-A. Kim, S. Furukawa, Y. B. Kim, S. Lee, V. Kiryukhin, et al., *Physical Review Letters* **108**, 077202 (2012), URL <http://link.aps.org/doi/10.1103/PhysRevLett.108.077202>.
- [104] M. Matsuda, R. S. Fishman, T. Hong, C. H. Lee, T. Ushiyama, Y. Yanagisawa, Y. Tomioka, and T. Ito, *Physical Review Letters* **109**, 067205 (2012), URL <http://link.aps.org/doi/10.1103/PhysRevLett.109.067205>.
- [105] S. Lisenkov, D. Rahmedov, and L. Bellaiche, *Physical Review Letters* **103**, 047204 (2009), URL <http://link.aps.org/doi/10.1103/PhysRevLett.103.047204>.
- [106] G. Catalan and J. F. Scott, *Advanced Materials* **21**, 2463 (2009), URL <http://onlinelibrary.wiley.com/doi/10.1002/adma.200802849/abstract>.
- [107] T. Kimura, T. Goto, H. Shintani, K. Ishizaka, T. Arima, and Y. Tokura, *Nature* **426**, 55 (2003), URL <http://www.nature.com/nature/journal/v426/n6962/abs/nature02018.html>.
- [108] J. F. Scott, *Reports on Progress in Physics* **42**, 1055 (1979), URL <http://stacks.iop.org/0034-4885/42/i=6/a=003>.
- [109] D. L. Fox and J. F. Scott, *Journal of Physics C: Solid State Physics* **10**, L329 (1977), URL <http://stacks.iop.org/0022-3719/10/i=11/a=011>.
- [110] T. Kimura, *Annual Review of Materials Research* **37**, 387 (2007), URL <http://dx.doi.org/10.1146/annurev.matsci.37.052506.084259>.
- [111] J. Wang, J. B. Neaton, H. Zheng, V. Nagarajan, S. B. Ogale, B. Liu, D. Viehland, V. Vaithyanathan, D. G. Schlom, U. V. Waghmare, et al., *Science* **299**, 1719 (2003), URL <http://science.sciencemag.org/content/299/5613/1719>.
- [112] N. A. Hill, *The Journal of Physical Chemistry B* **104**, 6694 (2000), URL <http://dx.doi.org/10.1021/jp000114x>.
- [113] M. Mostovoy, *Physical Review Letters* **96**, 067601 (2006), URL <http://link.aps.org/doi/10.1103/PhysRevLett.96.067601>.

- [114] J. J. Betouras, G. Giovannetti, and J. van den Brink, *Physical Review Letters* **98**, 257602 (2007), URL <http://link.aps.org/doi/10.1103/PhysRevLett.98.257602>.
- [115] S.-W. Cheong and M. Mostovoy, *Nature Materials* **6**, 13 (2007), URL <http://www.nature.com/nmat/journal/v6/n1/full/nmat1804.html>.
- [116] D. Khomskii, *Physics 2* **20** (2009), URL <http://physics.aps.org/articles/v2/20>.
- [117] J.-G. Park, M. D. Le, J. Jeong, and S. Lee, *Journal of Physics: Condensed Matter* **26**, 433202 (2014), URL <http://stacks.iop.org/0953-8984/26/i=43/a=433202>.
- [118] N. Jedrecy, H. J. von Bardeleben, V. Badjeck, D. Demaille, D. Stanescu, H. Magnan, and A. Barbier, *Physical Review B* **88**, 121409 (2013), URL <http://link.aps.org/doi/10.1103/PhysRevB.88.121409>.
- [119] R. Ramesh and N. A. Spaldin, *Nature Materials* **6**, 21 (2007), URL <http://www.nature.com/nmat/journal/v6/n1/full/nmat1805.html>.
- [120] N. A. Spaldin and M. Fiebig, *Science* **309**, 391 (2005), URL <http://science.sciencemag.org/content/309/5733/391>.
- [121] J. M. Rondinelli, M. Stengel, and N. A. Spaldin, *Nature Nanotechnology* **3**, 46 (2008), URL <http://www.nature.com/nnano/journal/v3/n1/full/nnano.2007.412.html>.
- [122] E. A. Eliseev, A. N. Morozovska, M. D. Glinchuk, B. Y. Zaulychny, V. V. Skorkhod, and R. Blinc, *Physical Review B* **82**, 085408 (2010), URL <http://link.aps.org/doi/10.1103/PhysRevB.82.085408>.
- [123] J. P. Velev, S. S. Jaswal, and E. Y. Tsymbal, *Philosophical Transactions of the Royal Society of London A: Mathematical, Physical and Engineering Sciences* **369**, 3069 (2011), URL <http://rsta.royalsocietypublishing.org/content/369/1948/3069>.
- [124] G. Lawes and G. Srinivasan, *Journal of Physics D: Applied Physics* **44**, 243001 (2011), URL <http://stacks.iop.org/0022-3727/44/i=24/a=243001>.
- [125] S. Borlenghi, W. Wang, H. Fangohr, L. Bergqvist, and A. Delin, *Physical Review Letters* **112**, 047203 (2014), URL <http://link.aps.org/doi/10.1103/PhysRevLett.112.047203>.
- [126] E. Barati, M. Cinal, D. M. Edwards, and A. Umerski, *Physical Review B* **90**, 014420 (2014), URL <http://link.aps.org/doi/10.1103/PhysRevB.90.014420>.
- [127] I. M. McKinley, F. Y. Lee, and L. Pilon, *Applied Energy* **126**, 78 (2014), URL <http://www.sciencedirect.com/science/article/pii/S0306261914003092>.

- [128] C. A. F. Vaz, *Journal of Physics: Condensed Matter* **24**, 333201 (2012), URL <http://stacks.iop.org/0953-8984/24/i=33/a=333201>.
- [129] P.-E. Janolin, N. A. Pertsev, D. Sichuga, and L. Bellaiche, *Physical Review B* **85**, 140401 (2012), URL <http://link.aps.org/doi/10.1103/PhysRevB.85.140401>.
- [130] C.-G. Duan, J. P. Velev, R. F. Sabirianov, Z. Zhu, J. Chu, S. S. Jaswal, and E. Y. Tsymbal, *Physical Review Letters* **101**, 137201 (2008), URL <http://link.aps.org/doi/10.1103/PhysRevLett.101.137201>.
- [131] T. Zhao, A. Scholl, F. Zavaliche, K. Lee, M. Barry, A. Doran, M. P. Cruz, Y. H. Chu, C. Ederer, N. A. Spaldin, et al., *Nature Materials* **5**, 823 (2006), URL <http://www.nature.com/nmat/journal/v5/n10/abs/nmat1731.html>.
- [132] S. Sahoo, S. Polisetty, C.-G. Duan, S. S. Jaswal, E. Y. Tsymbal, and C. Binek, *Physical Review B* **76**, 092108 (2007), URL <http://link.aps.org/doi/10.1103/PhysRevB.76.092108>.
- [133] P. Hänggi and F. Marchesoni, *Reviews of Modern Physics* **81**, 387 (2009), URL <http://link.aps.org/doi/10.1103/RevModPhys.81.387>.
- [134] J.-H. Moon, S.-M. Seo, K.-J. Lee, K.-W. Kim, J. Ryu, H.-W. Lee, R. D. McMichael, and M. D. Stiles, *Physical Review B* **88**, 184404 (2013), URL <http://link.aps.org/doi/10.1103/PhysRevB.88.184404>.
- [135] K. Di, V. L. Zhang, H. S. Lim, S. C. Ng, M. H. Kuok, J. Yu, J. Yoon, X. Qiu, and H. Yang, *Physical Review Letters* **114**, 047201 (2015), URL <http://link.aps.org/doi/10.1103/PhysRevLett.114.047201>.
- [136] F. Garcia-Sanchez, P. Borys, A. Vansteenkiste, J.-V. Kim, and R. L. Stamps, *Physical Review B* **89**, 224408 (2014), URL <http://link.aps.org/doi/10.1103/PhysRevB.89.224408>.

Eidesstattliche Erklärung

Hiermit erkläre ich, dass ich meine Dissertation selbständig und ohne fremde Hilfe verfasst und keine anderen als die von mir angegebenen Quellen und Hilfsmittel zur Erstellung meiner Dissertation verwendet habe. Den benutzten Werken wörtlich oder inhaltlich entnommene Stellen sind als solche gekennzeichnet.

Seyyed Ruhollah Etesami, _____

Halle an der Saale, den _____

Acknowledgements

This work would not have been performed in its present form without the help of others. Below I list those who contributed to the thesis directly or indirectly.

I express my thanks to **Prof. Dr. J. Berakdar**, **Prof. Dr. S. Trimper**, and **Prof. Dr. E. K. U. Gross** for giving me the opportunity to carry out this work as a PhD student of the International Max Planck Research School for Science and Technology of Nanostructures (IMPRS) and Martin-Luther-Universität Halle-Wittenberg. I specifically thank **Prof. Dr. J. Berakdar**, **Prof. Dr. S. Trimper**, **Dr. L. Chotorlishvili** and **Dr. A. Sukhov** for guiding me through my PhD. I thank **Dr. A. Ernst** as the coordinator and **I. Goffin** as the secretary of IMPRS and my colleagues **Dr. S. G. Bahoosh**, **Dr. T. Bose**, **Dr. Y. Pavlyukh**, **M. Schüler**, **S. Stagraczynski**, **M. Azimi**, **Y. Wätzel** and **M. Berthold** for providing a nice and comfortable atmosphere and assist me within my carrier. I also thank all other contributors to my publications, staff of Max-Planck institute and Martin-Luther university, and friends.

Curriculum Vitae

Personal Details

Name : Seyyed Ruhollah

Last Name : Etesami

Data of birth : 6 August 1983

Place of birth : Khomini Shahr, Isfahan, Iran

Nationality : Iranian

Education/Research

2002 - 2006 : B.Sc.

— Major : Solid State Physics

— University : University of Guilan, Iran

— Project : ITO Thin Film

— Supervisor: Prof. Seyed Mohammad Rozati

2006 - 2009 : M.Sc.

— Major : Condensed Matter Physics

— Institute : Institute for Advanced Studies in Basic Sciences (IASBS), Iran

— Thesis : Quantum Phase Transitions of Spin 1 System

— Supervisor : Prof. Mohamad Reza Khajehpour

2010 - 2011 : Military Service

2012 (Sep - Nov) : Guest

— Institute: Max Planck Institute of Microstructure Physics, Germany

Since Mar 2013 : PhD

— Major : Physics

— Institute : Max Planck Institute of Microstructure Physics, Germany

— University: Martin Luther University of Halle-Wittenberg, Germany

— Thesis : Kinetics of Ferroics at Nanoscales (Towards Low-energy Consuming Devices)

— Supervisor : Prof. Dr. Jamal Berakdar

Seyyed Ruhollah Etesami, _____

Halle an der Saale, den _____

List of Publications

1. S. R. Etesami, L. Chotorlishvili, A. Sukhov, and J. Berakdar : *Longitudinal spin current induced by a temperature gradient in a ferromagnetic insulator*, Phys. Rev. B **90** , pp 014410 (2014).
2. L. Chotorlishvili, Z. Toklikishvili, S. R. Etesami, V. K. Dugaev, J. Barnas, and J. Berakdar : *Magnon-driven longitudinal spin Seebeck effect in $F|N$ and $N|F|N$ structures: Role of asymmetric in-plane magnetic anisotropy*, J. Magn. Magn. Mater . **396** , pp 254 (2015).
3. S. R. Etesami, L. Chotorlishvili, and J. Berakdar : *Spectral characteristics of time resolved magnonic spin Seebeck effect*, Appl. Phys. Lett . **107** , pp 132402 (2015).
4. L. Chotorlishvili, S. R. Etesami, J. Berakdar, R. Khomeriki, and J. Ren : *Electromagnetically controlled multiferroic thermal diode*, Phys. Rev. B **92** , pp 134424 (2015).
5. S. R. Etesami and J. Berakdar : *Efficient thermal energy harvesting using nanoscale magnetoelectric heterostructures*, Appl. Phys. Lett. **108** , pp 053903 (2016).
6. S. R. Etesami, A. Sukhov, and J. Berakdar : *Kinetics of nanosize ferroelectrics*, Phys. Rev. B **94** , pp 174105 (2016).